DIRECT MEASUREMENT OF EDDY VISCOSITY AND ANALYSIS OF NON-BOUSSINESQ EFFECTS IN WALL-BOUNDED TURBULENT FLOWS

By
Danah Park and Ali Mani

Prepared with support from
The Boeing Company (SPO 134136),
the Office of Naval Research (#N000142012718),
the Stanford Graduate Fellowship Program, and
the Kwanjeong Educational Foundation Fellowship

Report No. TF-193

Flow Physics and Computational Engineering Group
Department of Mechanical Engineering
Stanford University
Stanford, CA 94305

December 2023

Direct Measurement of Eddy Viscosity and Analysis of Non-Boussinesq Effects InWall-Bounded Turbulent Flows

By

Danah Park and Ali Mani

Prepared with support from
The Boeing Company (SPO 134136),
the Office of Naval Research (#N000142012718),
the Stanford Graduate Fellowship Program, and
the Kwanjeong Educational Foundation Fellowship

Report No. TF-193

Flow Physics and Computational Engineering Group
Department of Mechanical Engineering
Stanford University
Stanford, CA 94305

December 2023

Abstract

This work presents studies of momentum mixing by turbulence in a channel flow, a separated boundary layer flow, and a separated boundary layer with sweep using direct numerical simulation (DNS) and the macroscopic forcing method (MFM, Mani and Park, Physical Review Fluids, 2021, p.054607) to quantify the non-Boussinesq effects of momentum mixing from turbulent eddies. The key goal of our investigation is to develop a quantitative understanding of the anisotropy and nonlocality of the eddy viscosity operator in wall-bounded turbulent flows.

The first study aims to quantify how turbulence in a channel flow mixes momentum in a purely parallel flow. We applied MFM to DNS of a turbulent channel flow at Re_τ=180 using two different forcing strategies designed to separately assess the anisotropy and nonlocality of momentum mixing. In the first strategy, the leading term of the Kramers-Moyal expansion of the eddy viscosity operator is quantified, revealing all 81 tensorial coefficients that essentially characterize the local-limit eddy viscosity. The results indicate: (1) the eddy viscosity has significant anisotropy, (2) Reynolds stresses are generated by both the mean strain rate and mean rotation rate tensors associated with the momentum field, and (3) the local-limit eddy viscosity generates asymmetric Reynolds stress tensors. In the second strategy, the eddy viscosity is quantified as an integration kernel revealing the nonlocal influence of the mean momentum gradient at each wall-normal coordinate on all nine components of the Reynolds stresses over the channel width. Our results indicate that while the shear component of the Reynolds stress is reasonably approximated by the local mean gradients, other components of the Reynolds stress are highly nonlocal.

In the second study, we present a direct measurement of the eddy viscosity for a canonical separated boundary layer flow at Re_θ=350. This work presents the leading-order term in the Kramers-Moyal expansion of the eddy viscosity operator representing its local approximation while focusing on the anisotropy. All relevant tensor components of this operator are computed, and the results show significant anisotropic effects. In our a priori testing, we show that the measured eddy viscosity, when multiplied by the mean velocity gradients obtained from DNS, results in a reasonable prediction of the Reynolds stress profiles, indicating the dominant role of the leading-order term in the Kramers-Moyal expansion of the nonlocal eddy viscosity. Furthermore, the resulting mean flow from a RANS solution that employs the measured leading order eddy viscosity is shown to be

remarkably closer to the mean of the DNS solutions compared to traditional RANS solutions that employ a Boussinesq eddy viscosity or its anisotropic extensions based on quadratic constitutive relations. The remaining error between this improved RANS solution and the DNS mean field is quantified as a measure of the upper bound of accuracy for local Reynolds stress closures. As part of our investigation, we also identify the dominant components of the eddy viscosity tensor that play a significant role in momentum mixing. Lastly, using a comparison of predictions of the local eddy viscosity against the mean of DNS and analyzing the positive definiteness of the leading-order eddy viscosity tensor, we identify zones where nonlocal momentum mixing plays an important role.

In the third study, we extend the previous work to a more realistic separation bubble with spanwise sweep, which has non-zero shear at the separation line. Similar to the previous works, using MFM applied to DNS, we measure the leading-order eddy viscosity tensor. The results show substantial anisotropic effects in both separation bubbles, but additional anisotropic effects are present in the separation bubble with sweep. This outcome contradicts the independence principle, suggesting a significant impact of the spanwise velocity gradient on the mean chordwise momentum mixing, even in close proximity to the separation line. Furthermore, similar to the unswept case, we utilize MFM and momentum balance analysis to determine important components of the eddy viscosity and identify additional components resulting from the sweep-induced effects. Finally, we identify regions where the measured leading-order eddy viscosity exhibits local non-positive semidefinite characteristics and make a comparison with the unswept case. In these regions, momentum mixing must encompass substantial nonlocal influences, raising concerns about the reliability of local models.

Overall, these studies provide important perspectives on the macroscopic behavior of turbulence in diverse flow setups, and they supply valuable data for enhancing turbulence closure models. These discoveries unveil unique ways to understand how turbulence influences the mixing of momentum in wall-bounded flows. Furthermore, they encourage a reevaluation of previous works in turbulence modeling and provide a foundation for enhancing the effectiveness of current RANS models.

Acknowledgment

The authors acknowledge the support provided by the Boeing Company under Grant No. SPO 134136, and by the Office of Naval Research under Grant number N000142012718. They also acknowledge the Stanford Graduate Fellowship program and the Kwanjeong Educational Foundation fellowship.

THIS PAGE DELIBERATELY LEFT BLANK

Contents

List of Tables

List of Figures

Chapter 1

Introduction

1.1 Wall-bounded Turbulent Flow

Wall-bounded turbulent flow refers to a type of turbulent fluid motion that occurs in the vicinity of a solid surface or wall. The flow is bounded by the wall due to the no-slip and no-penetration conditions between flow and the wall and therefore, the presence of the wall introduces frictional effects on the fluid, which can significantly affect the flow behavior. In wall-bounded turbulent flows, small-scale, highly irregular vortices and eddies form near the wall, which rapidly dissipate energy and transport momentum towards the wall faster than an otherwise laminar flow. These vortices are sustained by the complex interactions between the near-wall shear strain and the turbulent fluctuations in the fluid, and they play a crucial role in determining the overall flow behavior and thereby the friction force and normal loads on the solid surface [25]. Understanding their behavior is important for predicting and optimizing the performance of systems involving wall-bounded turbulent flows.

Wall-bounded turbulent flows are often characterized by Reynolds number based on the frictional shear stress τ. One of the main reasons τ is used is that it can be measured through experiments, and it serves as a crucial parameter in various applications. The Reynolds number is the ratio of inertia to viscous forces:

$$\mathrm{Re} = \frac{UL}{\nu} \tag{1.1}$$

where U and L are characteristic velocity and length scales and ν is the kinematic viscosity of the fluid. Utilizing the frictional shear stress, we often use $\mathrm{Re}_\tau = u_\tau L/\nu$ where u_τ is the friction velocity defined as:

$$u_\tau = \left(\frac{\tau}{\rho}\right)^{1/2} \tag{1.2}$$

where ρ is the density of the fluid. The characteristic length scale L is often a length scale corresponding to the wall-normal direction. For instance, it is a wall height for a channel flow and a

boundary layer thickness for a attached boundary layer.

Wall-bounded turbulent flows are commonly encountered in various practical applications, and the scales of these flows can differ significantly between applications. In such context of engineering analysis, an essential consideration is the range of scales encompassed within a flow, specifically, the ratio between large-scale eddies and small-scale eddies. This ratio is characterized by the Reynolds number, where higher values of Reynolds number indicate a greater range of scales. For instance, at a Reynolds number on the order of 10^2, turbulent flow of blood in a heart is a wall-bounded flow example, while the flow around a wind farm encounter Reynolds number on the order of 10^3. The industrial applications of wall-bounded flows can range from Reynolds numbers of 10^3 to 10^5, such as flows past ships and planes. Furthermore, most atmospheric flows are at a very high Reynolds numbers [58]. Common observation among these applications of wall-bounded flow is that they all exhibit a wide range of scales.

Understanding wall-bounded turbulent flows is important for industry applications as a considerable amount of energy, approximately 25%, used by industries and businesses is dedicated to transporting fluids through pipes and canals or vehicles through air or water. A significant portion of this energy is lost due to turbulence in the vicinity of walls, accounting for about one quarter of the total energy dissipation. Additionally, shear-dominated wall-bounded turbulence contributes to approximately 5% of the CO2 emissions caused by human activities [25]. Therefore, understanding and predicting wall-bounded turbulence is very important in both industry and environmental aspects.

1.2 Prediction of Flow Separation

Settings in which wall-bounded turbulence encounters flow separations over smooth, often curved, surfaces, are among the most challenging environments when it comes to quantitative prediction of turbulent flows. Smooth body flow separation is a complex physical phenomenon that occurs when the boundary layer of a smooth solid body detaches due to an adverse pressure gradient. The separation of the flow from the solid body can occur at various locations on the three-dimensional surface of an aircraft, including the leading edge of the wing and nacelle, particularly during high angle of attack maneuvers. In fact, smooth body flow separation is a critical consideration in aircraft design and engineering, as it can significantly impact the aerodynamic performance of the aircraft.

The accurate prediction of smooth body flow separation is of utmost importance in computational fluid dynamics (CFD) because it plays a crucial role in determining system-level metrics such as aerodynamic loads, stall limit, and maximum lift. One way to predict the flow separation is to perform direct numerical simulation (DNS). DNS is a computational technique to predict fluid flows at a high level of detail by numerically solving the Navier-Stokes equations without any modeling assumptions. Unlike traditional turbulence models, which use closure models to approximate the

effects of small-scale turbulent motions, DNS resolves all scales of motion and directly computes the velocity, pressure, and other flow variables for every point in space and time. This makes DNS a highly accurate method for predicting fluid flow behavior.

Unfortunately, DNS is computationally expensive and is typically limited to simulations of relatively simple geometries and lower Reynolds number flows. At high Reynolds numbers, the range of length scales and temporal scales involved in turbulent motions becomes very wide, spanning orders of magnitude, which makes DNS infeasible as the number of computational cells required to resolve the small-scale eddies becomes prohibitively large. As a result, the computational expense associated with DNS grows rapidly with increasing Reynolds number, making it difficult to simulate high Reynolds number flows using this method. For instance, to capture the spatial changes in a turbulent flow, a considerable number of grid points on the order of $\mathrm{Re}_\tau^{9/4}$ is necessary. Additionally, accounting for time-varying fields and other computational expenses the total estimated computational cost increases roughly in proportion to Re_τ^4 [58, 74, 44]. Since many real-world flows have Re_τ values greater than one thousand, the expenses related to DNS can quickly become too high to be feasible. So far, DNS of wall-bounded turbulence has only been possible for simple configurations and relatively low Reynolds numbers. The highest is around $\mathrm{Re}_\tau = 5000$ to the author's knowledge [30]. Therefore, utilizing such high-fidelity simulations for the practical applications can be computationally expensive and often impossible. This limitation has led to the development of other approaches, such as Large Eddy Simulation (LES) and Reynolds-averaged Navier-Stokes (RANS), which are more suited to simulating turbulent flows at higher Reynolds numbers.

1.3 RANS and Boussinesq Approximation

Reduced-order models have gained popularity in engineering, especially in the field of fluid mechanics, where the accurate prediction of aerodynamic flows is essential for the design of vehicles such as aircraft and naval vessels. For example, engineers often focus on predicting large-scale motions and system-level impacts, such as lift, drag, and force moments on an aircraft, to ensure the safety and efficiency of the vehicle. Such macroscopic prediction does not require high-fidelity data and therefore, reduced-order models have been persistently attractive as a cost-effective way of predicting industry-relevant high Reynolds number flows.

One of the most commonly used reduced-order methods for turbulent flow prediction in industrial settings is the RANS method. RANS provides a time-efficient and cost-effective way to predict turbulent flows and system-level statistics, such as lift, drag, and force moments, on an aircraft or naval vessel. It has been used extensively for predicting turbulent flow patterns on various aircraft components, including wings, nacelles, and fuselages, and naval vessel components, including hulls and propellers. Due to its low cost, fast time to solution, computational robustness, RANS has been an attractive option for engineers. However, current RANS models are limited in their accuracy

due to relying on heuristic derivation and empirical model fittings. Despite these limitations, RANS remains an essential tool for engineers due to its practicality and effectiveness in predicting turbulent flows.

Solving for the ensemble-averaged momentum fields, RANS requires closure models that allow quantitative expressions of the Reynolds stresses in terms of mean-field quantities such as the mean velocity gradient tensor [5]. Many of the turbulence models in use today are based on the Boussinesq approximation [8], in which the Reynolds stresses are assumed to be related to the local mean flow strain rate via an eddy viscosity coefficient. In addition to the locality assumption, this approximation relegates the entire anisotropic relation between mean velocity gradients and Reynolds stresses to an isotropic eddy viscosity. The two simplifications offered by the Boussinesq approximation reduce the job of turbulence modeling to a determination of a scalar eddy viscosity field from which local Reynolds stresses can be determined algebraically without the need to solve any additional equations. For cases in which a single component of the Reynolds stress plays the dominant role, such as in parallel flows, a scalar eddy viscosity can be tuned to yield acceptable Reynolds stress fields [47]. However, most turbulence models utilize this approximation even for multi-dimensional flows [61, 10, 36, 16, 22, 72]. While some models allow anisotropic eddy viscosities [60, 35, 52], they still retain the locality of the Reynolds stress dependence on the mean velocity gradient.

Experimental measurements, as well as DNS data, suggest that the isotropy and locality assumptions of the Boussinesq approximation are not strictly valid. Several studies have shown significant misalignment between the principal axes of the Reynolds stress and strain rate tensors, indicating non-negligible anisotropy of the eddy viscosity operator [48, 50, 38, 12]. Furthermore, the assumption of Reynolds stress locality is often not true because turbulent mixing may exist from the history of the straining in a given region of a turbulent flow. For instance, the experiment conducted by Warhaft showed that the Reynolds stress can arise from the history effects of straining, even with a locally zero mean strain rate. In this case, the Reynolds stress should incorporate temporal or spatial nonlocality of the strain rate tensor [68].

1.4 Macroscopic Forcing Method

Given these pieces of evidence, various modeling techniques have attempted to relax both locality and isotropy assumptions via development of second-order closure models [71, 65, 9, 29, 18] often using the Reynolds stress transport equation as a framework to identify the needed closures. Each of these models, provides a specific way in which Reynolds stresses could depend nonlocally and/or anisotropically on the velocity gradient field. However, standard data of turbulent flows, either from DNS or experiments, does not provide sufficient information to allow proper discrimination between these models. While these data reveal anisotropy of the Reynolds stresses, they do not uniquely determine the anisotropy or nonlocality of the closure operators that express their dependence on

the mean velocity gradient. Closing this gap would require quantification of the eddy viscosity as an operator acting on the mean velocity gradient. With this goal in mind, this study presents a direct quantification of the eddy viscosity operator in a canonical turbulent flow via utilization of the macroscopic forcing method (MFM) [34].

1.4.1 Characterization of Eddy Viscosity as an Operator

Prior to the description of our work, we start by reviewing generalized forms of the eddy diffusivity and eddy viscosity operators for scalar and momentum transport in turbulent flows. Firstly, one way of generalizing the Boussinesq approximation is to allow for the anisotropy of the eddy viscosity. Batchelor suggested using a second-order tensor replacing the diffusion coefficient in the Fickian model to describe the mean transport of a scalar quantity [6]. Later, a similar concept was suggested by [49], where the mean turbulent flux of a passive scalar was approximated with an algebraic model expressed in a second-order tensor eddy diffusivity. This anisotropic eddy diffusivity model can be written as:

$$-\overline{u_i' c'} = D^0_{ij} \frac{\partial C}{\partial x_j} \tag{1.3}$$

where $\overline{(\cdot)}$ represents ensemble-average, u_i' represents the fluctuation of the velocity, C and c' represent the mean and the fluctuation of the scalar quantity being transported, x_i represents the coordinate system, and D^0_{ij} represents the second-order eddy diffusivity tensor that is local.

Similarly, for the turbulent momentum flux, one method of generalizing the Boussinesq approximation is to use a tensorial representation of the eddy viscosity. Hinze has suggested the use of the fourth-order tensor as the eddy viscosity [23]. Later, Stanivsic et al. conducted a systematic investigation of the tensorial character of the eddy viscosity coefficient and revealed that the eddy viscosity tensor has to be at a minimum fourth-order [66]. In parallel to the anisotropic eddy diffusivity model, the anisotropic eddy viscosity model for momentum transport can be written as:

$$-\overline{u_i' u_j'} = D^0_{ijkl} \frac{\partial U_l}{\partial x_k} \tag{1.4}$$

where U_l represents mean velocity field. Here, the Reynolds stresses $\overline{u_i' u_j'}$ is locally closed in terms of the fourth-order tensorial eddy viscosity D^0_{ijkl} and the mean velocity gradient.

An even more general form of the eddy viscosity can be used to incorporate not only anisotropy but also nonlocality. Hamba suggested writing the closure of the Reynolds stress in terms of the mean velocity gradient at remote times and locations. This form of eddy viscosity involves a fourth-order tensorial kernel, which we refer to as the eddy viscosity kernel [20, 21]. For statistically stationary flows, this relation can be expressed as

$$-\overline{u_i' u_j'}(\mathbf{x}) = \int D_{ijkl}(\mathbf{x}, \mathbf{y}) \left. \frac{\partial U_l}{\partial x_k} \right|_{\mathbf{y}} \mathrm{d}^3\mathbf{y} \,, \tag{1.5}$$

where $D_{ijkl}(\mathbf{x}, \mathbf{y})$ is the eddy viscosity kernel indicating how mean gradients at location $\mathbf{y}$ result in Reynolds stresses at location $\mathbf{x}$. [20] reported the first quantification of the eddy viscosity kernel for a turbulent channel flow using a Green's function formulation approach based on an earlier work by [27]. However, their study focuses on a subset of the tensorial coefficients, i.e., D_{ij21}. This choice is motivated since other components of the mean velocity gradient are zero in channel flow; however, the Reynolds stresses are still sensitive to all mean flow gradients since their corresponding eddy viscosities are nonzero. Nevertheless, quantification of other components of eddy viscosity in this canonical setting would provide significant insights about momentum mixing in the broader context of wall-bounded shear flows. Aside from this shortcoming, [20] chose to manually enforce the symmetry $D_{ijkl} = D_{jikl}$ by performing arithmetic averaging of the respective components (i.e., ij and ji) of the output data from their simulations. This choice was made given the expectation that the Reynolds stress tensor as the output of Equation 1.5 must always be symmetric, while the raw kernels did not follow this symmetry.

1.4.2 Generalized Momentum Transport Equation

Recently, Mani and Park presented an alternative interpretation of Equation 1.5 in the context of the generalized momentum transport (GMT) equation [34]. GMT can be derived by applying the Reynolds Transport Theorem to momentum transport without constraining the momentum field to be identical to the velocity field. In this context, the Reynolds stress, expressed as $\overline{u_i' v_j'}$, is interpreted as the mean product of two conceptually different fields, with u_i representing the kinematic displacement of volume acting as a transporter of momentum, and v_j representing momentum per unit mass, the quantity of interest that results in friction and pressure. Navier-Stokes (NS) is rendered as a special solution to GMT in which the two fields are constrained to be equal. Specifically, when GMT is supplied with the same boundary conditions and forcing conditions as those in NS, the solution to NS is the only attractor solution to GMT, as shown theoretically and numerically by Mani and Park [34]. With this interpretation, Equation 1.5 is, in fact, a closure operator to the ensemble-averaged GMT, which is an extension of the Reynolds Averaged Navier-Stokes (RANS) equation. In other words, ensemble-averaged GMT is not limited to RANS, but it is inclusive of RANS. Therefore, D_{ijkl} and D_{jikl} are not required to be equal since $\overline{u_i' v_j'} \neq \overline{u_j' v_i'}$ in the GMT context. The present study reassesses the momentum transport closure by examining the raw eddy viscosity operator without any symmetry averaging. We confirm that while the eddy viscosity kernel of channel flow is not symmetric, it still results in symmetric Reynolds stresses when it acts on the mean velocity gradient of the same flow generating the eddy viscosity.

As previously mentioned, Mani and Park provide a statistical technique called the macroscopic forcing method (MFM), which allows direct measurement of a flow's eddy viscosity D_{ijkl} with data gathered from direct numerical simulations (DNS) of the Navier-Stokes system and the GMT [34]. More generally speaking, MFM allows precise computation of RANS closure operators via

applying various macroscopic forcing to the GMT equations, which can be utilized to extract the eddy viscosity operator. It is worth noting that macroscopic forcing is not limited to Dirac delta functions, which is shown to reveal the same Green's functions obtainable from the method from Hamba [20]. For instance, Shirian and Mani employed harmonic forcing to efficiently unveil the eddy diffusivity operator for homogeneous isotropic turbulence [56]. They successfully fitted this operator with an analytical expression. More importantly, Mani and Park developed the inverse macroscopic forcing method (IMFM), in which forcing to constrain mean polynomial fields was shown to reveal nonlocal moments of the underlying eddy diffusivity operator in an economical way compared to the Green's function approach [34]. This study utilizes this method in our investigation of turbulent channel flow. More specifically, we examine a systematic procedure for obtaining a local operator approximation of the full eddy viscosity operator by considering a Kramers-Moyal expansion of the eddy viscosity operator and quantifying its leading term [67]. This approach not only enables the estimation of the eddy viscosity in an economical fashion but also separates out the easy-to-comprehend local eddy viscosity by utilizing this established expansion, which we believe was a missing piece in the analysis of Hamba [20].

1.5 Utilizing MFM for Wall-bounded Turbulent Flows

In this study, we delve into the dynamics of wall-bounded turbulent flows using DNS and MFM techniques. Our goal is to obtain a better understanding of the anisotropy and nonlocality of momentum mixing caused by turbulent eddies. To achieve this, we propose utilizing MFM to measure the fully generalized kernel representation of the eddy viscosity and leading-order anisotropic representation of the eddy viscosity in wall-bounded flows.

The key remaining question is which flow systems are suitable for the application of MFM. As mentioned earlier, current RANS models are often unreliable for complex flow systems such as smooth body flow separation. It has been demonstrated that in the high-lift scenario, where separation is dominant, the RANS solutions become very unreliable. Lift-coefficient results in the AIAA CFD High-Lift Prediction Workshop reveal that the lift-coefficient prediction encounters substantial errors at high angles of attack [57, 53]. RANS solutions vary by different turbulence models and code implementations. Therefore, even with state-of-the-art simulations, achieving reliable RANS solutions is challenging. Our goal is to understand the missing pieces in the RANS models in such external wall-bounded flow scenarios.

We examine three different flow systems, each carefully selected to help us gain insights into the flow phenomena in wall-bounded turbulent flows, specifically around an airplane wing in a high-lift scenario. The selection of the flow systems was based on an analysis of surface streamlines and skin friction contours on an airplane wing for both landing and takeoff configurations [28]. The first flow system we explore is the channel flow, which exhibits physics that are very similar to those

of the attached boundary layers on a smooth surface. Next, we investigate a canonical separated boundary layer inspired by the model adopted by previous researchers [62, 40, 14]. This flow system mimics two-dimensional separation at the outboard wing near the trailing edge. Lastly, we focus on a canonical separated boundary layer with sweep in our third flow system. This system is designed to help us understand three-dimensional separation at the inboard wing. By studying the anisotropy and nonlocality of momentum mixing in this system, we aim to gain insights into the dynamics of turbulent mixing in such flow regimes as well.

Through these investigations, we quantify the eddy viscosity data for turbulence closure models and examine non-Boussinesq effects in different flow systems. Our studies offer insights into the dynamics of mean momentum mixing in various flow configurations relevant to both aerodynamic and naval applications, revealing missing pieces in existing RANS models.

1.6 Outline

The first study presented in Chapter 3 analyzes turbulence in a channel flow at Re_τ=180 using two MFM forcing strategies to precisely decompose the Reynolds stress closure into local and nonlocal operators. We begin by evaluating the isotropy assumption in Boussinesq's approximation. For simplicity, we defer the non-locality analysis by solely focusing on the assessment of the leading-order (local-limit) eddy viscosity tensor. This study presents the fields associated with all 81 tensorial coefficients of this leading-order eddy viscosity. With the measured local eddy viscosity tensor, we discuss the following: the standard eddy viscosity, the quantified anisotropy, the dependency of Reynolds stress on the rate of rotation, the leading-order Reynolds stress, and the positive definiteness of the leading-order eddy viscosity operator. In addition, we extend our study to nonlocal effects and provide the full eddy viscosity kernel, quantifying the dependence of all components of the Reynolds stress as a nonlocal function of the wall-normal velocity gradient.

In the second study presented in Chapter 4, we compute the leading-order eddy viscosity, expressed as a fourth-order tensor acting on the local mean velocity gradient for a separation bubble. Considering the canonical problem of an induced separation bubble on a fully turbulent boundary layer over a flat plate [62, 40] at Re_θ=350, we compute all the relevant components of the leading-order eddy viscosity tensor as a function of spatial coordinates. This leading-order eddy viscosity captures the local limit of the generalized (nonlocal) eddy viscosity operator. First, we examine the various components of the measured eddy viscosity and demonstrate the need for anisotropy in local Reynolds stress closure models. We also identify important anisotropic components for the prediction of the flow. Then, by assessing the accuracy of a RANS model that uses this measured leading-order eddy viscosity as its closure operator, we estimate the importance of non-local effects, and thereby provide an upper bound on the accuracy of local RANS models for this flow.

In the last study presented in Chapter 5, we extend our previous MFM work to a more realistic

case of separation. The previous MFM work involves a unique case where the shear stress is zero at the separation bubble. However, realistic flows involve three-dimensional effects of the mean flow where most of the separation line experiences non-zero mean shear. To remedy this gap and following [14], we consider a canonical flat plate turbulent boundary layer setting at Re_θ=350 in which a spanwise sweep is imposed on top of the boundary, while similar to the prior work, separation is induced via suction and blowing boundary conditions. Following [14], the spanwise sweep is designed to result in a 35° angle between the chordwise direction and the streamwise flow outside of the boundary layer. The goal of this work is to understand the sensitivity of the eddy viscosity tensor to the imposed sweep and to re-assess the relative role of eddy viscosity anisotropy in determining the mean momentum budget in this flow. We use MFM to quantify all relevant components of the local-limit eddy viscosity tensor. Finally, we compare the anisotropic eddy viscosity tensors between the separation bubble with and without sweep [41]. While both exhibit substantial anisotropic effects, we identify additional anisotropy to those previously quantified in the case of a two-dimensional separated boundary layer.

Finally, in Chapter 6, we provide a summary of our findings concerning eddy viscosity operators of the channel flow and separated boundary layers. Furthermore, we outline the limitations inherent in our work and present potential avenues for extending these analyses.

Chapter 2

Numerical Methods

In this chapter, we introduce the governing equations and RANS equation as well as its closure. We then introduce the eddy viscosity kernel D_{ijkl} which is a generalized form of the eddy viscosity ν_T in the Boussinesq approximation and its local-limit. Finally, we discuss numerical methods for each flow systems: channel flow, separated boundary layer, and separated boundary layer with sweep.

2.1 Governing Equations and RANS closure

The dimensionless equations expressing mass and momentum conservation are as follows:

$$\frac{\partial u_i}{\partial t} + \frac{\partial u_j u_i}{\partial x_j} = -\frac{\partial p}{\partial x_i} + \frac{1}{\mathrm{Re}} \frac{\partial^2 u_i}{\partial x_j \partial x_j} + r_i, \tag{2.1}$$

$$\frac{\partial u_j}{\partial x_j} = 0, \tag{2.2}$$

where u_i is the flow velocity, p is the fluctuating pressure normalized by density, x_i is the Cartesian coordinate system, t is time, and r_i represents additional force terms.

The RANS equations can be obtained by taking the ensemble-average of Equations 2.1 and 2.2, yielding:

$$\frac{\partial U_i}{\partial t} + \frac{\partial U_j U_i}{\partial x_j} = -\frac{\partial \overline{p}}{\partial x_i} + \frac{1}{\mathrm{Re}} \frac{\partial^2 U_i}{\partial x_j \partial x_j} - \frac{\partial \overline{u_j' u_i'}}{\partial x_j} + \overline{r}_i, \tag{2.3}$$

$$\frac{\partial U_j}{\partial x_j} = 0, \tag{2.4}$$

where U_i is the mean velocity, u_i' is the velocity fluctuation around the mean velocity, and $\overline{(\cdot)}$ imply ensemble-averaged quantities. To close this system, the divergence of Reynolds stresses, $\partial \overline{u_j' u_i'} \big/ \partial x_j$, need to be modeled in terms of the primary variable U_i. This can be generally expressed as an

operator acting on the ensemble-averaged field, $-\partial\overline{u_j'u_i'}\Big/\partial x_j \equiv \overline{\mathcal{L}}\left(U_i\right)$. One form of such operators is expressed in Equation 2.6.

Many of the RANS models used today are based on the Boussinesq approximation. In his paper from 1877, Boussinesq hypothesized that the Reynolds stress $\overline{u_i'u_j'}$ is proportional to the mean strain rate tensor $S_{ij} = \frac{1}{2}\left(\frac{\partial U_i}{\partial x_j} + \frac{\partial U_j}{\partial x_i}\right)$ yielding linear eddy viscosity model [8]:

$$-\overline{u_i'u_j'} = 2\nu_T S_{ij} - \frac{2}{3}k\delta_{ij} = \nu_T\left(\frac{\partial U_i}{\partial x_j} + \frac{\partial U_j}{\partial x_i}\right) - \frac{2}{3}k\delta_{ij} \tag{2.5}$$

where the coefficient of proportionality ν_T is often referred to as the eddy viscosity, where we later refer to as standard eddy viscosity.

Equation 2.5 makes several assumptions, including the isotropy and the locality of the eddy viscosity; that is, the Reynolds stress only arises from the local mean velocity gradient in the same direction at a given location aligned. However, as mentioned earlier, this is not true in many flow systems, especially in a complex wall-bounded flow. Hence, we need to use a more general form of eddy viscosity to investigate the anisotropic and nonlocal effects of the Reynolds stress:

$$-\overline{u_i'u_j'}(\mathbf{x}) = \int D_{ijkl}(\mathbf{x},\mathbf{y})\left.\frac{\partial U_l}{\partial x_k}\right|_{\mathbf{y}} \mathrm{d}^3\mathbf{y}\,, \tag{2.6}$$

where $D_{ijkl}(\mathbf{x},\mathbf{y})$ is the fourth-order tensorial eddy viscosity kernel, and $\mathbf{x}$ and $\mathbf{y}$ are each the 3D coordinates respectively pointing to the location where the Reynolds stress is measured and the location where the mean velocity gradient is probed.

Equation 2.6 was suggested by [20] as the exact closure for the Reynolds stress. In few works on scalar transport, a more advanced form was suggested to take into accounts the time-historical effects as well, but we limit the scope of this analysis to the form of Equation 2.6 [19, 51]. This equation, by including a fourth-order tensorial kernel, allows misalignment between the Reynolds stress and the velocity gradient. Moreover, the equation states that the Reynolds stress at location $\mathbf{x}$ is the summation of the effects from the velocity gradients at different locations $\mathbf{y}$. To measure the anisotropy and the nonlocality of the eddy viscosity, it is important to quantify and analyze this eddy viscosity kernel.

Before we discuss the measurement of the eddy viscosity kernel, we first revisit the measurement of the standard eddy viscosity ν_T. There have been many attempts to quantify the standard eddy viscosity in Equation 2.5 in the wall-bounded flows using experiments and DNS results [24, 45, 4]. One simple way is to approximate the model form and calculate the eddy viscosity as the ratio between the Reynolds stress and the velocity gradient where both quantities are obtained from the DNS results: $\nu_T \simeq -\overline{u_i'u_j'}/S_{ij}$. However, computing the eddy viscosity such way has two limitations. The first is that the eddy viscosity has a singular value where the velocity gradient is zero and extrapolation is often needed to avoid this singularity. The second limitation is that the given

equation already assumes the effective-viscosity model, which uses the Boussinesq approximation, and therefore ν_T is not the leading-order approximation of the actual eddy viscosity which would require calculating the leading-order approximation of the full tensorial eddy viscosity kernel from Equation 2.6. Using the exact definition of the RANS closure as in Equation 2.6 allows us to avoid these two limitations.

Therefore, a DNS solution to a wall-bounded flow does not provide enough information to fully quantify the nonlocal eddy viscosity kernel, $D_{ijkl}(\mathbf{x}, \mathbf{y})$. A full characterization of D requires quantification of Reynolds stresses in response to all possible independent flow gradients scenarios. Following Mani and Park [34], we next describe the procedure of obtaining D. In this work, however, we limit the scope of our analysis to the one or two-dimensional RANS context, in which we ignore spatio-temporal directions that are statistically homogeneous. However, the employed macroscopic forcing methodology is in principle generalizable to multi-dimensional cases, and with higher computational expense can capture the full behavior of $D_{ijkl}(\mathbf{x}, \mathbf{y})$.

2.2 Macroscopic Forcing Method

The macroscopic forcing method (MFM) is a systematic technique that allows a specialized statistical interrogation of DNS turbulence data to extract the exact form of closure operators required in RANS models [34]. The advantage of MFM is that it allows the determination of a precise RANS operator by forcing the momentum field while remaining non-intrusive to the underlying momentum transporting a turbulent flow.

2.2.1 Generalized Momentum Transport Equation

In our earlier work, which was mainly on the transport of passive scalars, we briefly introduced how one can apply MFM to analyze momentum transport [34]. To quantitatively determine the eddy viscosity operator, one first needs the detailed velocity field of the specific flow of interest. One method of obtaining such velocity fields is to perform a DNS simulation, which we call the donor simulation, as it donates a velocity field whose eddy viscosity is to be determined.

To analyze momentum transport by a given flow, we will now consider GMT, which can be derived from the Reynolds Transport Theorem for a fluid system with a Fickian model for molecular viscosity.

$$\frac{\partial v_i}{\partial t} + \frac{\partial u_j v_i}{\partial x_j} = -\frac{\partial q}{\partial x_i} + \frac{1}{\mathrm{Re}} \frac{\partial^2 v_i}{\partial x_j \partial x_j} + r_i, \tag{2.7}$$

$$\frac{\partial v_j}{\partial x_j} = 0. \tag{2.8}$$

where v_i represents momentum per unit mass, and is considered to be different from u_i from the

donor velocity field. Also, q is the generalized pressure to ensure the incompressibility of the velocity field v_i.

Equations 2.7 and 2.8 then describe a passive solenoidal vector field that is transported by the background velocity field u_j governed by Equation 2.1. An advantage of working with GMT, as opposed to NS, is its linearity with respect to the transported quantity, v_i. Under such conditions, expressing the generalized eddy viscosity in the format given by Equation 2.6 becomes meaningful. As discussed by Mani and Park [34], GMT spans a larger solution space than NS; NS is a special subset of the GMT space where $v_i = u_i$.

An important question that naturally follows is whether the computed RANS operator of GMT is the same as that of the NS equation. In our earlier work, we already showed analytically and numerically that the macroscopic operators of the GMT and NS equations are identical [34]. Moreover, the solutions of GMT and NS equations become microscopically the same after sufficient time regardless of the initial conditions when we apply the same boundary conditions to both equations. For example, the time scale at which the solutions become identical was found to be $\tau_{\text{mix}} = 16.6\delta/u_\tau$ for a turbulent channel flow. Therefore, it is justified that the macroscopic operator of the GMT equation obtained by MFM is the same as the RANS operator of the NS equations. In sum, GMT works as an auxiliary set of equations that probes RANS operator of NS and therefore we can obtain eddy viscosity of the RANS equations by investigating that of the GMT equations.

It is important to note that Hamba [20] wrote an equation very similar to GMT equations in spite of taking a conceptually different derivation path. His passive vector equation is indeed GMT subtracted by the mean of GMT. The main difference lies in the explicit inclusion of forcing in the equations, allowing for a general macroscopic field. In contrast, Hamba [20] implicitly applies forcing by specifically considering Dirac delta function mean fields.

2.2.2 Analysis Strategy and Leading-order Approximation

We aim to study two aspects of the eddy viscosity kernel: the anisotropy and the nonlocality. To fully investigate such non-Boussinesq effects, it is ideal to compute every value of the full eddy viscosity kernel D_{ijkl} in Equation 2.6.

$$-\overline{u_i' v_j'}(\mathbf{x}) \quad = \int D_{ijkl}(\mathbf{x}, \mathbf{y}) \left.\frac{\partial V_l}{\partial x_k}\right|_{y_2} \mathrm{d}\mathbf{y}. \tag{2.9}$$

We can actually simplify Equation 2.9 utilizing integration of the homogeneous directions. For instance, since the channel flow is homogeneous in x_1 and x_3 directions and statistically stationary, we integrate the mixing effect in these directions. The simplified Reynolds stress for GMT variables can be expressed as:

$$-\overline{u_i' v_j'}(x_2) \quad = \int D_{ijkl}(x_2, y_2) \left.\frac{\partial V_l}{\partial x_k}\right|_{y_2} \mathrm{d}y_2. \tag{2.10}$$

Equation 2.9 incorporates anisotropy via tensorial representation and nonlocality via the integration form. MFM has the capability to compute all the elements in the eddy viscosity kernel $D_{ijkl}(x_2, y_2)$ by tracking the influence of each entry of dV_l/dx_k on the entire Reynolds stress field. It has been demonstrated by Liu [31] that such a brute force approach is theoretically equivalent to Hamba's Green's function approach [20].

However, one caveat is that the cost of each simulation is significant and consequently it is not desirable to conduct a full nonlocal MFM analysis. To conduct computation for D_{ijkl} for given k and l, one requires as many DNS simulations as the number of degree of freedom of the RANS space. Therefore, to reduce the cost of the analysis, we conduct two separate analyses for the anisotropy and nonlocality, both using MFM.

First, we focus on studying the anisotropic nature of the eddy viscosity. However, to focus exclusively on anisotropy, we systematically construct a local approximation of the eddy viscosity operator using the Kramers-Moyal expansion [67], as investigated by Mani and Park [34]. For instance, in a channel flow where dV_1/dx_2 is the only active component of the velocity gradient, the Reynolds stress $\overline{u_2'v_1'}$ in Equation 2.9 can be written as the integral of only D_{2121} component of the eddy viscosity. By considering a Taylor series expansion of dV_1/dx_2 around $y_2 = x_2$, one can re-express the eddy viscosity operator in terms of the following expansion:

$$-\overline{u_2'v_1'}(x_2) = \int D_{2121}(x_2, y_2) \left.\frac{\partial V_1}{\partial x_2}\right|_{y_2} \mathrm{d}y_2 \tag{2.11}$$

$$= \int D_{2121}(x_2, y_2) \left(\left.\frac{\partial V_1}{\partial x_2}\right|_{x_2} + (y_2 - x_2) \left.\frac{\partial^2 V_1}{\partial x_2^2}\right|_{x_2} + \cdots \right) \mathrm{d}y_2 \tag{2.12}$$

$$= \sum_{n=0}^{\infty} D_{2121}^n(x_2) \frac{\partial^{n+1} V_1}{\partial x_2^{n+1}} \tag{2.13}$$

where $D_{2121}^n = \int D_{2121}(x_2, y_2)(y_2 - x_2)^n/n! \mathrm{d}y_2$ represents the n-th spatial moment of the eddy viscosity kernel.

As discussed by Mani and Park [34], the leading term in this expansion encapsulates the local limit eddy viscosity while the subsequent terms characterize finite moments associated with the nonlocal effects. The general form of this leading-order approximation for all components of the Reynolds stress and mean velocity gradient is as below:

$$-\overline{u_i'v_j'}(x_2) = D_{ijkl}^0(x_2) \frac{\partial V_l}{\partial x_k}, \tag{2.14}$$

where $D_{ijkl}^0(x_2)$ is called the leading-order eddy viscosity tensor:

$$D_{ijkl}^0(x_2) = \int D_{ijkl} \mathrm{d}y_2. \tag{2.15}$$

Equation 2.14 would be exact only when $D_{ijkl}(x_2, y_2)$ is local, i.e. $D_{ijkl}(x_2, y_2) = D^0_{ijkl}(x_2)\delta(x_2 - y_2)$ where $\delta(x)$ is a Dirac delta function.

The local eddy viscosity in Equation 2.14 is no longer a scalar value varying in space; it is a fourth-order tensor with 81 coefficients. The tensor representation was suggested by previous researchers including Batchelor [6], but the full quantification has not been conducted to the authors' knowledge.

Equivalently, one can derive this local approximation based on a scaling argument and without resorting to the Taylor series as follows. In this derivation, we do not assume homogeneity in spatial directions for generalization. When momentum mixing is said to be local, regardless of its degree of accuracy, it is implied that the underlying turbulent eddies have a length scale much smaller than the length characterizing the variation of the mean velocity gradient. The former length, is the mixing length, indicating the support of D_{ijkl} around $\mathbf{y} = \mathbf{x}$. Therefore, a local approximation implies that mean velocity gradient should not vary much over the (highly local) support of D_{ijkl}. As a result, the integration in Equation 2.9 can be simplified by assuming a constant mean velocity gradient over that support and taking it out of the integration and re-expressing the integral as:

$$\int D_{ijkl}(\mathbf{x}, \mathbf{y}) \frac{\partial V_l}{\partial x_k}\bigg|_{\mathbf{y}} \mathrm{d}\mathbf{y} \approx \left(\int D_{ijkl}(\mathbf{x}, \mathbf{y}) \mathrm{d}\mathbf{y} \right) \frac{\partial V_l}{\partial x_k} = D^0_{ijkl}(\mathbf{x}) \frac{\partial V_l}{\partial x_k} \tag{2.16}$$

where the same D^0_{ijkl} appears again, denoting the local and anisotropic eddy viscosity tensor. Intuitively, representing the spatial integral of D_{ijkl}, D^0_{ijkl} essentially relegates the finite span of the eddy viscosity kernel into a Dirac delta function and thus assumes the entire Reynolds stress can be approximated based on a local velocity gradient. To simplify, we can write our anisotropic local eddy viscosity model as follows:

$$-\overline{u_i' v_j'}(\mathbf{x}) = D^0_{ijkl}(\mathbf{x}) \frac{\partial V_l}{\partial x_k}. \tag{2.17}$$

For a subset of the flow systems, we conduct investigation focuses on the nonlocality of the eddy viscosity. As conducting MFM to measure the full kernel can be costly for complex turbulent flow systems, we focus on calculating a subset of tensorial kernel components, specifically the kernel components that are multiplied to $\partial V_1/\partial x_2$ in Equation 2.9. The computed tensorial kernel components are $D_{ij21}\,(x_2, y_2)$ and they are associated with the Reynolds stresses which correspond to the velocity gradient $\partial U_1/\partial x_2$, the only velocity gradient appearing in the RANS closure for a channel flow. The detailed steps on how to measure eddy viscosity kernel using MFM is discussed in Appendix D.

2.2.3 Application of Macroscopic Forcing Method

The next step involves how we actually compute the leading order eddy viscosity tensor and the eddy viscosity kernel. MFM enables a direct measurement of D_{ijkl} and D^0_{ijkl} via numerical solutions to the generalized momentum transport equation [34]. In this methodology, the momentum transport equation is manipulated via macroscopic forcing to allow quantitative probing of $D_{ijkl}(\mathbf{x}, \mathbf{y})$ by

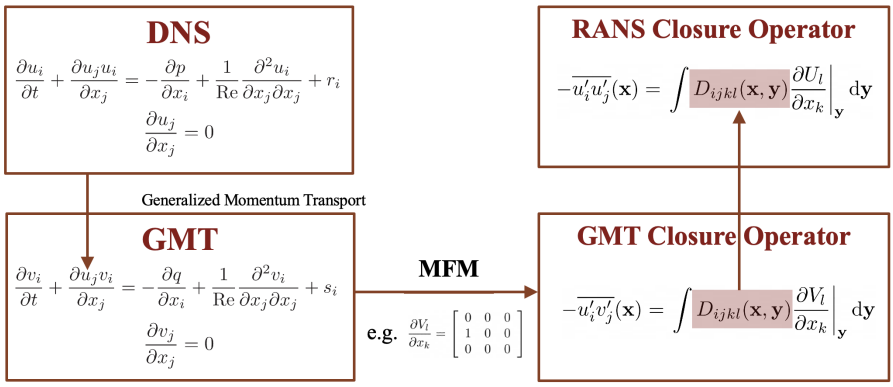

Figure 2.1: Schematic of the MFM analysis.

examining Reynolds stresses in response to various scenarios of mean velocity gradients. To keep this probing specific to the target flow, the advective velocity in the momentum transport equation is pre-selected and donated by the DNS. To allow direct probing of the local anisotropic eddy viscosity tensor, which is the coefficient of the leading term in the expansion of the eddy viscosity operator, one needs to apply a forcing that maintains a spatially uniform mean velocity gradient, and observe that Equation 2.9 reduces to Equation 2.17 exactly. Then, the specific components of D^0_{ijkl} can be computed by post-processing the Reynolds-stresses obtained from different, linearly independent forcing scenarios. In this case, each forcing is designed based on the inverse MFM approach discussed in [34] to maintain only one component of the mean velocity gradient tensor to be nonzero and spatially constant.

Figure 2.1 illustrates how we conducted our MFM analysis using an example case from a channel flow. To apply MFM, we start with two sets of solvers: one for the NS equations and the other for GMT. At each time step, we solve the NS equation to obtain the velocity field u_i and feed it as the advecting velocity to the GMT solver. For the GMT equations, we force the Reynolds-averaged GMT variable V_i to be a specific value in order to acquire certain information about the eddy viscosity. A forcing field s_i that results in $V_1 = x_2$ and $V_2 = V_3 = 0$ generates GMT data from which we can extract the leading-order eddy viscosity D^0_{ij21}. More specifically, D^0_{2121} can be obtained by post-processing $\overline{u_2' v_1'}$ from this GMT simulation, and re-evaluating Equation 2.11 - 2.13 to observe:

$$-\overline{u_2' v_1'}(x_2) = \int D_{2121}(x_2, y_2) \left.\frac{\partial V_1}{\partial x_2}\right|_{y_2} \mathrm{d}y_2 \overset{V_1 \equiv x_2}{=} \int D_{2121}(x_2, y_2)\, \mathrm{d}y_2 = D^0_{2121}(x_2) \tag{2.18}$$

As discussed, the macroscopic operator of the Reynolds-averaged GMT and the RANS operator of NS are identical. Therefore, D^0_{2121} corresponds to the standard eddy viscosity ν_T used in the Boussinesq approximation in RANS models. Likewise, we can compute other components of the

leading-order eddy viscosity tensor using different selections of the macroscopic forcing field, s_i, such that other components of the mean velocity gradient are activated.

Additionally, the same setup shown in Figure 2.1, can be used to compute the full kernel of eddy viscosity. The main difference is to apply macroscopic forcings that would generate mean fields in the form of Dirac delta functions. For example, a macroscopic field, s_i, that sustains $V_1(x_2) = \delta(x_2 - y_2)$, would result in GMT data from which we can extract $D_{ij21}(x_2, y_2)$, by merely post processing the $\overline{u_i' v_j'}$ data. This specific choice of forcing would result in data similar to those obtained by Hamba [20], with the difference that Hamba used only the symmetric portion of the momentum flux tensor in order to ensure symmetry of the Reynolds stresses. As we shall see, GMT does not produce symmetric eddy viscosity kernels and thus $D_{ijkl} \neq D_{jikl}$. This is intuitively understandable noting that D_{ijkl} quantifies the rate of mixing of the mean j-momentum by the i-component of the velocity fluctuations while D_{jikl} quantifies the rate of mixing of the mean i-momentum by the j-component of the velocity fluctuations. Since in this framework, momentum and velocity fields can be quantitatively different, the symmetry does not hold. Likewise, this asymmetry propagates to the Kramers-Moyal expansion of the eddy viscosity operator, and as we shall see, even the leading-order eddy viscosities are not symmetric.

Lastly, we note that the macroscopic forcing procedure used in this work is an inverse forcing method as discussed by Mani and Park [34], since we explicitly set the desired mean momentum field V_i for each GMT simulation, as opposed to setting the macroscopic forcing field.

2.3 Channel Flow

Figure 2.2 shows the schematics of the channel flow and its coordinate system where the flow is bounded by top and bottom walls spaced 2δ apart. We denote the Cartesian coordinates x_i, where x_1 is the streamwise direction, x_2 is the wall-normal direction, and x_3 is the spanwise direction. We include forcing $r_i = (1, 0, 0)$ in Equation 2.1 for normalized mean pressure gradient. The dimensionless spatial coordinates are normalized by δ, and Re_τ represents the flow Reynolds number defined based on δ and the friction velocity $u_\tau = \sqrt{\tau_w/\rho}$ where τ_w is the mean wall shear stress balancing the force due to the mean pressure gradient and ρ is the fluid density. We study a channel flow at Re_τ=180.

We adapt MFM solver to a three-dimensional incompressible NS solver originally developed by [7] and modified by [55]. The present DNS uses the fractional step method with semi-implicit time advancement [26]. For the temporal difference scheme, we use second order Crank-Nicholson for the wall-normal diffusion and Adams-Bashforth for the rest of the terms. The solver uses a second-order finite spatial discretization on a staggered mesh [39]. Also, we use a uniform grid in the streamwise and spanwise directions and grid-stretching in the wall-normal direction. The domain is periodic both in the spanwise and the streamwise directions, and the no-slip boundary condition is applied

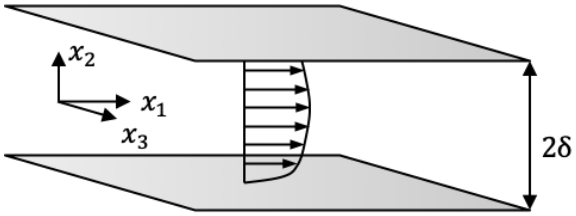

Figure 2.2: Schematic of the channel flow.

at the two walls.

The numerical setup for the GMT solver is almost identical to that of DNS, except for two differences. The first is that GMT obtains the background velocity from the NS solver at every time step. The other difference is that GMT utilizes macroscopic forcing, in order to maintain a desired macroscopic momentum field $V_i(x_2)$. To be most rigorous, the selected macroscopic forcing, $s_i(x_2)$, must be independent of time. Likewise, the resulting mean velocity field needs to match the pre-set $V_i(x_2)$ only after time averaging. However, constraining the simulations in this fashion, would require expensive iterations over which the entire simulation must be repeated after each adjustment of $s_i(x_2)$. To avoid this cost, in our implementation, we computed ensemble averages by averaging fields only in the x_1 and x_3 directions, and we constrained $s_i(x_2)$ at each time step such that $V_i(x_2)$ is matched to the pre-set $V_i(x_2)$ at each time step.

However, in this implementation the resulting $s_i(x_2)$ is not perfectly time independent. Due to finite number of samples per time step, fluctuations in time are observed. One remedy to reduce these fluctuations is to increase the number of samples by selecting a longer domain in the x_1 and x_3 directions. We have performed such domain convergence studies in Appendix A indicating the adequacy of the selected domain size in our MFM analysis.

There are two sets of forcings for MFM presented in this work, each corresponding to the analysis of anisotropy and the nonlocality of eddy viscosity (Table 2.1). Within each set, multiple simulations are performed where the macroscopic forcings are varied to reveal different components of the eddy viscosity. The first set uses GMT simulations under different macroscopic forcings to reveal the leading-order eddy viscosity tensor D^0_{ijkl}. We utilize these measurements to understand the anisotropy of the eddy viscosity. The second set probes a subset of the entire eddy viscosity kernel, D_{ij21}, which quantifies the nonlocality of the eddy viscosity in response to the most significant velocity gradient $\partial U_1/\partial x_2$. In addition to the analysis method and the resulting eddy viscosity, Table 2.1 presents the number of total DNSs in each set, the domain size, the spatial resolution, and the sampling times. For the first set, only nine DNSs are needed corresponding to $k, l \in \{1, 2, 3\}$, and for the second set, MFM analyses require a set of simulations with the number of the macroscopic degree of freedom. The results of each set are discussed in Sections 3 and 4 respectively, and the detailed simulation setup of each set is discussed in Appendix B and D, respectively.

Analysis	Eddy Viscosity	Number of DNS's	$L_1 \times L_2 \times L_3$	$N_1 \times N_2 \times N_3$	Tu_τ/L_2
Anisotropy	$D^0_{ijkl}(x_2)$	9	$2\pi \times 2 \times \pi$	$144 \times 144 \times 144$	750
Nonlocality	$D_{ij21}(x_2, y_2)$	145	$2\pi \times 2 \times \pi$	$144 \times 144 \times 144$	500

Table 2.1: Analysis strategy, corresponding eddy viscosity component, the number of simulations, domain size, grid points, and sampling time for the channel flow.

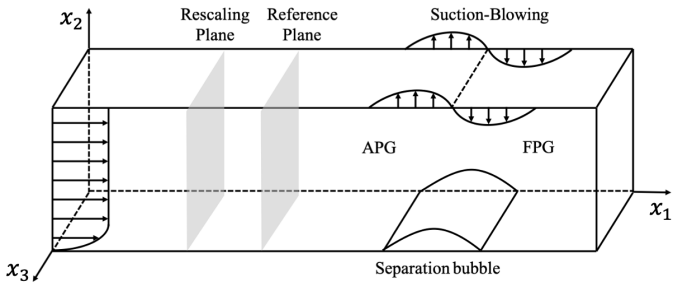

Figure 2.3: Schematic of SBL.

2.4 Separated Boundary Layer

The canonical separated boundary layer (SBL) for this study is a pressure-induced separation in a flat-plate turbulent boundary layer [62, 40, 1, 73], with the schematic of the flow and its coordinates shown in Figure 2.3. Cartesian coordinates are denoted by x_1 in the streamwise direction, x_2 in the wall-normal direction, and x_3 in the spanwise direction. The instantaneous velocity fields are denoted by u_i, and the spanwise and temporally averaged velocity fields are denoted by U_i. This flow is an incompressible boundary layer flow on a flat plate with a prescribed suction and blowing velocity distribution U_2^{top} for the top boundary condition. This suction and blowing velocity distribution induces an adverse pressure gradient (APG) that shifts to a favorable pressure gradient (FPG) that generates a circulation bubble. We conduct extensive DNS of such a flow at $\text{Re}_\theta = 350$, closely following simulation setups by Abe and Wu et al. [3, 1, 73].

At the inlet, we impose a turbulent boundary layer at Reynolds number of $\text{Re}_\theta = 225$ where θ is the momentum thickness. When the flow reaches $\text{Re}_\theta = 350$, we set this location to be the reference plane, and the normalized coordinate system is translated to set the origin at the reference plane. The reference plane is located at $163\theta_0$ away from the inflow in the streamwise direction where θ_0 is the momentum thickness at the reference plane. Unless stated otherwise, all the parameters are normalized by θ_0 and the far-field streamwise velocity $U_{1,\infty}$. Between the inlet and the reference plane, the rescaling plane is used to collect data for inflow generation. This plane is located at $x_1 = -84$. The generation of the inflow is discussed further in this section.

For the numerical simulation, we modify the incompressible Navier-Stokes solver originally developed by Lozano-Durán for turbulent boundary layers [32]. For spatial discretization, we use

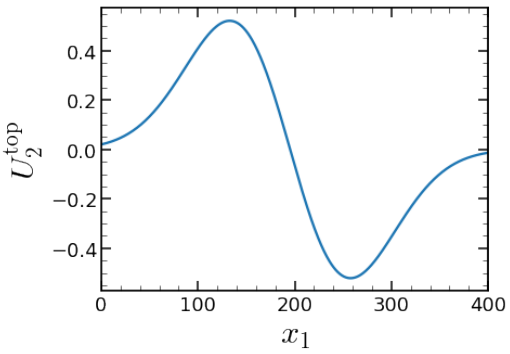

Figure 2.4: Imposed top velocity u_2^{top} for SBL.

second-order finite differences and a staggered mesh. For temporal discretization, we use second-order Runge-Kutta and a fractional step method. Table 2.2 shows the number of grid points, N_i; domain size, L_i; spatial resolution in wall units, Δx_i^+; and sampling time, T.

$N_1 \times N_2 \times N_3$	$L_1 \times L_2 \times L_3$	$\Delta x_1^+ \times \Delta x_2^+ \times \Delta x_3^+$	TU_0/θ_0
$840 \times 600 \times 386$	$605\theta_0 \times 80\theta_0 \times 120\theta_0$	$13 \times (0.35 \sim 9.4) \times 5.5$	7645

Table 2.2: Domain size, grid points, spatial resolution, and sampling time for SBL.

For the boundary conditions, we mostly follow Abe's work [1], but the generation of the inflow is inspired by Wu et al. [73]. For spanwise boundaries, we use periodic boundary conditions. On the bottom wall, we use a no-slip boundary condition. For the outlet, we use a convective boundary condition with convective velocity of $U_{1,\infty}$. Details for the top boundary conditions and the inflow generation are stated below.

For the top boundary condition, we use a suction and blowing condition. Following the work of Abe [1, 2], the top boundary condition is shown in Figure 2.4 and the equation governing the top suction and blowing velocity, u_2^{top}, is the following:

$$u_2^{\text{top}} = u_2^{\max} \times \sqrt{2} \times \left(\frac{x_c - x_1}{\sigma}\right) \exp\left(\psi - \left(\frac{x_c - x_1}{\sigma}\right)^2\right) \tag{2.19}$$

where $u_2^{\max} = 0.3325$, $x_c = 10^5/2^9$, $\sigma = 80\sqrt{2}\left(5^2/2^5\right)$, and $\psi = 0.95$. The suction and blowing boundary condition presented in Equation (2.19) starts from $x_1 = -35.4$. For regions upstream of $x_1 = -35.4$ the turbulent boundary layer correlation for displacement thickness is used to set the wall-normal velocity on the top boundary, leading to a smooth wall-normal boundary condition and turbulent boundary layer generation near the inlet [70]. This transition ensures a proper turbulent boundary layer at the rescaling plane and smooth transition of the top boundary condition from a turbulent boundary layer to a separated boundary layer. For the chordwise velocity, the zero

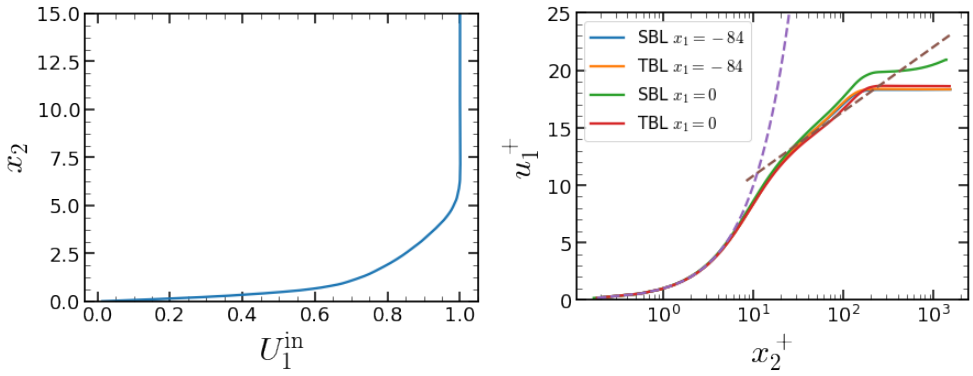

(a) U_1 at the inlet

(b) Mean velocity near wall

Figure 2.5: Imposed mean velocity at the inflow boundary, and the mean velocity in wall units for SBL and TBL.

spanwise vorticity condition, $\partial u_2/\partial x_1 - \partial u_1/\partial x_2 = 0$, is used. For the spanwise velocity, the zero Neumann condition $\partial u_3/\partial x_2 = 0$ is used.

For the inlet boundary condition, we use the Lund recycling and rescaling condition [33] with mean turbulent boundary layer profile. The recycling and rescaling inflow boundary condition is used to determine the fluctuating part of the velocity. The mean inlet velocity is a fixed profile prescribed based on Spalart's results [59] at $Re_\theta = 300$. Their U_1 field is scaled to match $Re_\theta = 225$ (Figure 2.5(a)) and the U_2 field is computed using similarity of the boundary layer velocity profile. In addition, we add a spanwise shift of $\Delta x_3 = L_3/2$ where L_i is the domain size in each direction to remove the artificial correlation in the turbulent structures from the rescaling method [63]. The location of the rescaling plane is at $x_1 = -84$ to ensure that the fully-developed turbulent boundary layer (TBL) is fed into the rescaling plane and the rescaling is unaffected by the suction and blowing boundary condition. Figure 2.5(b) shows the streamwise velocity variation in the wall-normal direction expressed in wall units. Two locations are chosen, the rescaling plane, $x_1 = -84$, and the reference plane, $x_1 = 0$. Also, the solid lines represent the mean velocity profiles of the SBL at $x_1 = -84$ (blue), TBL at $x_1 = -84$ (orange), SBL at $x_1 = 0$ (green), and TBL at $x_1 = 0$ (red), and the dashed lines represent $u_1^+ = x_2^+$ (purple) and $u_1^+ = (1/0.41)\log(x_2^+) + 5.2$ (brown). To ensure that the suction and blowing condition does not affect the profile at the rescaling plane, these plots are compared against the profiles obtained from simulation of the corresponding attached turbulent boundary layer (TBL) without imposing the suction and blowing condition.

To visualize the instantaneous flow structures, Figure 2.6(a) shows an iso-surface of the Q-criteria in the SBL where Q-criteria is defined as the following:

$$Q = -\frac{1}{2}\frac{\partial u_j}{\partial x_i}\frac{\partial u_i}{\partial x_j} = \frac{1}{2}\left(\Omega_{ij}\Omega_{ij} - S_{ij}S_{ij}\right) \tag{2.20}$$

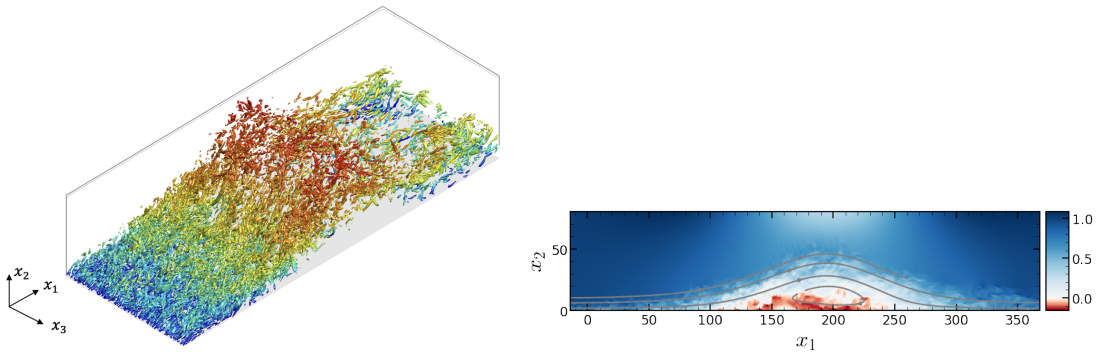

(a) (b)

Figure 2.6: DNS statistics for SBL: (a) iso-surface of Q-criterion, and (b) an instantaneous streamwise velocity field with the mean streamlines.

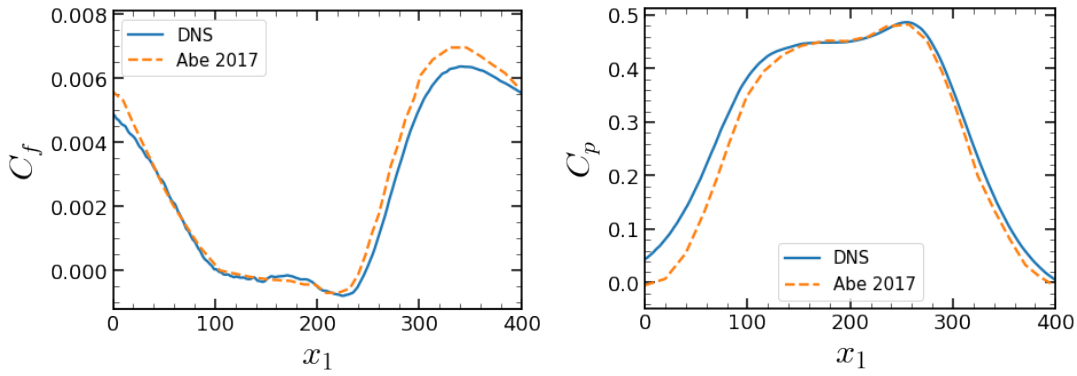

(a) Friction coefficient (b) Pressure coefficient

Figure 2.7: DNS statistics for SBL: (a) the friction coefficient, and (b) the pressure coefficient.

where Ω_{ij} is the rotation rate tensor, $\Omega_{ij} = 1/2\,(\partial u_i/\partial x_j - \partial u_j/\partial x_i)$, and S_{ij} is the strain rate tensor, $S_{ij} = 1/2\,(\partial u_i/\partial x_j + \partial u_j/\partial x_i)$. The given figure represents the iso-surface at $Q = 0.00414$. The color represents the wall-distance, and we note the full formation of the separation bubble. Figure 2.6(b) shows the instantaneous streamwise velocity with the mean velocity streamlines plotted on top. The red color represents negative streamwise velocity and shows a region of backflow within the separation bubble.

Figure 2.7 compares the friction coefficient, C_f, and the pressure coefficient, C_p, from our DNS results (blue solid line) to the results of Abe [1] (orange dashed line). Our DNS results are very consistent with those of Abe's with small differences. These differences arise from the following alterations in the simulations between ours and Abe's. Firstly, the Reynolds numbers at the reference plane, $x_1 = 0$, in our simulation is $\mathrm{Re}_{\theta_0} = 350$, whereas in the Abe's work, the closest Reynolds number is $\mathrm{Re}_{\theta_0} = 300$ (Figure 2.7). Secondly, the inflow generation differs between our simulations.

We follow the approach for the inflow generation from the work of Wu et al. [73] where we have an extended inflow generation region before the reference plane. This allows smoother transition from a turbulent boundary layer to a separated boundary layer. Therefore, this leads to influence of the top boundary condition before the flow reaches the reference plane in our flow setup, which induces the C_f and C_p differences at the reference plane. For instance, in the work of Wu et al. [73], a similar pattern of lower C_f at the reference plane is observed. Therefore, the differences arise from the small variations in the simulation setups, and we see consistent results with the reference work otherwise.

We perform the aforementioned analysis on the canonical separated boundary layer. For these simulations, an incompressible Navier-Stokes solver is used for the donor simulation, and the same solver is modified to generate discretely-consistent MFM solutions to the generalized momentum transport equation for the same flow field. Given that the resulting flow field is statistically two-dimensional, only a subset of components of the eddy viscosity tensor need to be measured by the MFM simulations to conduct RANS simulation. Specifically, we measure statistically relevant components of the eddy viscosity tensor for RANS, which are D^0_{ij11}, D^0_{ij12}, D^0_{ij13}, D^0_{ij21}, D^0_{ij22}, and D^0_{ij23}, where $i, j \in \{1, 2, 3\}$.

In addition, for SBL, we calculate the solution to the RANS equation using the directly measured eddy viscosity to represent the closure term. The adopted RANS equation in this case is written as:

$$\frac{\partial U_i}{\partial t} + \frac{\partial U_j U_i}{\partial x_j} = -\frac{\partial P}{\partial x_i} + \frac{1}{\mathrm{Re}} \frac{\partial^2 U_i}{\partial x_j \partial x_j} + \frac{\partial}{\partial x_j} D^0_{ijkl} \frac{\partial U_l}{\partial x_k} \tag{2.21}$$

$$\frac{\partial U_j}{\partial x_j} = 0 \tag{2.22}$$

For the numerical simulation for this modified RANS, we use incompressible RANS solver which uses pre-computed eddy viscosity and only advances two-dimensional velocity fields. For spatial discretization, we use second-order finite differences and a staggered mesh. For temporal discretization, we use second-order Runge-Kutta. The grid-size is identical to that of the DNS setting.

2.5 Separated Boundary Layer with Sweep

We apply MFM to a separated boundary layer with spanwise sweep (SBLS) across the bubble. The flow is a separated and rapidly reattached turbulent boundary layer over an idealized 35° infinite sweep as shown in Figure 2.8. The DNS set-up follows the works from the literature with and without sweep [62, 40, 2, 13, 14], and is similar to our previous work for SBL [41] for a meaningful comparison of the anisotropic eddy viscosity tensor. The flow consists of a suction-blowing velocity distribution along the upper boundary of the domain to induce an adverse-to-favorable pressure gradient, leading to generation of a separation bubble on a flat plate. Also, a constant spanwise flow is imposed on the top boundary to include the sweep effect. The Reynolds number for the simulation

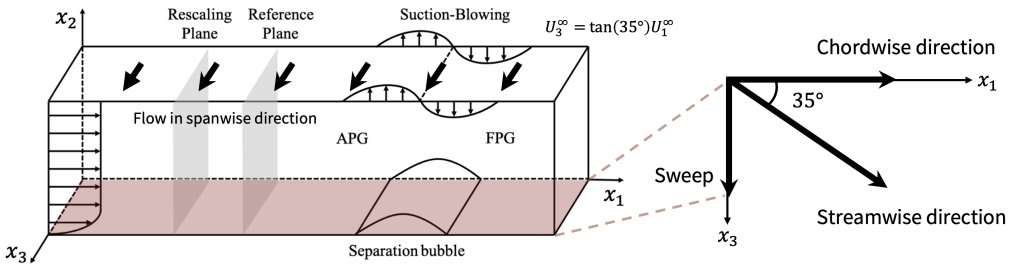

Figure 2.8: Schematic of SBLS.

is $Re_{\theta_0} = 350$, where θ_0 is the momentum thickness of an attached boundary layer defined at some distance upstream of the separation bubble. We denote x_1 direction as chordwise direction and the new primary flow direction as the streamwise direction. Also, x_2 is the wall-normal direction and x_3 is the spanwise direction. While the instantaneous flow is three dimensional and time dependent, the mean flow field is two-dimensional (defined in $x_1 - x_2$ plane) and steady but with all three components of the mean velocity remaining active.

To understand the mixing effects of the sweep, we match the chordwise velocity component of the SBLS to that of the streamwise velocity component of separated boundary layer without sweep (SBL). We closely follow the numerical parameters from our previous SBL work with two main differences accounting for the physical changes of these two flows. The first difference in SBLS is that the top suction and blowing boundary condition is closer to the inlet. Like SBL, we impose a turbulent boundary layer at Reynolds number of $\mathrm{Re}_\theta = 225$ at the inlet and we set the location of $\mathrm{Re}_\theta = 350$ the reference plane. However, unlike SBL where the reference plane is located at $163\theta_0$ away from the inlet in the chordwise direction, the reference plane of SBLS is location at $109\theta_0$ away from the inlet. Following Coleman et al. [14], this change is chosen to account for different growth rates of the boundary layers and to ensure that the momentum thickness is identical at the center of the suction and blowing boundary condition where suction transitions to blowing. We can estimate this location change of the top boundary condition using the empirical growth rate [75] in the projected system prior to the actual simulation. Figure 2.9 shows a top view of the SBL and SBLS simulations. L_s refers to the distance from the inlet to the center of the top suction and blowing boundary condition in SBLS and L refers to that of SBL. s represents the streamwise direction of SBLS; $s = x_1/\cos\alpha$ where α is the sweep angle. U_s is the streamwise velocity of SBLS and U_1^∞ is the streamwise velocity of SBL. The relation between U_s and U_1^∞ is $U_s = U_1^\infty/\cos\alpha$. Using empirical momentum thickness growth rate, momentum thickness of SBLS, θ_s, becomes the following:

$$\theta_s \sim \frac{s}{Re_s^{1/7}} \sim \frac{s}{\left(\frac{U_s s}{\nu}\right)^{1/7}} \sim \frac{\frac{x_1}{\cos\alpha}}{\left(\frac{\frac{U_1^\infty}{\cos\alpha}\frac{x_1}{\cos\alpha}}{\nu}\right)^{1/7}} \sim \frac{x_1}{Re_{x_1}^{1/7}}(\cos\alpha)^{-5/7} \tag{2.23}$$

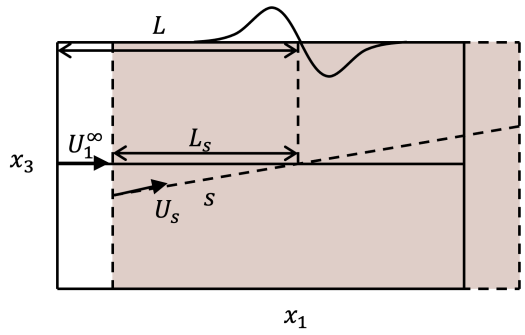

Figure 2.9: Schematic for the boundary layer growth.

Since we want the momentum thickness at the inlet and the center of the suction and blowing boundary condition to be the same, we impose $\Delta\theta = \Delta\theta_s$. Then, the relation between L_s and L becomes $L_s/L = (\cos\alpha)^{5/6}$. Using this relation, we moved the top boundary condition to upstream using $\alpha = 35°$, and the resulting value is $L_s/L \simeq 0.846$. As comparison, [14] used $L_s/L \simeq 0.887$. Unless stated otherwise, all the parameters are normalized by θ_0 and the far-field chordwise velocity $U_{1,\infty}$.

The second difference is that the there are more grid points in the chordwise direction. Due to the sweep, the elongated hairpin vortices near the wall that were aligned to the chordwise direction are now tilted to the spanwise direction [14]. This change causes shortened effects of the turbulent eddies in the chordwise direction, requiring more resolution in x_1 direction. Table 2.3 shows the number of grid points, N_i; domain size, L_i; spatial resolution in wall units, Δx_i^+; and sampling time, T.

$N_1 \times N_2 \times N_3$	$L_1 \times L_2 \times L_3$	$\Delta x_1^+ \times \Delta x_2^+ \times \Delta x_3^+$	TU_0/θ_0
$1400 \times 600 \times 386$	$605\theta_0 \times 80\theta_0 \times 120\theta_0$	$7.8 \times (0.35 \sim 9.4) \times 5.5$	5921

Table 2.3: Domain size, grid points, spatial resolution, and sampling time for SBLS

For the numerical simulation, we modify the incompressible Navier-Stokes solver from the SBL [41]. For spatial discretization, we use second-order finite differences and a staggered mesh. For temporal discretization, we use second-order Runge-Kutta and a fractional step method. For the boundary conditions, the top boundary condition is the same between SBL and SBLS for the chordwise component and the wall-normal component, and a finite sweep, a Dirichlet condition $u_3 = \tan(35°)$, is added for the spanwise component as shown in Figure 2.10. On the bottom wall, we use a no-slip boundary condition. For the outlet, we use a convective boundary condition with convective velocity of $U_{1,\infty}$.

For the inlet boundary condition, we use the Lund recycling and rescaling condition [33] with

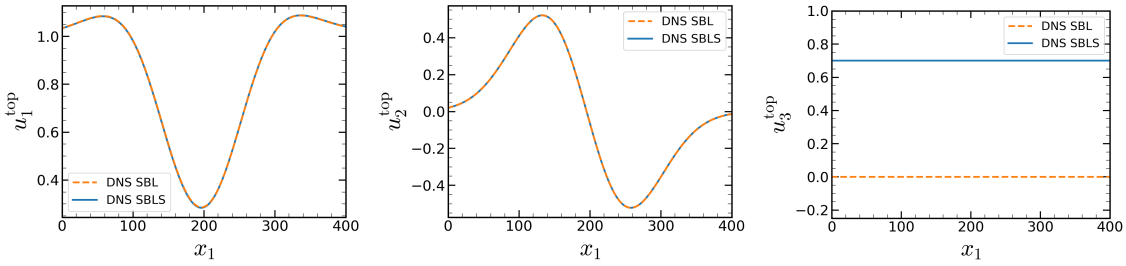

(a) u_1^{top} (b) u_2^{top} (c) u_3^{top}

Figure 2.10: Top boundary condition U_i^{top} for SBL and SBLS.

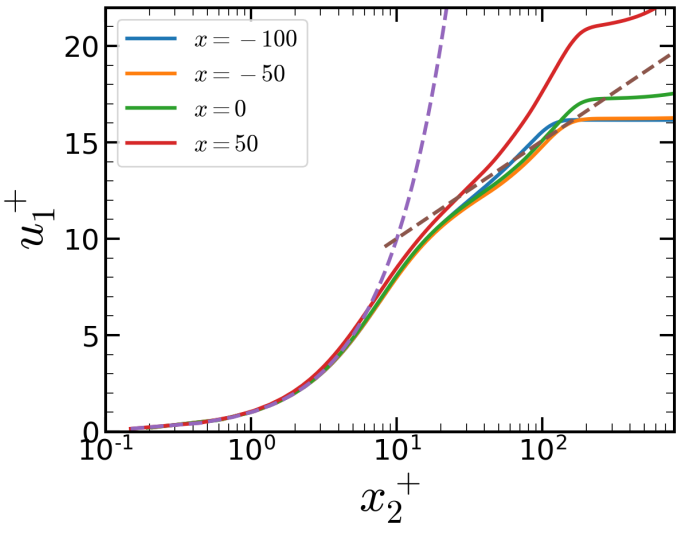

Figure 2.11: DNS statistics for SBLS: mean velocity near wall.

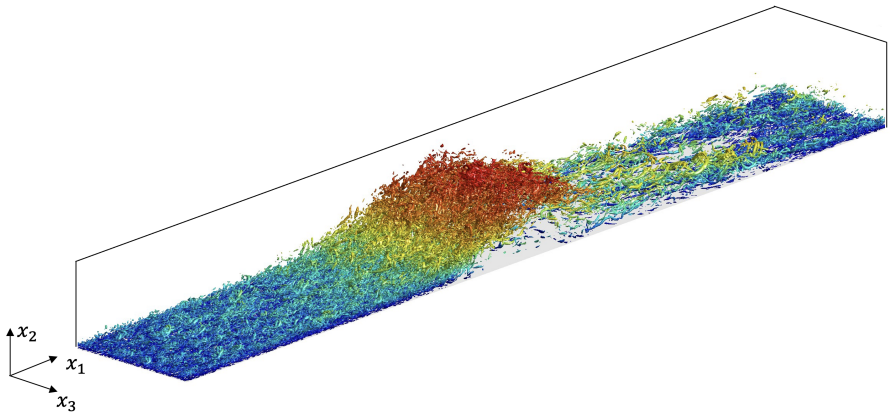

Figure 2.12: DNS statistics for SBLS: iso-surface of Q-criterion for SBLS.

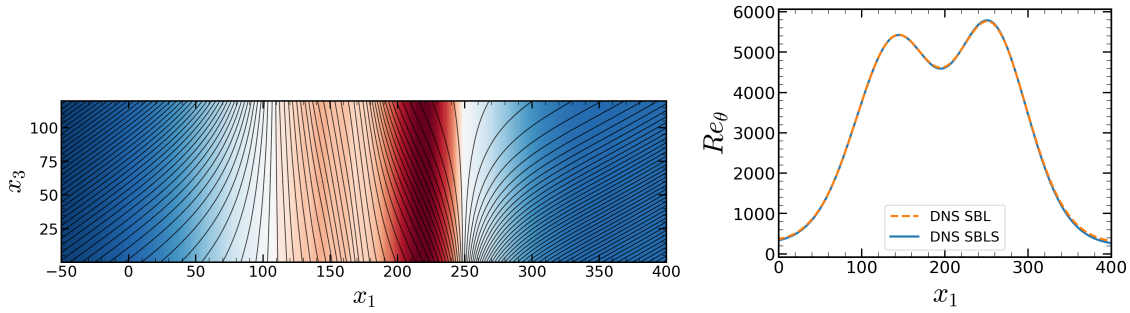

(a) Frictionline (b) Re_θ

Figure 2.13: DNS statistics for SBLS: (a) instantaneous streamwise velocity field one point away from the wall with the mean frictionline, and (b) Reynolds number based on the momentum thickness.

mean turbulent boundary layer profile. The imposed mean turbulent boundary layer is same as the SBL simulation with $Re_\theta = 225$ (Figure 2.5(a)). The recycling methods is identical to that of the SBL simulation with only one difference. Since we moved the top boundary condition to upstream, the rescaling plane is also moved to upstream. The rescalig plane for SBLS is located at $x_1 = -31$. Figure 2.11 shows the chordwise velocity variation in the wall-normal direction expressed in wall units. In this figure, the dashed lines represent $u_1^+ = x_2^+$ (purple) and $u_1^+ = (1/k_x)\log(x_2^+) + A_x$ (brown). Due to the added sweep effect, the classical near-wall behavior change. k_x is the modified Von Karman constant where $k_x = k/\sqrt{\cos\alpha}$ and $k = 0.41$. A_x is the modified intercept $A_x = A\sqrt{\cos\alpha} - \log(\cos\alpha)/2k_x$ and $A = 5.2$ [14]. In this figure, we confirm that the turbulent boundary layer is properly generated at $x_1 = -31$.

To visualize the instantaneous flow structures, Figure 2.12 shows an iso-surface of the Q-criteria in the SBLS. The given figure represents the iso-surface at $Q = 0.00414$. The color represents the wall-distance, and we note the full formation of the separation bubble and the shifted turbulent

structures. Figure 2.13(a) shows the instantaneous streamwise velocity collected one point away from the wall with the mean friction line plotted on top. The red color represents negative streamwise velocity and shows a region of backflow within the separation bubble. Also, the frictionline indicate that the flow is originally 35° swept and as it goes near the separation bubble the flow becomes parallel to the separation line. Furthermore, Figure 2.13(b) compare Reynolds number based on the chordwise momentum thickness between SBL and SBLS along x_1. We see that the SBLS flow is properly generated for the fair comparison to the SBL.

To study the eddy viscosity of SBLS, we conduct MFM analysis using a modified version of the incompressible Navier-Stokes solver mentioned earlier. The modification enables the solver to produce discretely-consistent MFM solutions for the generalized momentum transport equation in the same flow field. Since the flow field obtained is statistically two-dimensional, we only need to measure a subset of components of the eddy viscosity tensor using MFM simulations, which are D^0_{ij11}, D^0_{ij12}, D^0_{ij13}, D^0_{ij21}, D^0_{ij22}, and D^0_{ij23}, where $i, j \in \{1, 2, 3\}$.

Chapter 3

Eddy Viscosity in a Turbulent Channel Flow

Materials in this chapter have been published in [42].

This chapter analyzes turbulence in a channel flow at Re_τ=180 using two MFM forcing strategies to precisely decompose the Reynolds stress closure into local and nonlocal operators. The two sets of forcings for MFM, each corresponding to anisotropic and nonlocality analysis (Table 2.1). Each set includes multiple simulations with varying macroscopic forcings to reveal different components of the eddy viscosity kernel. The first set of macroscopic forcings is used to understand the anisotropy of the eddy viscosity by measuring the leading-order eddy viscosity tensor D^0_{ijkl}. The second set of macroscopic forcings focuses on a subset of the eddy viscosity kernel, D_{ij21}, which quantifies the nonlocality of the eddy viscosity in response to the most significant velocity gradient $\partial U_1/\partial x_2$.

3.1 Anisotropy Analysis

In this section, we compute the leading-order eddy viscosity tensor D^0_{ijkl} and focus on the analysis on anisotropy of the eddy viscosity and specifically contrast it to the standard eddy viscosity implied by the Boussinesq model. In addition, we assess dependency of Reynolds stresses on the rate of rotation, examine reconstruction of Reynolds stresses using the leading-order eddy viscosity, and lastly discuss positive definiteness of the leading-order eddy viscosity tensor.

3.1.1 Leading-order Eddy Viscosity Tensor

This section provides the complete set of nonzero values of the leading-order eddy viscosity tensor D^0_{ijkl} for a channel flow. The values are shown in Figures 3.1 to 3.9, and correspond to the eddy viscosity tensor in Equation 2.17. The values that are not shown converge to zero, which was

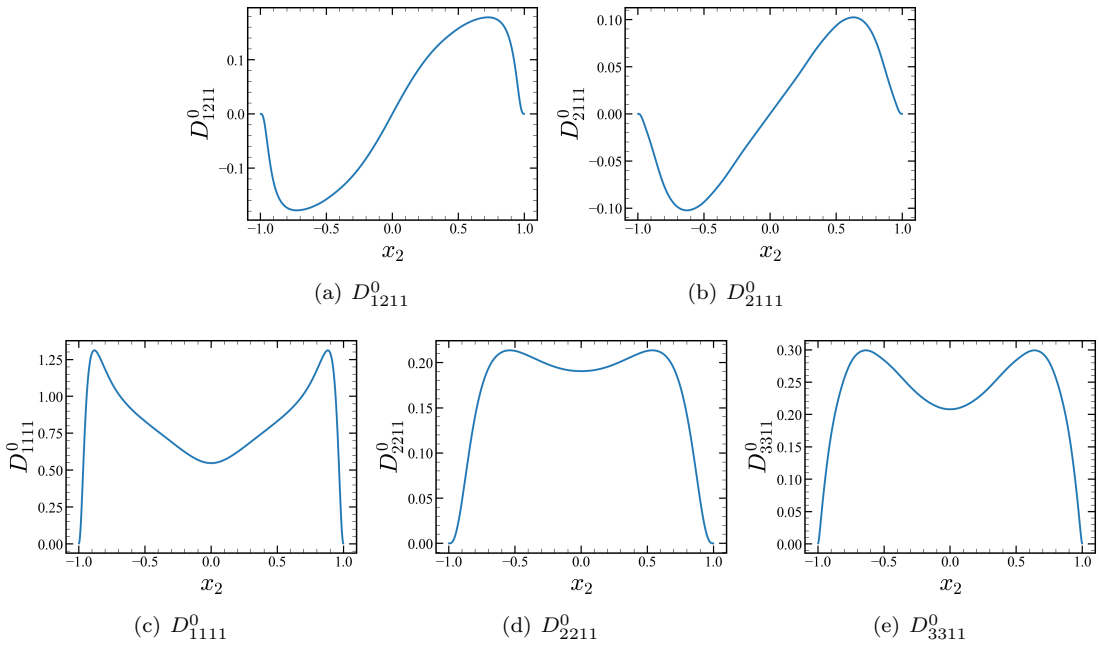

(a) D^0_{1211} (b) D^0_{2111}

(c) D^0_{1111} (d) D^0_{2211} (e) D^0_{3311}

Figure 3.1: Distribution of nonzero D^0_{ij11} for the channel flow.

either evident through the symmetry of the channel or through a decrease in statistical noise as the simulation was run for longer.

The eddy viscosity components can be symmetric or antisymmetric depending on the number of even or odd indices of 2 among the $ijkl$ indices. Additionally, all eddy viscosity components consistently go to zero at the walls. In the following sections, we delve further into important eddy viscosity components and their significance.

3.1.2 Standard Eddy Viscosity

In parallel flows, among all the components of the eddy viscosity tensor, by far the most important component is D^0_{2121} which represents the mixing effect by $\partial U_1/\partial x_2$. This component also corresponds to the standard eddy viscosity ν_T. Figure 3.10 shows the MFM-measured D^0_{2121} across the wall-normal dimension x_2. An important observation here is that the MFM allows us to measure the eddy viscosity at the channel center plane $x_2 = 0$, where the velocity gradient $\partial U_1/\partial x_2$ is zero due to the symmetry of the mean velocity profile. This value is unobtainable in typical approaches—tuning ν_T to $\overline{u_2' u_1'}/(\partial U_1/\partial x_2)$.

Figure 3.11 shows instantaneous field data for the streamwise velocities u_1' and v_1' of the MFM simulation for evaluation of D^0_{2121} at the same instantaneous time. Figures (a) and (b) show the velocity profile over (x_1, x_3) cross-section taken at $x_2 = -0.8492$ ($x_2^+ = 27$) and Figures (c) and (d)

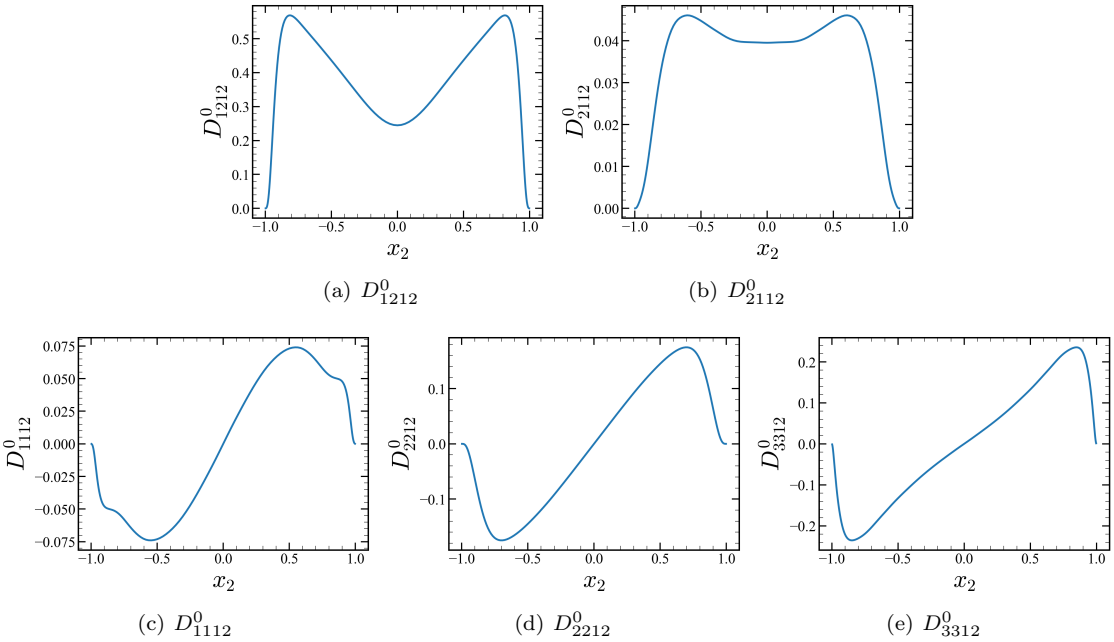

(a) D^0_{1212} (b) D^0_{2112}

(c) D^0_{1112} (d) D^0_{2212} (e) D^0_{3312}

Figure 3.2: Distribution of nonzero D^0_{ij12} for the channel flow.

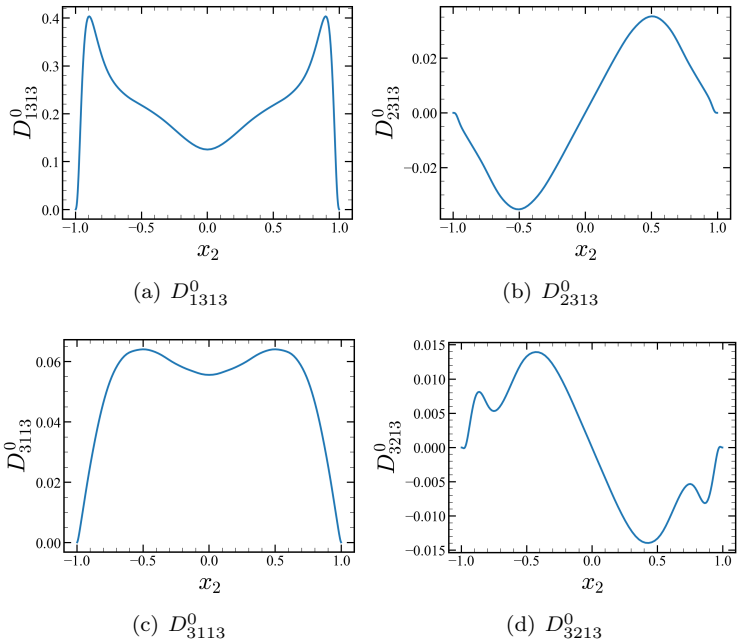

(a) D^0_{1313} (b) D^0_{2313}

(c) D^0_{3113} (d) D^0_{3213}

Figure 3.3: Distribution of nonzero D^0_{ij13} for the channel flow.

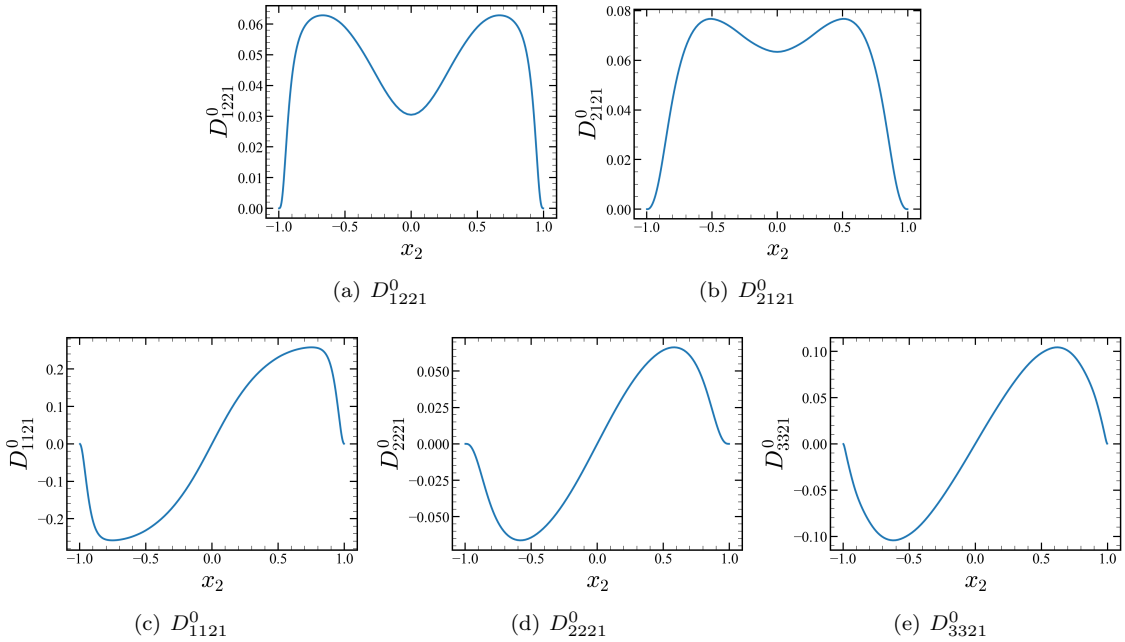

(a) D^0_{1221} (b) D^0_{2121}

(c) D^0_{1121} (d) D^0_{2221} (e) D^0_{3321}

Figure 3.4: Distribution of nonzero D^0_{ij21} for the channel flow.

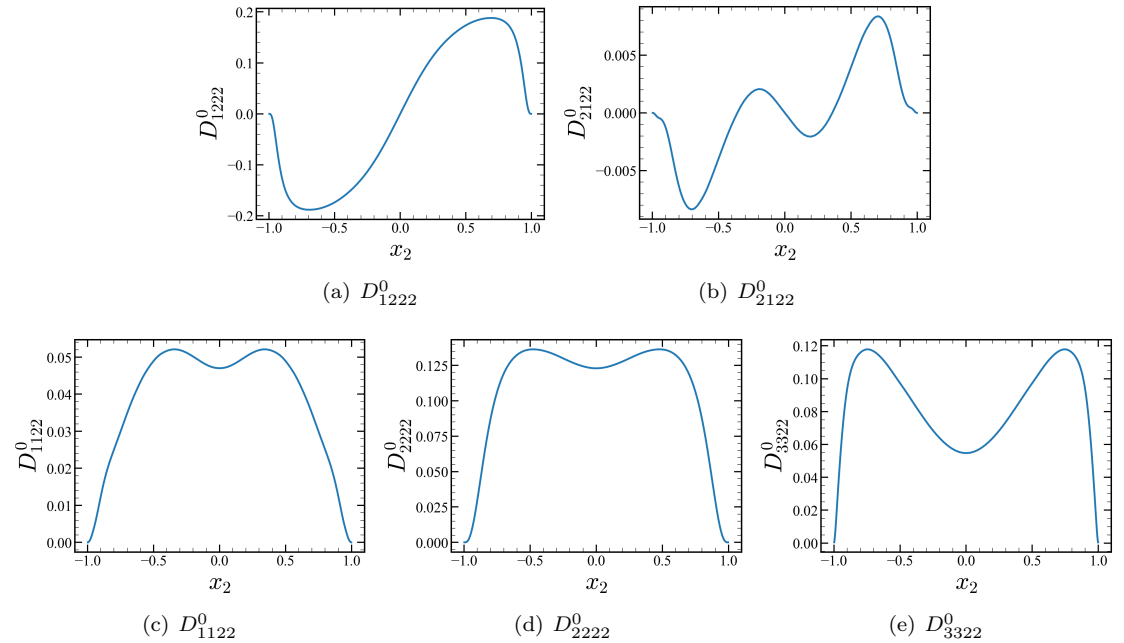

(a) D^0_{1222} (b) D^0_{2122}

(c) D^0_{1122} (d) D^0_{2222} (e) D^0_{3322}

Figure 3.5: Distribution of nonzero D^0_{ij22} for the channel flow.

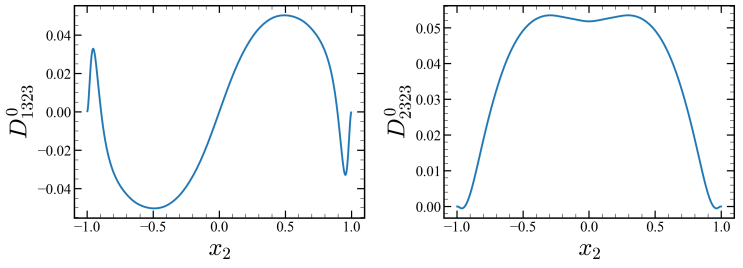

(a) D^0_{1323} (b) D^0_{2323}

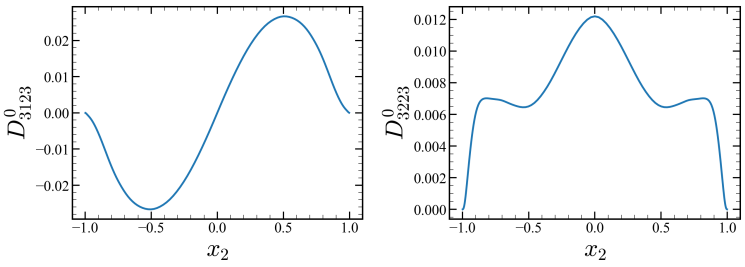

(c) D^0_{3123} (d) D^0_{3223}

Figure 3.6: Distribution of nonzero D^0_{ij23} for the channel flow.

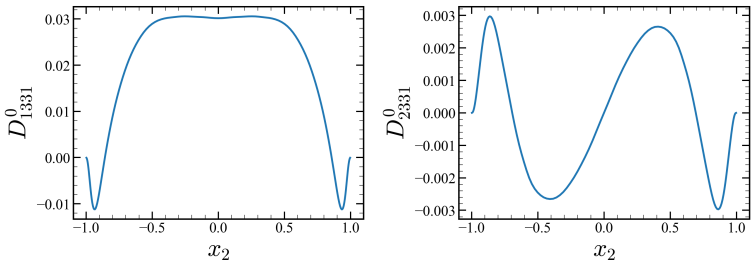

(a) D^0_{1331} (b) D^0_{2331}

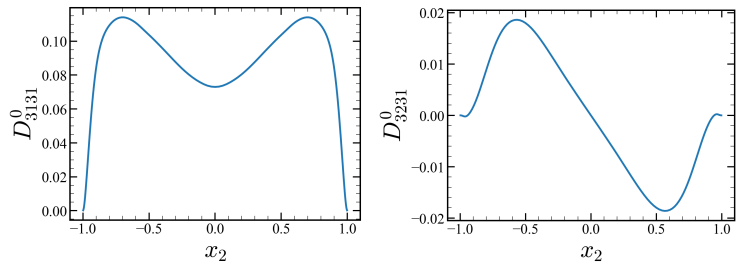

(c) D^0_{3131} (d) D^0_{3231}

Figure 3.7: Distribution of nonzero D^0_{ij31} for the channel flow.

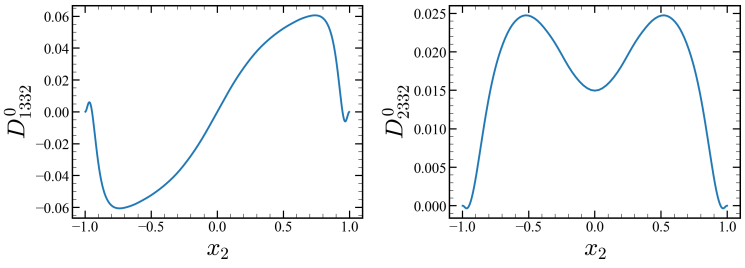

(a) D^0_{1332} (b) D^0_{2332}

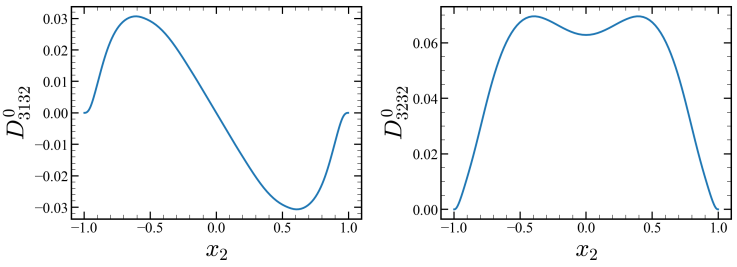

(c) D^0_{3132} (d) D^0_{3232}

Figure 3.8: Distribution of nonzero D^0_{ij32} for the channel flow.

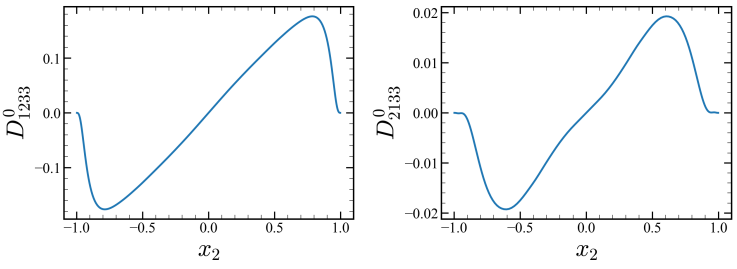

(a) D^0_{1233} (b) D^0_{2133}

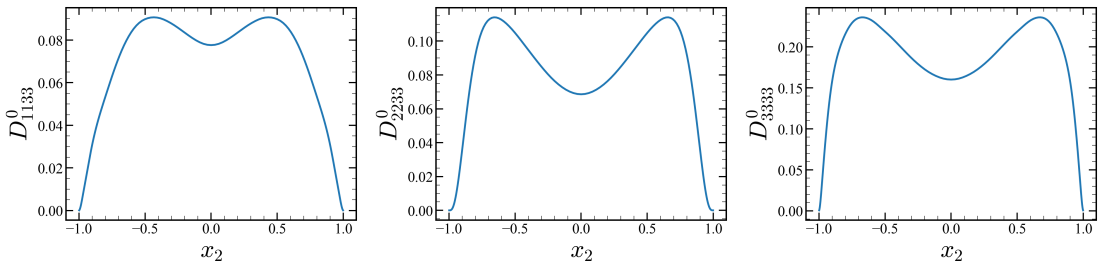

(c) D^0_{1133} (d) D^0_{2233} (e) D^0_{3333}

Figure 3.9: Distribution of nonzero D^0_{ij33} for the channel flow.

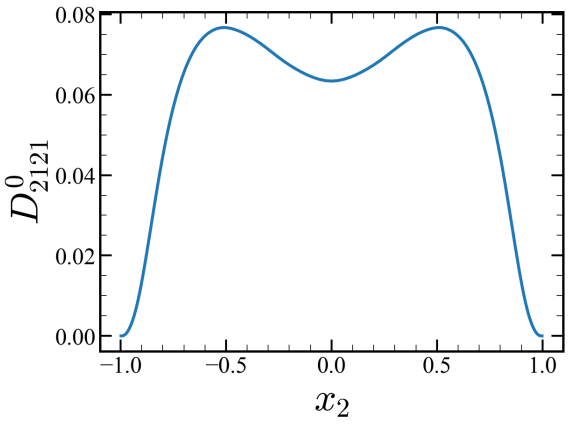

Figure 3.10: Eddy viscosity element D^0_{2121} for the channel flow.

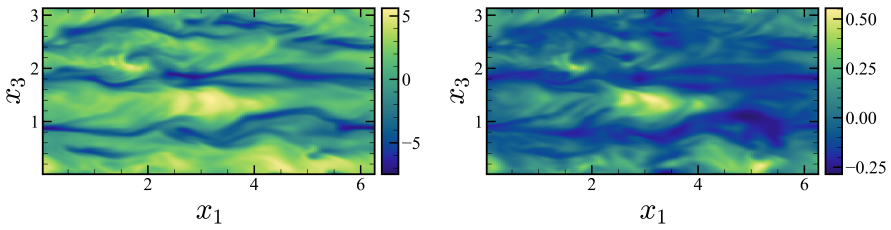

(a) u_1' contour in x_1-x_3 plane

(b) v_1' contour in x_1-x_3 plane

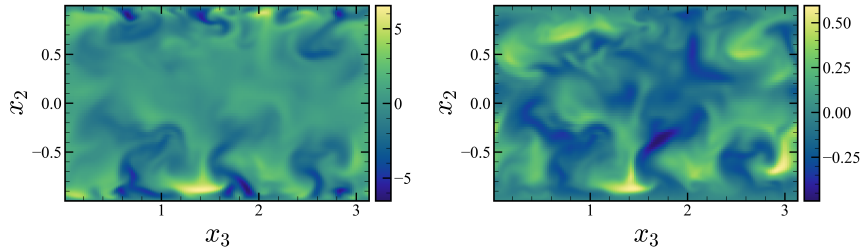

(c) u_1' contour in x_3-x_2 plane

(d) v_1' contour in x_3-x_2 plane

Figure 3.11: Instantaneous velocity contour of u_1' and v_1' in cross-section: (a) and (b) correspond to the cross-section taken at $x_2 = -0.8492$ and (c) and (d) correspond to the cross-section taken at $x_1 = 3.08$. The shown vector field v_i corresponds to a leading-order MFM in which GMT equation is macroscopically forced to achieve $V_1 = x_2$ and $V_2 = V_3 = 0$.

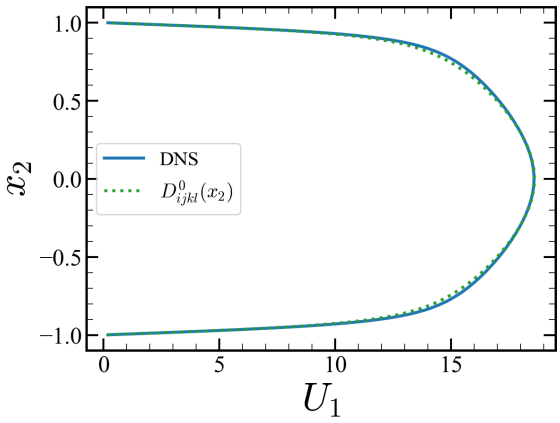

Figure 3.12: RANS prediction using D^0_{2121}: dashed green line, mean velocity prediction using D^0_{2121} and blue solid line, its comparison to the DNS data.

show the velocity profile over (x_3, x_2) cross-section taken at $x_1 = 3.08$. The key feature shown is that even though the forcings for the NS vector field u_i and the GMT vector field v_i are completely different macroscopically, MFM leads to similar features in the u_1' and v_1'. The same qualitative observation holds across all three components of the u_i' and v_i' fields. Furthermore, while for $x_2 < 0$ we observe positive correlation between u_i' and v_i' fields, the sign of correlation flips for $x_2 > 0$. For this specific MFM analysis, the sole difference between u_i' and v_i' fields is in the enforced mean velocity profile. As shown by Mani and Park without forcing [34], GMT would result in v-fields identical to u-fields after a few flow through times regardless of the choice of initial conditions. The case shown in Figure 3.11 corresponds to a forced GMT in which the mean velocity gradient is kept constant $\partial V_1/\partial x_2 = 1$ in order to examine mixing by the leading-order (local limit) eddy viscosity. The observation in Figure 3.11 suggests that mixing of u_1 in turbulent channel flow is dominated by the leading-order effects.

To assess this conclusion quantitatively we next obtain the RANS solution using the measured D^0_{2121} to examine how accurate the leading-order eddy viscosity performs for the prediction of the mean velocity profile. Since the prediction of the mean channel flow only requires one component in the Reynolds stress, we conduct the RANS simulation using D^0_{2121} and compare the predicted solution with that of the DNS. As shown in Figure 3.12, the MFM-based leading-order RANS solution predicts the DNS solution very accurately with an accuracy of 99%. The accuracy is computed with max absolute error $\max\left(U_1^{\mathrm{DNS}} - U_1^{\mathrm{MFM}}\right) / \max\left(U_1^{\mathrm{DNS}}\right)$, where U_1^{DNS} is the streamwise velocity from DNS and U_1^{MFM} is the streamwise velocity predicted from RANS using MFM-measured eddy viscosity D^0_{2121}. This highly accurate RANS prediction indicates that the nature of the mean momentum mixing in the turbulent channel flow is highly local and the RANS solution of this flow can be predicted using the leading-order approximation.

Other parallel flows like the channel flow have only one active velocity gradient, the wall-normal gradient of streamwise velocity. Additionally, for these flows only one component of the Reynolds stress, the shear component, is mixing momentum. Therefore, as far as prediction of the mean flow is concerned, for these flows anisotropy of the eddy viscosity does not play a role; only D_{2121} needs to be accurate. Furthermore, based on the observed MFM analysis, we conclude that the leading-order eddy viscosity, D^0_{2121} provides accurate prediction of momentum mixing, and thus eddy viscosity is local. Therefore, for purely parallel flows, at least for channel flow observed here, both isotropy and locality of the Boussinesq approximation are justified.

Hamba also reported a small subset of the components of the leading-order (local limit) eddy viscosity, through a more expensive method of first computing the full eddy viscosity kernel for those components and then performing integration as in Equation 2.15 [20]. Our result in Figure 3.12 regarding locality of momentum mixing is in contrast to his result (see Figure 4 in [20]). We attribute this difference to the fact that Hamba used the average of D^0_{2121} and D^0_{1221} as the representative local eddy viscosity. This averaging was motivated to enforce symmetric Reynolds stresses. However, conceptually these two eddy viscosities represent different mixing rates: the former represents mixing of the streamwise momentum in the wall normal direction, while the latter represents mixing of the wall-normal momentum in the streamwise direction. As we shall see, while a full eddy viscosity kernel reproduces symmetric Reynolds stresses, the leading-order eddy viscosity causes errors not only in magnitude but also in symmetry of Reynolds stresses.

We next use MFM to quantify other components of D^0_{ijkl}. While these components do not affect prediction of the mean velocity profile in purely parallel flows, they provide an understanding of momentum mixing by this parallel flow, if hypothetical mean momentum gradients were imposed in other directions. Our analysis is motivated by observation of spatially developing turbulent boundary layers, where weak momentum gradient could exist in both streamwise and spanwise directions. These mean gradients induce additional Reynolds stresses, due to components of D_{ijkl} other than D_{2121}. Additionally, it has been observed that turbulent boundary layers have similar hairpin structures in their velocity field as those seen in turbulent channel flows [17], and thus are expected to mix momentum in manners similar to that of a turbulent channel flow. While quantitative differences are expected between the two flows, we expect anisotropy in eddy viscosity observed in turbulent channel flow be at least qualitatively representative of anisotropy encountered in turbulent boundary layers. Given the stringent statistical convergence requirements for MFM simulations, e.g. at least an order of magnitude longer simulations needed than commonly reported DNS, compared to turbulent boundary layers, turbulent channel flows have the advantage of cheaper runtime per time step and availability of additional homogeneous direction for statistical convergence.

3.1.3 Quantifying Anisotropy

We computed all other components of the anisotropic eddy viscosity tensor D^0_{ijkl}, a total of 81 coefficients as a function of the wall-normal coordinate. All the data are shown in Section 3.1.1. Out of 81 components, 41 are non-zeros and 40 are inevitably zero due to the symmetry in spanwise direction.

Out of all the elements, the largest eddy viscosity component is D^0_{1111}, with a maximum value of 1.318, and the smallest nonzero eddy viscosity component is D^0_{2331} with the maximum value of 0.00248. After comparing these values to a maximum value of the nominal eddy viscosity D^0_{2121}, which is 0.0767, we determined that the largest coefficient in the eddy viscosity tensor is one order of magnitude larger than the nominal eddy viscosity and three orders of magnitude larger than the smallest coefficient, indicating a significant anisotropy. When we examine these ratios locally at each x_2, the differences are more drastic and may go up to a few orders of magnitude. After D^0_{1111}, the largest eddy viscosity components are D^0_{1212} and D^0_{1313} with maximum values of 0.573 and 0.407, respectively. All three eddy viscosities have their first and third index represented by the streamwise direction. These indices respectively represent the component of the velocity field that mixes momentum and the direction of the mean-momentum gradient. This observation coincides with the fact that u'_1 is the largest fluctuating velocity component in channel flow. Combining the two observations, we conclude that u'_1 is the strongest mixer of momentum and is most effective in mixing in the x_1 direction, as intuitively expected. Specifically, mixing rate in the streamwise direction due to streamwise gradients is substantially faster than the standard eddy viscosity which characterises mixing in the wall-normal direction due to wall normal gradients.

Additionally, all three dominant eddy viscosity components have repeated second and fourth indices. These indices respectively represent the momentum component that is being mixed and the momentum component whose mean gradient is responsible for mixing. Based on this observation, we conclude that within D^0_{1j1l}, mean gradient of component l most effectively contributes to the generation of $\overline{u'_1 v'_j}$ when $j = l$. In other words, gradient of each momentum component most effectively generates fluxes of the same momentum component at least in the leading-order limit. This latter observation is extendable to D^0_{ijil} components.

As we discussed since flow structures and thus momentum mixing is similar between the channel flow and the attached boundary layers, we can use the measured eddy viscosity anisotropy in the former setting to identify important eddy viscosity components for the latter setting. To this end, we present in Appendix C a scaling analysis of various gradients contributing to the Reynolds stress tensor. Combining this analysis with the measured order of magnitude of each eddy viscosity component that acts as a pre-factor multiplying components of the velocity gradient tensor, we identify the key eddy viscosity components that contribute dominantly to the Reynolds stress tensor budget. Based on our analysis we identify D_{1111}, D_{1121}, D_{2121}, and D_{2221} as the key four, out of 16, dominant eddy viscosity components for 2D spatially developing turbulent boundary layers.

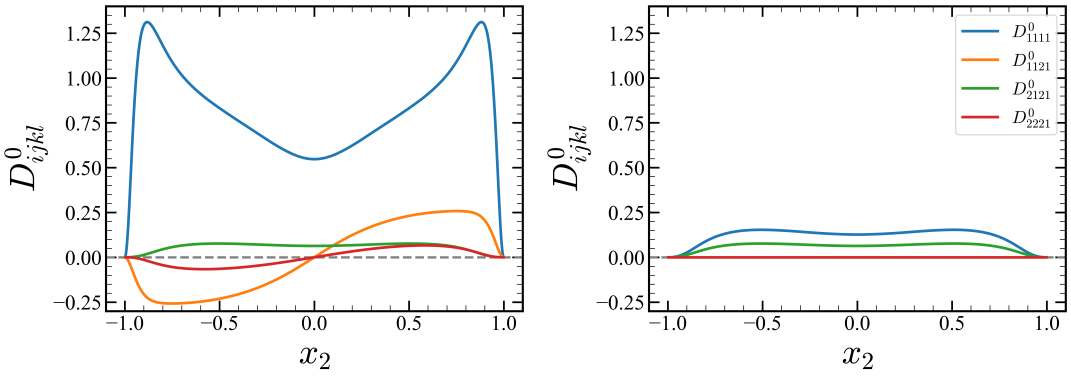

(a) MFM (b) Boussinesq

Figure 3.13: Comparison of the eddy viscosity elements D^0_{1111} (blue line), D^0_{1121} (orange line), D^0_{2121} (green line), and D^0_{2221} (red line) to the Boussinesq approximation.

Motivated by this example, we next examine the identified anisotropy against the Bousinesq approximation. When we cast the Boussinesq approximation to our tensorial representation, the components in the eddy viscosity tensor are in ratio of 0, 1, or 2 to the standard eddy viscosity ν_T. For instance, the four elements are prescribed with following ratios; $D_{1111} = 2\nu_T$, $D_{1121} = 0$, $D_{2121} = \nu_T$, and $D_{2221} = 0$. Figure 3.13 shows the comparison of these eddy viscosity components to the Boussinesq approximation. In Figure 3.13(a), we show the measured four elements using our MFM calculation. In Figure 3.13(b) we set the standard eddy viscosity to the MFM-measured leading-order value, $\nu_T = D^0_{2121}$ and prescribe the other components with the ratio to ν_T. As shown in the figure, a huge anisotropy is observed not only among all elements but specificallty among these four critical elements, and the ratio of these plots can locally go up to hundreds. We conclude that, while D_{2121} is the most important eddy viscosity component for parallel and semi-parallel flows, the presence of small non-parallel effects could lead to significant influence of anisotropy in momentum transport in wall bounded flows.

Lastly, we point that there have been attempts to include the anisotropy in RANS such as Spalart-Allmaras model with quadratic constitutive relation (SA-QCR) [60, 35, 52]. However, examining our results suggest that these models do not captured the level of the anisotropy that MFM measured. For instance, SA-QCR still prescribes $D_{1111} = 2\nu_T$ and the anisotropy is not yet introduced in needed directions.

3.1.4 Dependence on the Rate of Rotation

One of the major explicit assumptions in the Boussinesq approximation is that the Reynolds stress is dependent only on the rate of strain S_{ij} and not on the rate of rotation ω_{ij}. With our eddy viscosity tensor notation, this indicates that $D^0_{ijkl} = D^0_{ijlk}$ because under this condition, each Reynolds stress

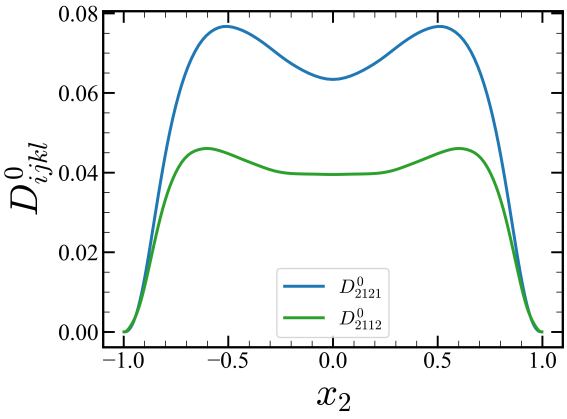

Figure 3.14: Comparison of D^0_{2121} (blue line) and D^0_{2112} (green line).

component, $\overline{u'_i u'_j}$, would be equally sensitive to both $\partial U_l/\partial x_k$ and $\partial U_k/\partial x_l$, and thus is a function of the summation $\partial U_l/\partial x_k + \partial U_k/\partial x_l$, which is $2S_{kl}$. One can verify that under this condition the inner product $D^0_{ijkl}\omega_{lk}$ would be identically zero. because the inner product of the anti-symmetric tensor, the rate of rotation, to the symmetric tensor is zero. However, our measurement of the leading-order eddy viscosity tensor invalidates the relation. Figure 3.14 shows the comparison between D^0_{2121} and D^0_{2112}. These two components have the same sign and their qualitative shape is similar, but the magnitudes are drastically different. In order for the Boussinesq assumption to be true, the two values must be identical. This highlight an important conclusion: the mean rotation can cause significant Reynolds stress even at the leading-order. Likewise, we reach the same conclusion with the case of D^0_{ij13} and D^0_{ij23}.

3.1.5 Leading-order Reynolds Stress

In Section 3.1.2, we computed a RANS solution using D^0_{2121} and compare the solution to that of the DNS to assess appropriateness of the leading-order eddy viscosity for prediction of the mean velocity profile. Another way to make this assessment is to reconstruct Reynolds stress using the computed eddy viscosity tensor and compare it to the Reynolds stress of DNS. This way, we can assess some other components in D^0_{ijkl}. The Reynolds stress in the channel flow can be represented in the following way: $\overline{u'_i u'_j} = -D^0_{ij21}\partial U_1/\partial x_2$. With the leading-order eddy viscosity tensor D^0_{ij21} computed using MFM and with the mean velocity gradient $\partial U_1/\partial x_2$ measured from the DNS data, we construct the Reynolds stress $\overline{u'_i u'_j}$.

Figure 3.15 shows the five reconstructed Reynolds stresses associated with the RANS prediction of the channel flow, in comparison with the Reynolds stresses from the DNS data. There are three important observations with the Reynolds stresses that are reconstructed with the leading-order

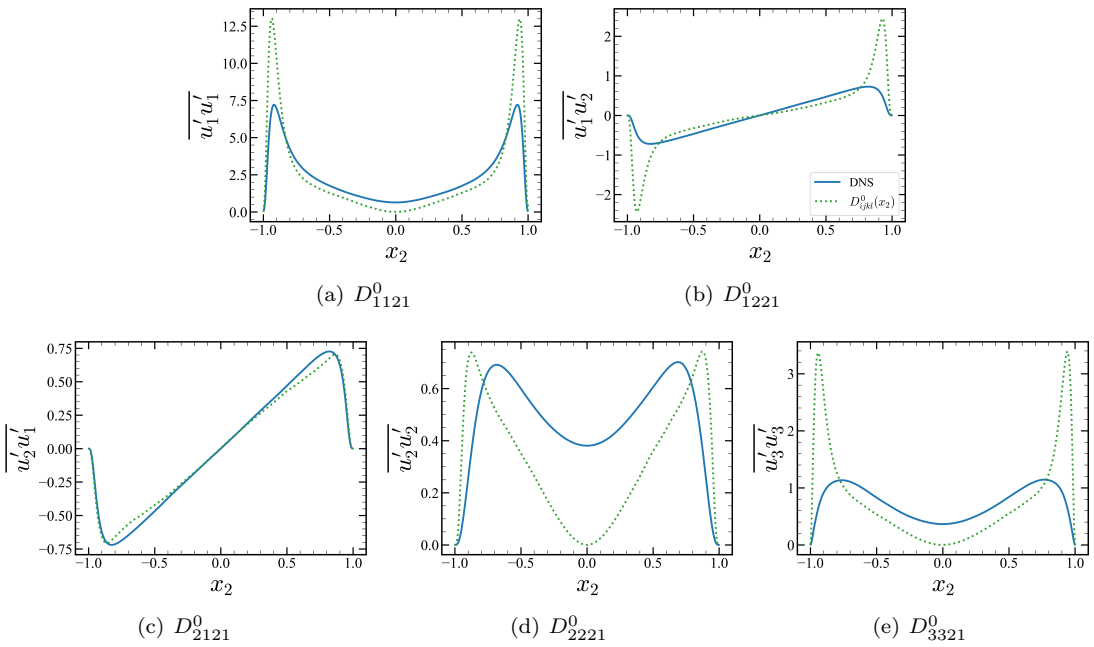

(a) D^0_{1121} (b) D^0_{1221}

(c) D^0_{2121} (d) D^0_{2221} (e) D^0_{3321}

Figure 3.15: Reynolds stresses constructed by the leading-order eddy viscosity tensor associated with (a) D^0_{1121}, (b) D^0_{1221}, (c) D^0_{2121}, (d) D^0_{2221}, and (e) D^0_{3321}: green dashed line, the reconstructed Reynolds stress by the leading-order eddy viscosity tensor; blue solid line, the DNS data.

eddy viscosity tensor. The first finding is that while the Reynolds stresses reconstructed using the leading-order eddy viscosity show similar qualitative trends and orders of magnitudes to those from DNS, there's still a noticeable difference between the two. This difference is likely due to the leading-order truncation of the eddy viscosity operator. Among the various Reynolds stresses, only $\overline{u_2'u_1'}$ is accurately constructed. This suggests that this specific component is influenced by local mean gradients, while the other components show nonlocal dependence at least in a portion of the domain.

The next important observation is that constructed Reynolds stresses from the leading-order eddy viscosity are not symmetric. This asymmetry error is entirely due to the truncated representation of the eddy viscosity to its local term, i.e. the leading term in Equation 2.13. As we shall see, inclusion of the full nonlocal eddy viscosity will eliminate this error. However, the fact that the leading-order $\overline{u_2'u_1'}$ match the DNS, substantially better than $\overline{u_1'u_2'}$ indicates that the former Reynolds stress is more local while the latter has substantial nonlocal sensitivity to the mean velocity gradient. While we do not have an intuitive explanation for this observation, we note the coincidence that the former Reynolds stress, represents flux of an active mean momentum component in the direction where its gradients are active. The only way that the latter Reynolds stress could be generated in this setting is through pressure coupling, whose fluctuations are known to nonlocally depend on velocity fluctuations.

Lastly, we observe that is that the leading-order model cannot approximate the nonzero centerline

value, where the velocity gradient is zero due to the symmetry of the channel flow. But, since the trace part of the Reynolds stress at the centerline is nonzero, the nonlocality needs to be included in eddy viscosity to enable prediction of the centerline value. In Section 3.1.6, we examine the eddy viscosity and the Reynolds stress further by including the nonlocality.

3.1.6 Positive Definiteness

It is noted that the Reynolds stress is a positive semi-definite tensor [15, 54]. Therefore, we often require a turbulence model to satisfy the same condition as done in the Boussinesq approximation with $\nu_T \geq 0$ [64]. In this section, we discuss whether this condition holds for our leading-order eddy viscosity tensor D^0_{ijkl} as well. The positive definiteness of the eddy viscosity is closely related to the mean kinetic energy equation, which is the following:

$$\frac{\partial}{\partial t}\left(\frac{U_i U_i}{2}\right) + U_j \frac{\partial}{\partial x_j}\left(\frac{U_i U_i}{2}\right) = \frac{\partial}{\partial x_j}\left(-\frac{P}{\rho}U_j\right) + \nu \frac{\partial^2 U_i U_i/2}{\partial x_j \partial x_j} \tag{3.1}$$

$$- \nu \frac{\partial U_i}{\partial x_j}\frac{\partial U_i}{\partial x_j} - \frac{\partial}{\partial x_j}\left(U_i \overline{u'_j u'_i}\right) + \overline{u'_j u'_i}\frac{\partial U_i}{\partial x_j}. \tag{3.2}$$

The last term in Equation 3.2 is the negative of turbulent kinetic energy production. It is well-known that this term drains the kinetic energy from the mean flow via interactions of the mean shear and the turbulent fluctuations, and provide energy to the turbulence production. We denote the turbulent kinetic energy as $P_k = -\overline{u'_j u'_i}\frac{\partial U_i}{\partial x_j}$. In all statistically stationary flows, the volumetric integral of P_k must be non-negative. There are certain cases such as the separation of the shear layer where P_k is locally negative, but even for those cases, the turbulent production is positive for the most of the domain [11]. The volumetric integral condition for P_k can be expressed using our generalized eddy viscosity expression in Equation 2.6.

$$\int P_k \, \mathrm{d}^3\mathbf{x} = \int -\overline{u'_j u'_i} \left.\frac{\partial U_i}{\partial x_j}\right|_{\mathbf{x}} \mathrm{d}^3\mathbf{x} \tag{3.3}$$

$$= \int\int D_{ijkl}(\mathbf{x},\mathbf{y}) \left.\frac{\partial U_l}{\partial x_k}\right|_{\mathbf{y}} \left.\frac{\partial U_i}{\partial x_j}\right|_{\mathbf{x}} \mathrm{d}^3\mathbf{y} \, \mathrm{d}^3\mathbf{x} \tag{3.4}$$

Furthermore, this condition is also required for well-posedness and numerical robustness of the simulation. Similar work has been done by Milani in the context of the scalar transport [37].

We can further reduce the Equation 3.4 using our leading-order eddy viscosity tensor as the closure model, then the production term becomes:

$$\int P_k \, \mathrm{d}^3\mathbf{x} \simeq \int D^0_{ijkl}(\mathbf{x}) \left.\frac{\partial U_l}{\partial x_k}\right|_{\mathbf{x}} \left.\frac{\partial U_i}{\partial x_j}\right|_{\mathbf{x}} \mathrm{d}^3\mathbf{x} \tag{3.5}$$

Since the operator is now local, this implies that positive definiteness must be satisfied for each

point. Then, $D^0_{ijkl}\frac{\partial U_j}{\partial x_i}\frac{\partial U_l}{\partial x_k} \geq 0$ must also be satisfied. In other word, the quadratic form of the eddy viscosity tensor is non-negative. Therefore, we can conclude that anisotropic eddy viscosity tensor is positive semi-definite.

Using our MFM measurement of the eddy viscosity, we can examine whether a local model from the truncated Kramer-Moyal expansion satisfies the positive semi-definite condition. If the positive semi-definite condition is not satisfied, it is an indication that the local truncation is not valid and nonlocality is needed for the positive definiteness condition.

To test the positive semi-definiteness of the eddy viscosity tensor, we flatten the eddy viscosity tensor and the velocity gradient. Then, the turbulent production becomes $D^0_{ijkl}\frac{\partial U_j}{\partial x_i}\frac{\partial U_l}{\partial x_k} = \mathbf{z}^T\mathbf{D}\mathbf{z}$ where $\mathbf{z}$ is the flattened velocity gradient $[\partial U_1/\partial x_1\ \partial U_2/\partial x_1\ \partial U_1/\partial x_2\ \partial U_2/\partial x_2]^T$ and where $\mathbf{D}$ is the following matrix:

$$\mathbf{D} = \begin{bmatrix} D^0_{1111} & D^0_{1112} & D^0_{1121} & D^0_{1122} \\ D^0_{1211} & D^0_{1212} & D^0_{1221} & D^0_{1222} \\ D^0_{2111} & D^0_{2112} & D^0_{2121} & D^0_{2122} \\ D^0_{2211} & D^0_{2212} & D^0_{2221} & D^0_{2222} \end{bmatrix}$$

It is well known that a symmetric $\mathbf{D}$ is positive semi-definite if and only if $\mathbf{z}^T\mathbf{D}\mathbf{z} \geq 0$ for all real vector $\mathbf{z}$. However, for our case, $\mathbf{D}$ is non-symmetric and $\mathbf{z}$ is limited to only certain value due to the incompressible condition. Therefore, we modified the quantity of interest. First of all, instead of the non-symmetric matrix $\mathbf{D}$, we look at the positive definiteness of $\mathbf{D} + \mathbf{D}^T$. If $\mathbf{D} + \mathbf{D}^T$ is positive semi-definite, $\mathbf{z}^T\mathbf{D}\mathbf{z} \geq 0$ also holds [37]. Secondly, since the flow system is incompressible, $\mathbf{z}$ is limited to certain values satisfying $\partial U_2/\partial x_2 = -\partial U_1/\partial x_1$. To expand the column vector multiplied to matrix $\mathbf{D}$ to every nonzero real column vector, we must embed the incompressibility condition to the matrix $\mathbf{D}$. We define $\mathbf{z} = \mathbf{C}\mathbf{z}^*$ where $\mathbf{z}^*$ is the reduced flattened velocity gradient $[\partial U_1/\partial x_1\ \partial U_2/\partial x_1\ \partial U_1/\partial x_2]^T$ and $\mathbf{C}$ is the following matrix:

$$\mathbf{C} = \begin{bmatrix} 1 & 0 & 0 \\ 0 & 1 & 0 \\ 0 & 0 & 1 \\ -1 & 0 & 0 \end{bmatrix}$$

Using this definition, $\mathbf{z}^T\mathbf{D}\mathbf{z}$ becomes $\mathbf{z}^{*T}\mathbf{C}^T\mathbf{D}\mathbf{C}\mathbf{z}^*$. Combining these two methods, we conclude that the eddy viscosity tensor is positive semi-definite when all the eigenvalues of the matrix $\mathbf{C}\left(\mathbf{D} + \mathbf{D}^T\right)\mathbf{C}^T$ is non-negative. We computed the smallest eigenvalue of this matrix at each x_2. The resulting plot is shown in Figure 3.16. As shown, except for the thin zones near the wall, we see that the eigenvalues are positive, hence the eddy viscosity tensor is positive definite. Near the wall,

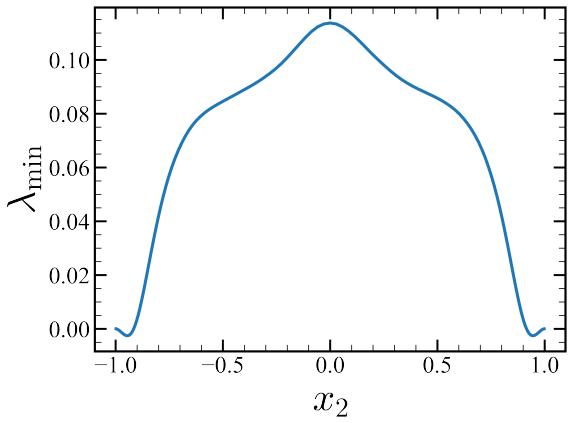

Figure 3.16: The minimum eigenvalue of the matrix $\mathbf{C}\left(\mathbf{D}+\mathbf{D}^T\right)\mathbf{C}^T$.

however, the eigenvalues become negative, indicating that the leading term is not sufficient to capture the positive semi-definiteness of the eddy viscosity. In other words, this negativity occurs due to the local truncation of the eddy viscosity tensor and therefore nonlocality should be incorporated to make the eddy viscosity positive semi-definite.

3.2 Nonlocality Analysis

In Section 3.3, we discuss that the capturing of the Reynolds stress in the channel centerline requires the inclusion of nonlocal terms in the eddy viscosity operator. To further understand the non-Boussinesq effect, we investigate eddy viscosity kernel D_{ijkl} and assess the nonlocality of the eddy viscosity. Furthermore, we discuss Reynolds stress reconstruction and positive definiteness of the full kernel.

3.2.1 Nonlocality

Figure 3.17 shows the full eddy viscosity kernel representation of the D_{2121} component. Each point in Figure 3.17(a) represents the effect of the velocity gradient at the location y_2 to the Reynolds stress at the location x_2. The distribution of D_{2121} is quite narrow and confined to $x_2 \sim y_2$, indicating the locality of this eddy viscosity. At a given location x_2, we can visualize how much contribution the remote velocity gradient at different location y_2 makes to the Reynolds stress at the location x_2.

For instance, in Figure 3.17(b), the thick blue line represents $D_{2121}\left(x_2 = 0.502, y_2\right)$ and the distribution indicates the effects of the velocity gradient nearby. If the Boussinesq approximation holds, a delta function around $y_2 = 0.502$ is expected. In the figure, even though the plotted profile is not identical to a Dirac delta function, $D_{2121}\left(x_2 = 0.502, y_2\right)$ shows concentrated behavior around

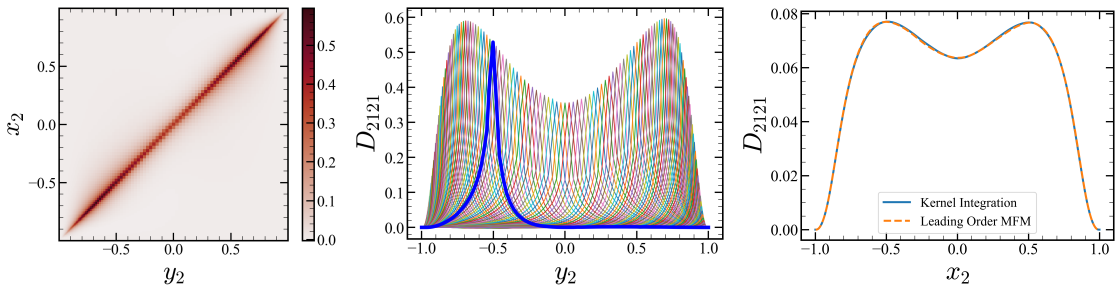

(a) D_{2121} (b) D_{2121} (c) $\int D_{2121}\mathrm{d}y_2$

Figure 3.17: Distribution of D_{2121}: (a) contour plot of D_{2121}, (b) $D_{2121}\,(x_2 = x_2^*, y_2)$ with various x_2^* where the blue line is at $x_2^* = 0.502$, and (c) the blue solid line, $\int D_{2121}\mathrm{d}y_2$ and the orange dashed line, D^0_{2121}.

$y_2 = 0.502$. The rest of the plots in Figure 3.17(b) shows $D_{2121}\,(x_2 = x_2^*, y_2)$ at other x_2^*. Overall, our narrow banded results indicate that D_{2121} is highly local throughout the domain, with small deviation to the Boussinesq approximation. Such locality explains the earlier conclusion in Section 3 that a leading-order eddy viscosity is reasonable for this parallel flow.

In addition, Figure 3.17(c) is comparing the results of kernel integration $\int D_{2121}\mathrm{d}y_2$ and the leading-order eddy viscosity tensor component D^0_{2121}. The definition of D^0_{2121} is the leading-order moment of the eddy viscosity kernel D_{2121}. In other word, the integration of the kernel $\int D_{2121}\mathrm{d}y_2$ must match the eddy viscosity tensor D^0_{2121}. Figure 3.17(c) shows that the two results are collapsing verifying that our two different MFM measurements, MFM for D^0_{ijkl} and MFM for D_{2121} show consistent result.

Previously, we demonstrated that the leading-order eddy viscosity alone can predict a highly accurate RANS solution for the channel mean velocity with the prediction error around 1%. This error can be furture reduced by including the nonlocality using the full kernel representation of the eddy viscosity. Figure 3.18 shows the two RANS results, one obtained using the leading-order eddy viscosity D^0_{2121} and the other obtained using eddy viscosity kernel D_{2121}. Analytically, the full measurement of the kernel is expected to provide the RANS solution that is identical to the averaged DNS result. In our simulation, small errors are due to statistical noise that we expect to resolve with a larger data set. Still, the kernel result is significantly better than the leading-order result, indicating that even the RANS simulation of the channel, which is highly local, can be improved using a nonlocal model.

Next, we assess nonlocality of other components of D_{ijkl} by examining the corresponding kernels. For example, the eddy viscosity kernel D_{1221} (Figure 3.19) is widespread and shows significant nonlocality, invalidating the intrinsic assumption in the Boussinesq approximation. The level of nonlocality is drastic such that the velocity gradient at one half of the channel may affect the Reynolds

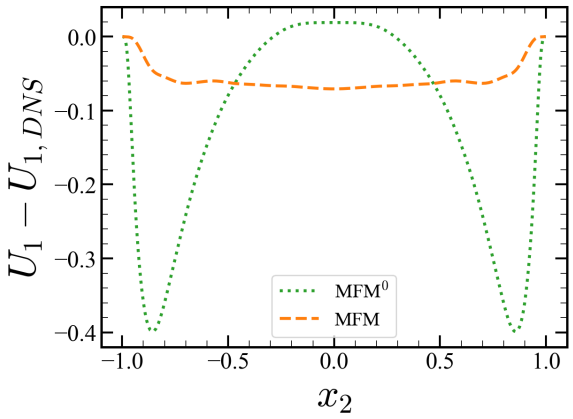

Figure 3.18: Error in RANS prediction of the streamwise velocity using eddy viscosity tensor D^0_{2121} (denoted as MFM^0) and eddy viscosity kernel D_{2121} (denoted as MFM), $U_1 - U_{1,\mathrm{DNS}}$; the dashed green line, U_1 predicted with D^0_{2121} and the dashed orange line, U_1 predicted with D_{2121}.

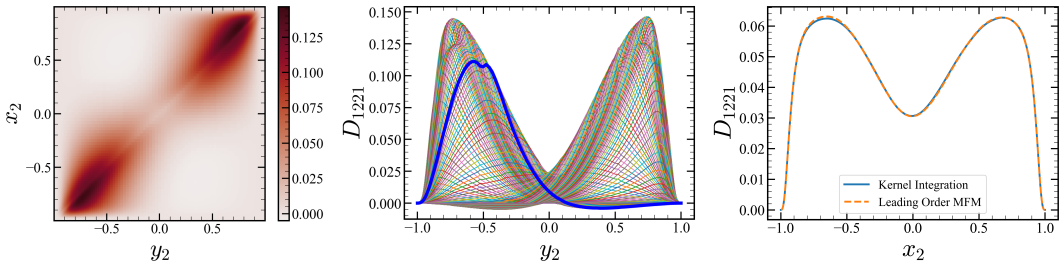

(a) D_{1221} (b) D_{1221} (c) $\int D_{1221}\mathrm{d}y_2$

Figure 3.19: Distribution of D_{1221}: (a) contour plot of D_{1221}, (b) $D_{1221}\,(x_2 = x_2^*, y_2)$ with various x_2^* where the blue line is at $x_2^* = 0.502$, and (c) blue solid line, $\int D_{1221}\mathrm{d}y_2$ and orange dashed line, D^0_{1221}.

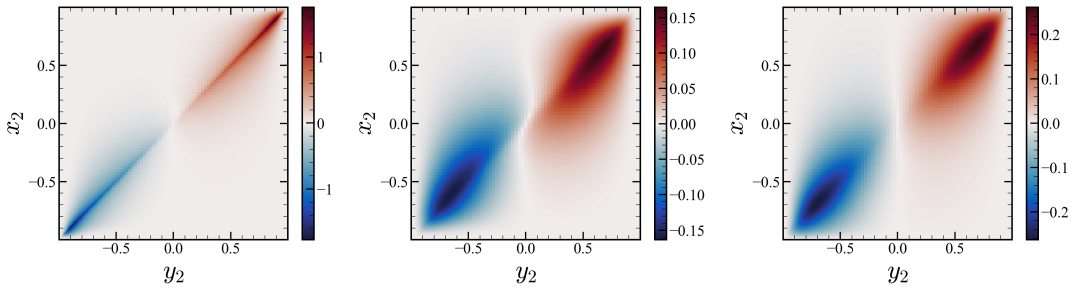

(a) D_{1121} (b) D_{2221} (c) D_{3321}

Figure 3.20: Distribution of nonzero D_{ij21} where (a) D_{1121}, (b) D_{2221}, and (c) D_{3321}.

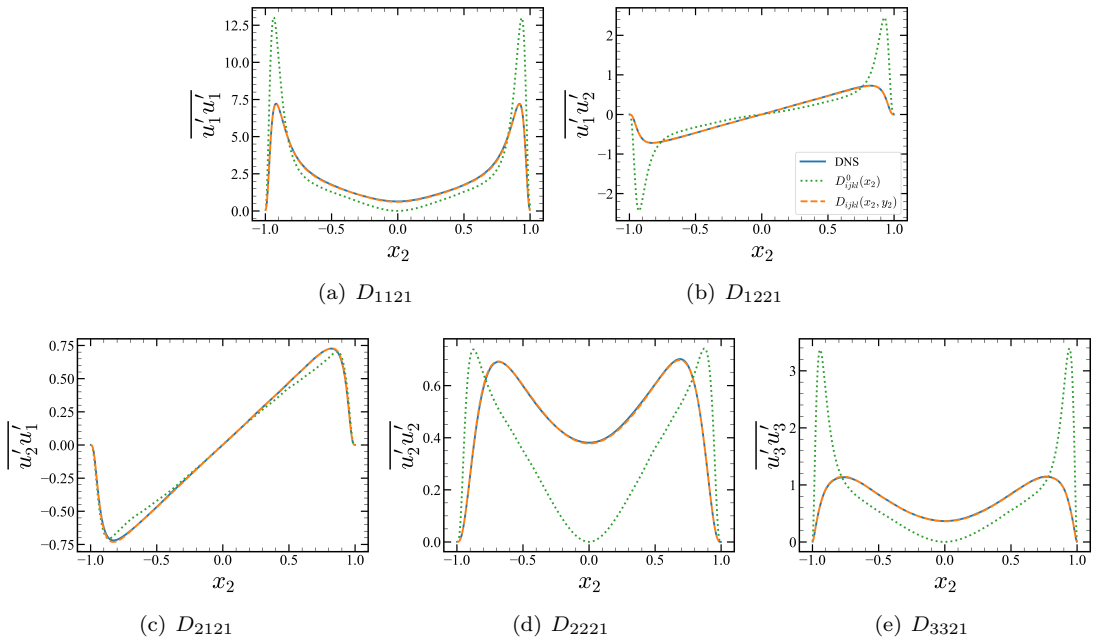

(a) D_{1121} (b) D_{1221}

(c) D_{2121} (d) D_{2221} (e) D_{3321}

Figure 3.21: Reynolds stresses constructed by the leading-order eddy viscosity tensor and the eddy viscosity kernel associated with (a) D_{1121}, (b) D_{1221}, (c) D_{2121}, (d) D_{2221}, and (e) D_{3321}: orange dashed line, the reconstructed Reynolds stress by the eddy viscosity kernel; green dashed line, the reconstructed Reynolds stress by the leading-order eddy viscosity tensor; blue solid line, the DNS data.

stress at the other half of the domain. Moreover, the shape of D_{2121} differs from D_{1221}, implying the non-universality of the kernel profile across different components of eddy diffusivity. Furthermore, the differences in the kernel shape between D_{2121} and D_{1221}, clarifies why a truncated eddy viscosity operator based on the leading term of its Kramer-Moyal expansion can lead to asymmetric Reynolds stresses. Figure 3.20 shows the additional three nonzero eddy viscosity kernel D_{1121}, D_{2221}, and D_{3321}. The rest of the components are zero due to channel symmetry. These three kernels correspond to the trace part of the eddy viscosity kernel and are also highly nonlocal.

3.2.2 Revisit of Reynolds stress

Lastly, we revisit the Reynolds stress reconstruction with the inclusion the effects of the nonlocality. Figure 3.21 shows three different ways of constructing the Reynolds stresses. The first shown in the orange dashed line is the reconstructed Reynolds stress by the eddy viscosity kernel from MFM and the mean velocity gradient from DNS. The second shown in green dashed line is the reconstructed Reynolds stress by the leading-order eddy viscosity tensor from MFM and the mean velocity gradient from DNS. The last one is from the mean DNS data shown in blue solid line. The leading-order

result and the mean DNS data are shown before in Figure 3.15.

Unlike the leading-order analysis, the results from the full kernel eddy viscosity matches very well to the DNS data. These plots verify our computational method yielding two findings. First, with full kernels, the Reynolds stresses recover the symmetry that was lost in the leading-order approximation. Only D_{2121}, which is quite narrow banded, is applicable for the local approximation. Hence, this leads to the symmetry breakage after leading-order approximation. Second, now we can capture the nonzero Reynolds stress at the channel centerline. Thus, the measured nonlocal eddy viscosity allows prediction of non-zero Reynolds stresses near the centerline, whereas the leading-order approximation fails to do so.

3.2.3 Revisit of Positive Definiteness

In Section 3.1.6, we discuss the positive definiteness of the local eddy viscosity tensor D^0_{ijkl}. Due to the leading-order truncation of the eddy viscosity kernel, D_{ijkl}, our result indicated that the local eddy viscosity tensor was not positive definite near the walls. In this section, we introduce the full kernel and see if including the nonlocality restores the semi-positive definite condition.

Using the full eddy viscosity kernel expression and applying the fact that there exist only one nonzero velocity gradient in the turbulent channel flow, the turbulent production in Equation 3.4 can be written as the following:

$$P_k = \int D_{2121}(x_2, y_2) \left.\frac{\partial U_1}{\partial x_2}\right|_{y_2} \mathrm{d}y_2 \frac{\partial U_1}{\partial x_2} = \left[\frac{\partial U_1}{\partial x_2}\right]^T [D_{2121}] \left[\frac{\partial U_1}{\partial x_2}\right].$$

The far right term represents the discrete form of the expression, where $\left[\frac{\partial U_1}{\partial x_2}\right]$ represents any velocity gradient vector at each point in x_2 and $[D_{2121}]$ represents the discrete matrix value of $D_{2121}(x_2, y_2)$. To make the turbulent production non-negative, the matrix $[D_{2121}]$ needs to be semi-positive definite. Likewise in Section 4.5, we computed eigenvalues of $[D_{2121}]+[D_{2121}]^T$ to determine the positive definiteness. The computed eigenvalues range from 0.00 to 7.58, indicating that the eddy viscosity kernel D_{2121} is indeed semi-positive definite, recovering the stability condition that was lost by the leading-order truncation.

Chapter 4

Eddy Viscosity in a Turbulent Separated Boundary Layer

Materials in this chapter have been published in [41].

This chapter discuss the eddy viscosity for SBL at Re_θ=350 using the MFM. This work presents the leading-order term in the Kramers-Moyal expansion representing the local-limit of the eddy viscosity operator, focusing on the anisotropy. We measure a subset of components of the eddy viscosity tensor using MFM simulations, which are D^0_{ij11}, D^0_{ij12}, D^0_{ij13}, D^0_{ij21}, D^0_{ij22}, and D^0_{ij23}, where $i, j \in \{1, 2, 3\}$. We discuss the anisotropy by focusing on D^0_{1111} and D^0_{2121}, and further discuss the upper limit of the local models.

4.1 Leading-order Eddy Viscosity Tensor

This section provides the entire nonzero values of the leading-order eddy viscosity tensor D^0_{ijkl}. Figure 4.1 shows a subset of measured eddy viscosity components in contour plot and Figure 4.2-4.13 shows all the measured eddy viscosity components in line plot before ($x_1 = 0$) and after the separation ($x_1 = 100$). The separation location is at $x_1 = 103$. This corresponds to the eddy viscosity tensor in Equation 2.17. The values that are not shown converge to zero, which was either evident through the spanwise homogeneity of SBL or through a decrease in statistical noise as the simulation was run for longer.

4.2 Standard Eddy Viscosity

In the turbulent boundary layer region where $\partial U_1/\partial x_2$ is the only dominant component of the mean velocity gradient and $\overline{u_2' u_1'}$ is the most important component of the Reynolds stress tensor, D^0_{2121}

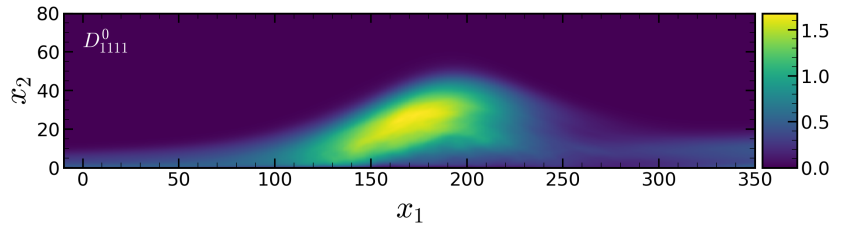

(a) D^0_{1111}

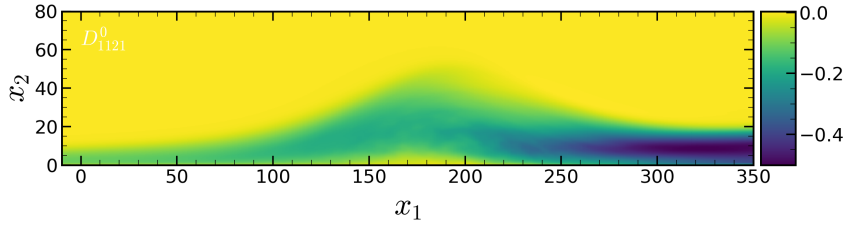

(b) D^0_{1121}

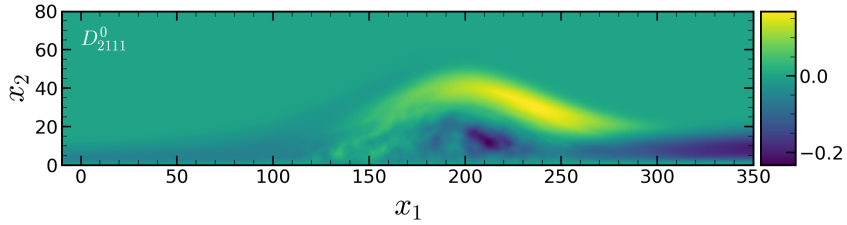

(c) D^0_{2111}

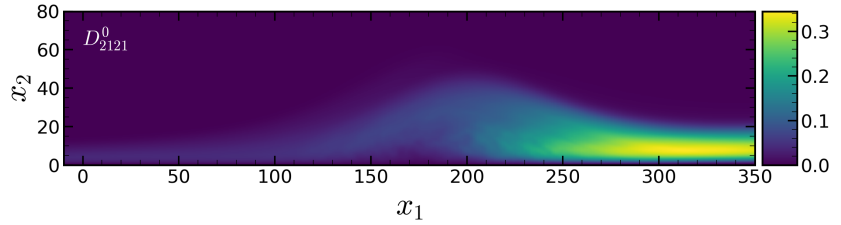

(d) D^0_{2121}

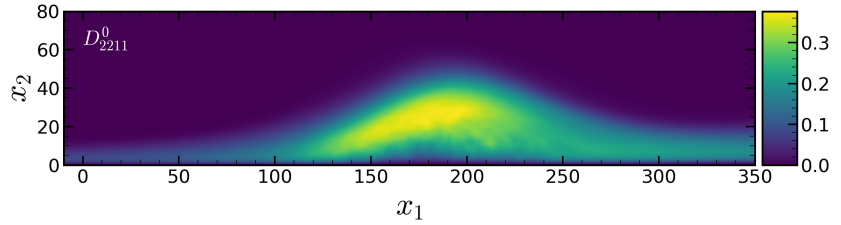

(e) D^0_{2211}

Figure 4.1: Distribution of nonzero D^0_{ijkl} for SBL.

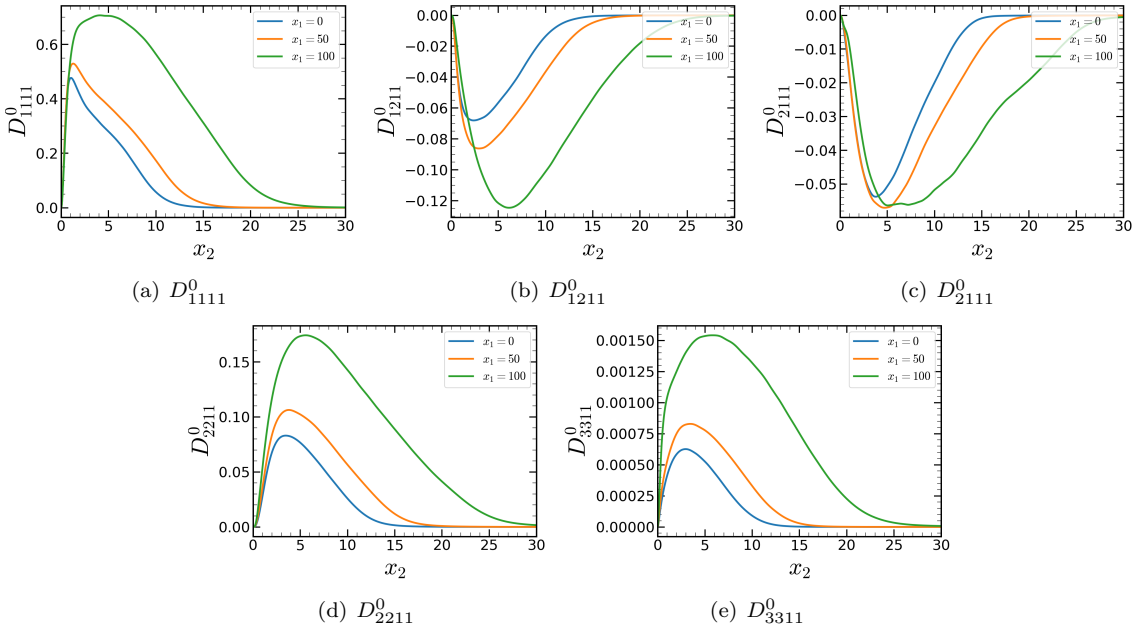

(a) D^0_{1111} (b) D^0_{1211} (c) D^0_{2111}

(d) D^0_{2211} (e) D^0_{3311}

Figure 4.2: Distribution of nonzero D^0_{ij11} for SBL before separation.

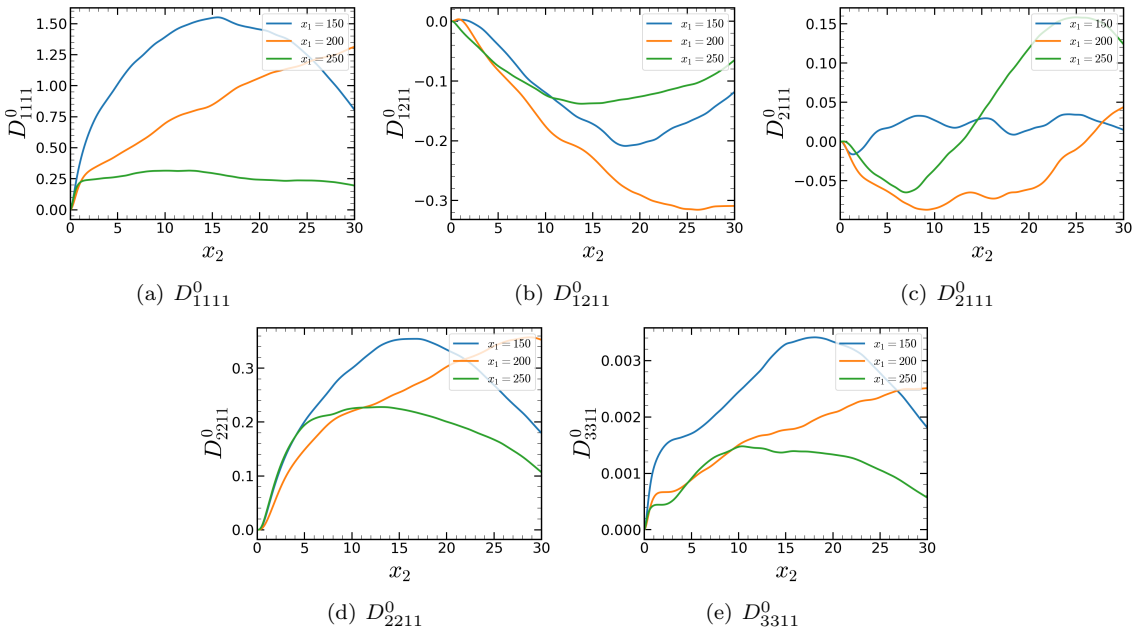

(a) D^0_{1111} (b) D^0_{1211} (c) D^0_{2111}

(d) D^0_{2211} (e) D^0_{3311}

Figure 4.3: Distribution of nonzero D^0_{ij11} for SBL after separation.

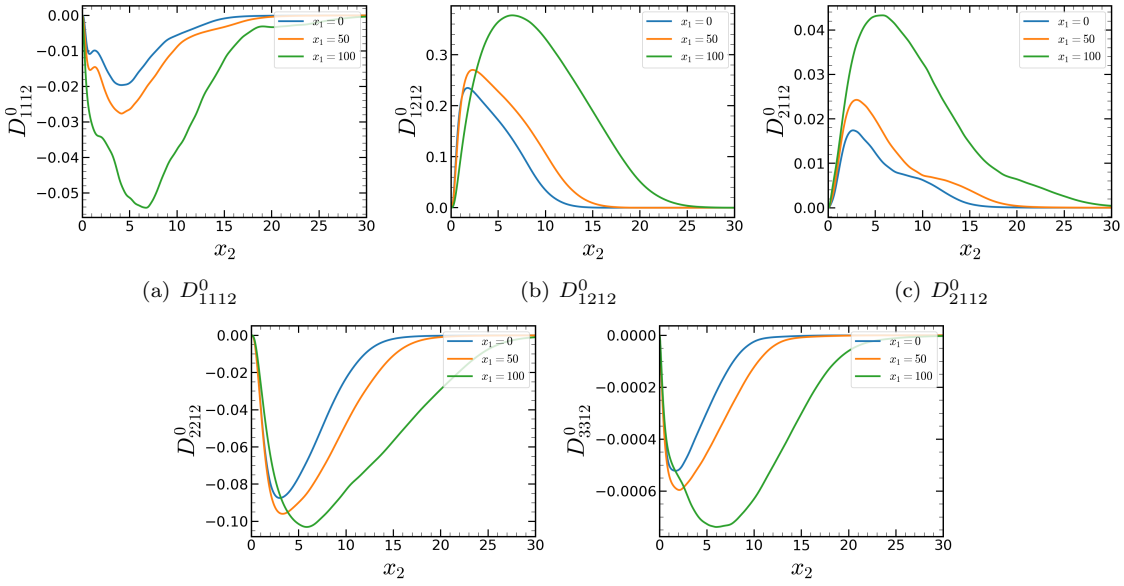

(a) D^0_{1112} (b) D^0_{1212} (c) D^0_{2112}

(d) D^0_{2212} (e) D^0_{3312}

Figure 4.4: Distribution of nonzero D^0_{ij12} for SBL before separation.

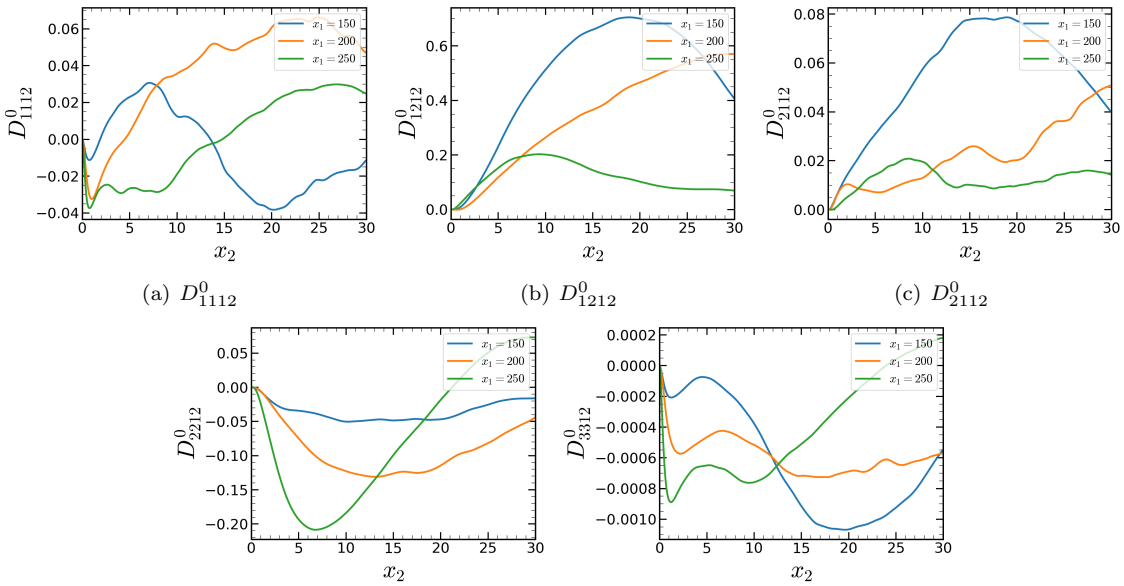

(a) D^0_{1112} (b) D^0_{1212} (c) D^0_{2112}

(d) D^0_{2212} (e) D^0_{3312}

Figure 4.5: Distribution of nonzero D^0_{ij12} for SBL after separation.

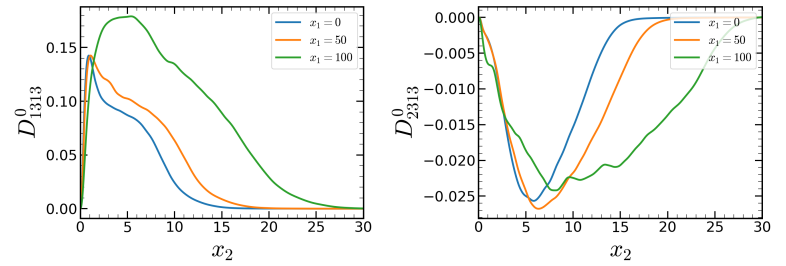

(a) D^0_{1313} (b) D^0_{2313}

(c) D^0_{3113} (d) D^0_{3213}

Figure 4.6: Distribution of nonzero D^0_{ij13} for SBL before separation.

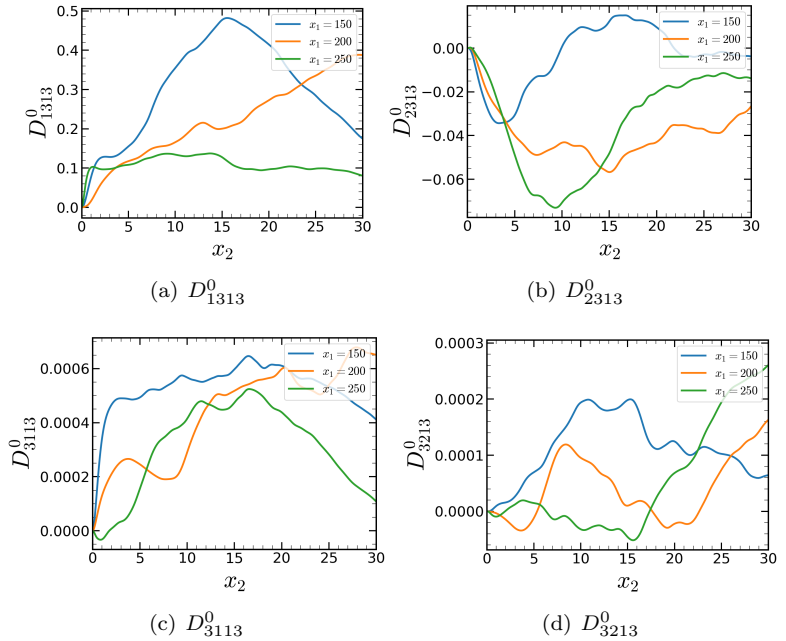

(a) D^0_{1313} (b) D^0_{2313}

(c) D^0_{3113} (d) D^0_{3213}

Figure 4.7: Distribution of nonzero D^0_{ij13} for SBL after separation.

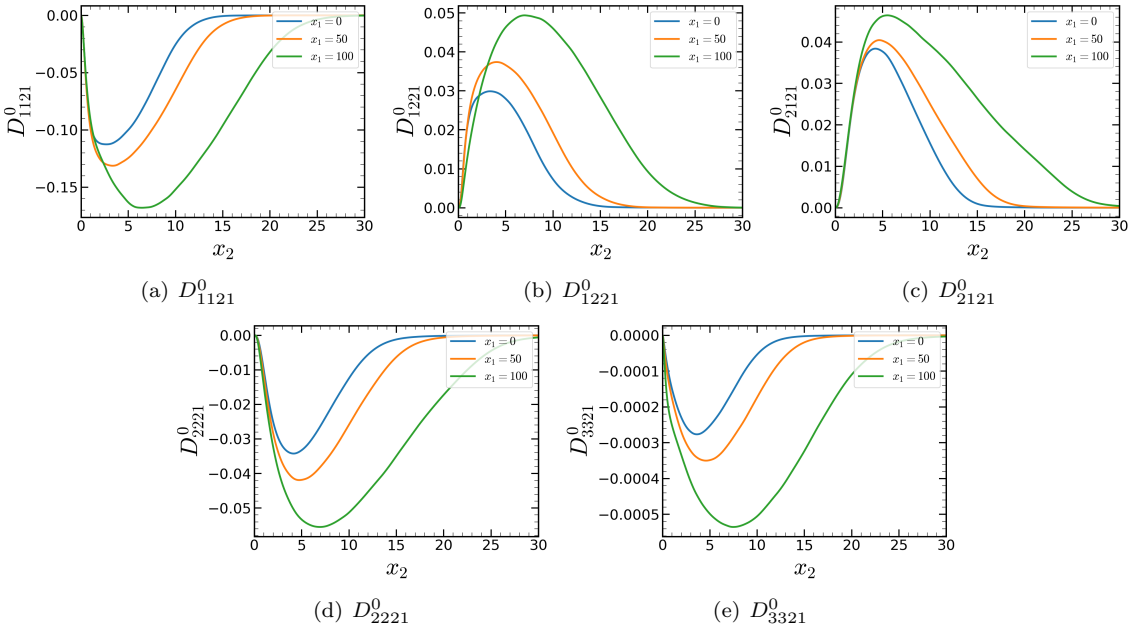

(a) D^0_{1121} (b) D^0_{1221} (c) D^0_{2121}

(d) D^0_{2221} (e) D^0_{3321}

Figure 4.8: Distribution of nonzero D^0_{ij21} for SBL before separation.

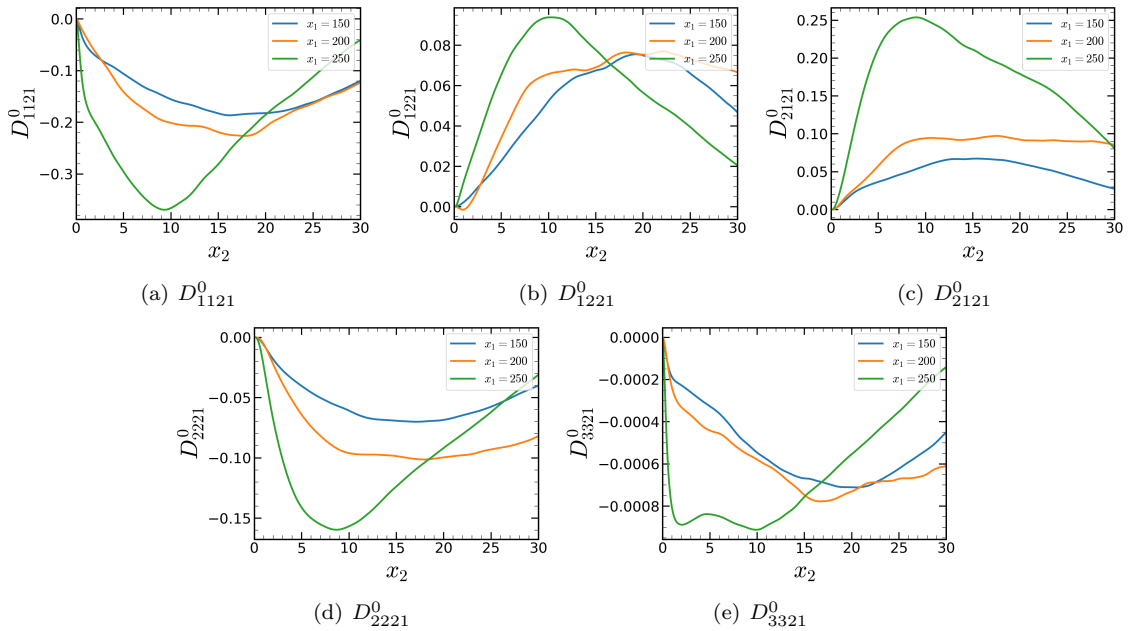

(a) D^0_{1121} (b) D^0_{1221} (c) D^0_{2121}

(d) D^0_{2221} (e) D^0_{3321}

Figure 4.9: Distribution of nonzero D^0_{ij21} for SBL after separation.

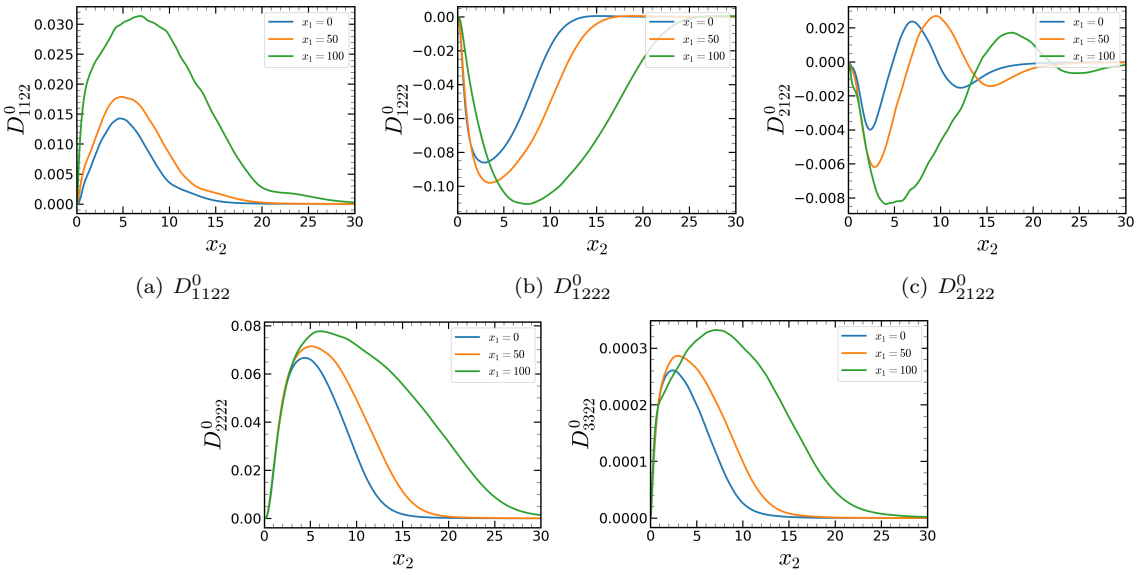

(a) D^0_{1122} (b) D^0_{1222} (c) D^0_{2122}

(d) D^0_{2222} (e) D^0_{3322}

Figure 4.10: Distribution of nonzero D^0_{ij22} for SBL before separation.

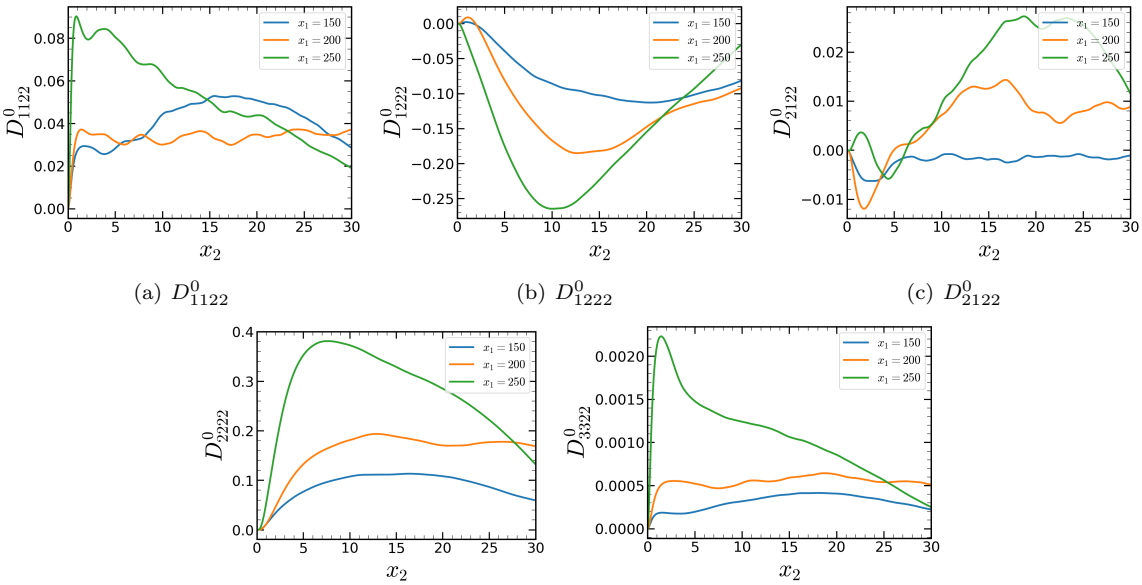

(a) D^0_{1122} (b) D^0_{1222} (c) D^0_{2122}

(d) D^0_{2222} (e) D^0_{3322}

Figure 4.11: Distribution of nonzero D^0_{ij22} for SBL after separation.

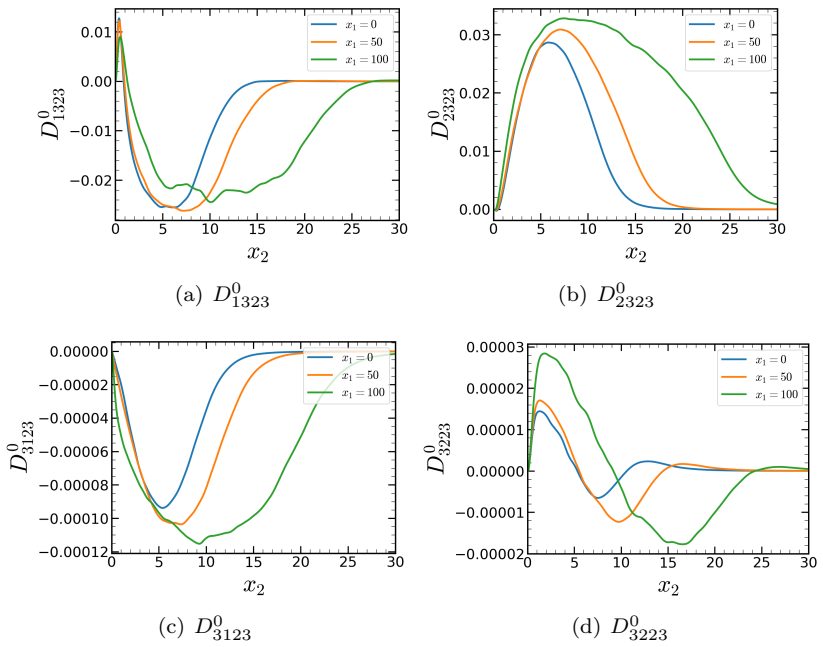

(a) D^0_{1323} (b) D^0_{2323}

(c) D^0_{3123} (d) D^0_{3223}

Figure 4.12: Distribution of nonzero D^0_{ij23} for SBL before separation.

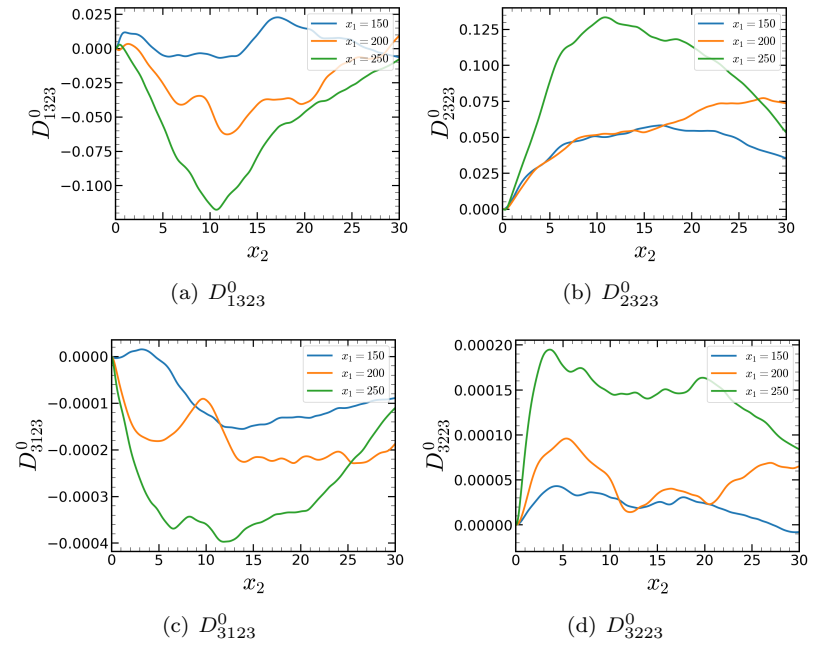

(a) D^0_{1323} (b) D^0_{2323}

(c) D^0_{3123} (d) D^0_{3223}

Figure 4.13: Distribution of nonzero D^0_{ij23} for SBL after separation.

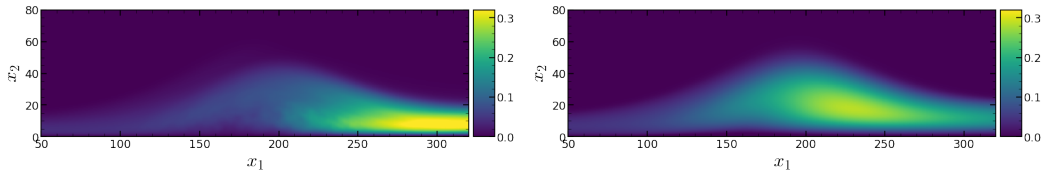

(a) D^0_{2121} (b) ν_T

Figure 4.14: MFM measurement of SBL: (a) D^0_{2121} of the anisotropic eddy viscosity tensor and (b) ν_T from SA model.

is solely the key component of the eddy viscosity tensor. However, when the flow starts to deviate from this semi-parallel behavior, we expect the other components of the velocity gradient tensor and Reynolds stress tensor to play a significant role, and therefore other components of the eddy viscosity tensor D^0_{ijkl} become important. Therefore, in order to truly assess RANS closures in the context of the separated flow, assessment of all tensorial elements in D^0_{ijkl} is necessary.

Using MFM, we measure all D^0_{ijkl} where $i, j, k, l \in \{1, 2\}$. These are the eddy viscosity components that are needed for RANS closure of the separated boundary layer with or without sweep in our settings. While we provide all components of the eddy viscosity data for both canonical settings as a supplementary document to this report, in this section, we show two of the components which are D^0_{1111} and D^0_{2121} in order to highlight the anisotropy in D^0_{2121} for the SBL flow. These are the two most important components of the eddy viscosity tensor in the sense that they have the most influence on the mean momentum budget. While D^0_{2121} is the most important eddy viscosity component in semi-parallel flows, D^0_{1111} is found to play an important role near the separation bubble. Also, we compare the measured eddy viscosity to that of a widely-used isotropic RANS model, Spalart-Allmaras (SA) [61]. The SA model is chosen as an example of a local, and isotropic eddy viscosity model. We expect however, that our comparative results hold qualitatively for any other RANS model with a Boussinesq approximation closure.

An isotropic eddy viscosity, as implied by the Boussinesq model used in SA, implies $D^0_{1111} = D^0_{2222} = 2\nu_T$, $D^0_{1212} = D^0_{1221} = D^0_{2121} = D^0_{2121} = \nu_T$ and the rest of D^0_{ijkl} components are zero where $i, j, k, l \in \{1, 2\}$. We compare the measured D^0_{ijkl} to the corresponding Boussinesq eddy viscosity.

Figure 4.14 shows the comparison between D^0_{2121} and ν_T. The component D^0_{2121} is the eddy viscosity tensor element that is multiplied with $\partial U_1/\partial x_2$ to compose $\overline{u'_2 u'_1}$, which is the only Reynolds stress needed to conduct RANS of parallel flows. Initially, in the regions where the turbulent boundary layer is attached before the the suction and blowing boundary condition is in effect, D^0_{2121} and ν_T are in good agreement. This is expected, because SA is well-tuned to capture attached boundary layers. Given the semi-parallel nature of the attached regions, even an isotropic eddy viscosity model is expected to perform well as long as it is well-tuned to match a realistic D^0_{2121}. Other components of the eddy viscosity tensor play an unimportant secondary role in the attached flow region. This finding is consistent with the results of [42] where appropriateness of both local and

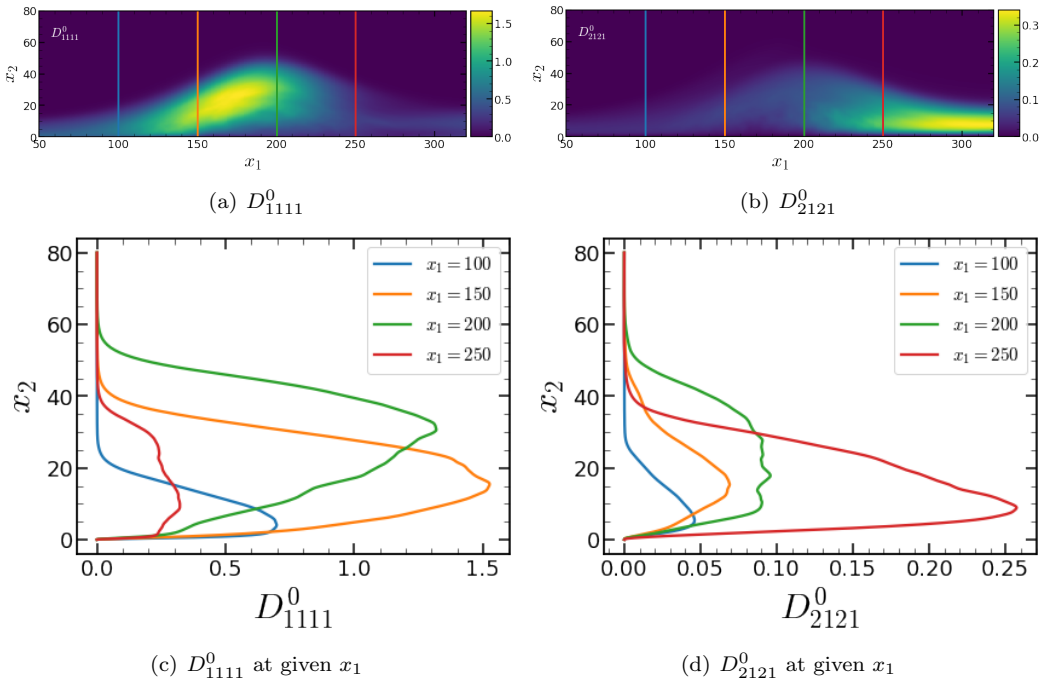

(a) D^0_{1111} (b) D^0_{2121}

(c) D^0_{1111} at given x_1 (d) D^0_{2121} at given x_1

Figure 4.15: MFM measurements of two anisotropic eddy viscosity tensor components for SBL and their values at the various x_1 locations, (a) and (c) D^0_{1111}, and (b) and (d) D^0_{2121}.

isotropic models for parallel flows are quantitatively assessed and confirmed through investigation of a turbulent channel flow.

In the separated flow region, however, D^0_{2121} implied by SA exhibits some deviation from the measured eddy viscosity using MFM. The magnitude of D^0_{2121} and ν_T are of the same order but the overall spatial distribution varies significantly. We observe that the measured D^0_{2121} reaches its maximum value after the reattachment zone whereas ν_T reaches its maximum value around the end of the bubble. These differences indicate that this Boussinesq eddy viscosity do not capture the corresponding local eddy viscosity tensor component correctly.

4.3 Anisotropy of Eddy Viscosity

Close investigation of the other components of the measured eddy viscosity indicates significantly different spatial distributions among the components rendering the Boussinesq model hopeless in capturing all components simultaneously. Figure 4.15 compares two components of eddy viscosity measured by the MFM procedure D^0_{1111} and D^0_{2121}. Figure 4.15(a) and Figure 4.15(b) show the contours of these two components with the color-coded vertical lines representing locations of the eddy viscosity values in Figure 4.15(c) and Figure 4.15(d). In the Boussinesq model, D^0_{1111} is equal

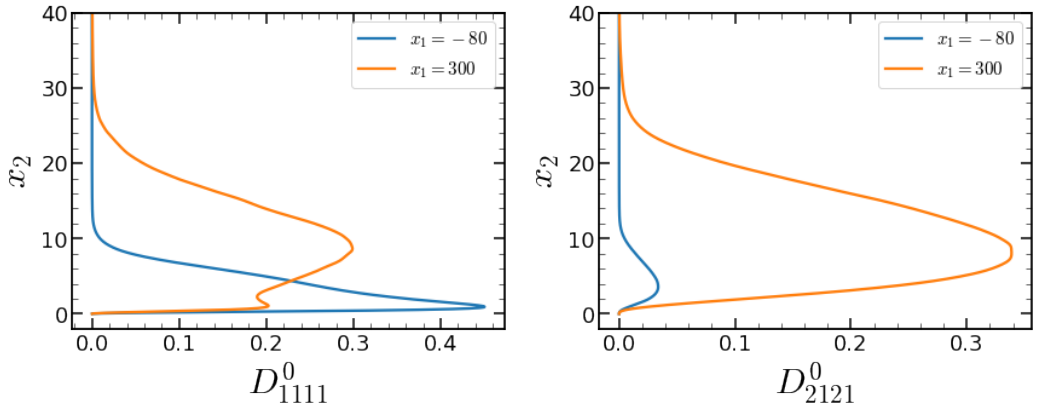

(a) D^0_{1111} at given x_1

(b) D^0_{2121} at given x_1

Figure 4.16: Two components, (a) D^0_{1111} and (b) D^0_{2121}, of the anisotropic eddy viscosity tensor measured at two different locations from SBL, $x_1 = -80$ (blue) and $x_1 = 300$ (orange), before and after the separation bubble.

to $2\nu_T$. Therefore, any model with the Boussinesq approximation presets $D^0_{1111} = 2D^0_{2121}$. However, the MFM measurements, as shown in the figure, indicate that the difference between D^0_{1111} and D^0_{2121} is much more drastic than a mere factor of two. For instance, these two fields differ by a factor of $\mathcal{O}(10)$ upstream of the bubble, but have the same order of magnitude after the reattachment. Furthermore, not only are the magnitudes of the eddy viscosity components vastly different, but so are their spatial distributions, such as the locations of their respective maxima. Similar qualitative differences are also observed in other components of the eddy viscosity tensor. Such results suggest that the eddy viscosity operator is strongly anisotropic even in the local limit.

Furthermore, we see that D^0_{ijkl} changes qualitatively even within semi-parallel attached boundary layer regions when comparing the data from before and after the separation bubble. Before and after the bubble, we expect both of the regions to have a similar nature because after the reattachment, the flow recovers to a semi-parallel boundary layer very quickly after the short transition length by forming near-wall streaks [69, 40]. In Figure 4.16, we compare D^0_{1111} and D^0_{2121} at two different locations: before separation at $x_1 = -80$ and after reattachment at $x_1 = 300$. The MFM measurements reveal that D^0_{1111} remains similar in order before and after the bubble whereas D^0_{2121} increases drastically after the flow passes the separation bubble. Given the similar profiles of the local mean velocity in the two zones, the differences in the measured eddy viscosity suggest some nonlocal effects, as if the flow after reattachment still retains the vigorous mixing from its history of being in the separated flow zone. While this statement is qualitative, we shall see below a more quantitative assessment of the need for nonlocality near the reattachment zone.

Based on the observations made so far, our measured eddy viscosity indicates that RANS models

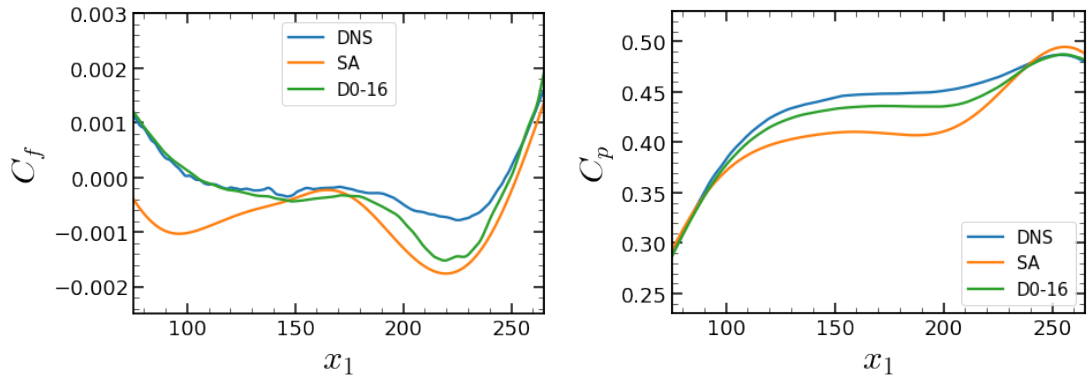

(a) Friction coefficient

(b) Pressure coefficient

Figure 4.17: The measured anisotropic but local-limit eddy viscosity offers significant improvements in RANS predictions. The friction coefficient (a) and pressure coefficient (b) are computed using DNS (blue), RANS using SA (orange), and RANS using all 16 measured eddy viscosity tensor components (green).

should at least incorporate anisotropy. However, the question remains whether relying on the local-limit eddy viscosity is sufficient for prediction of the true mean field. Although it is difficult to construct an analytical stand-alone local Reynolds-stress closure model that would reproduce the anisotropy in the measured eddy viscosity, it is possible to perform a priori testing of such models with the quantitative components of eddy viscosity already at hand.

4.4 Verification and Key Components of Anisotropic Eddy Viscosity

We calculate the solution to the RANS equation using the directly measured eddy viscosity and Equation (2.17) to represent the closure term. The adopted RANS equation in this case is written as:

$$\frac{\partial U_i}{\partial t} + \frac{\partial U_j U_i}{\partial x_j} = -\frac{\partial P}{\partial x_i} + \frac{1}{\mathrm{Re}} \frac{\partial^2 U_i}{\partial x_j \partial x_j} + \frac{\partial}{\partial x_j} D^0_{ijkl} \frac{\partial U_l}{\partial x_k} \tag{4.1}$$

$$\frac{\partial U_j}{\partial x_j} = 0 \tag{4.2}$$

Figure 4.17 shows the friction coefficient and the pressure coefficient near the separation bubble resulting from our a priori RANS solution. We denote this solution as D0-16 since we are using 16 eddy viscosity tensor components given only two components of the mean flow are active in SBL. Along with this solution, the RANS solutions obtained from averaging of DNS and from the SA model are also provided for comparison. The measured leading-order eddy viscosity is shown

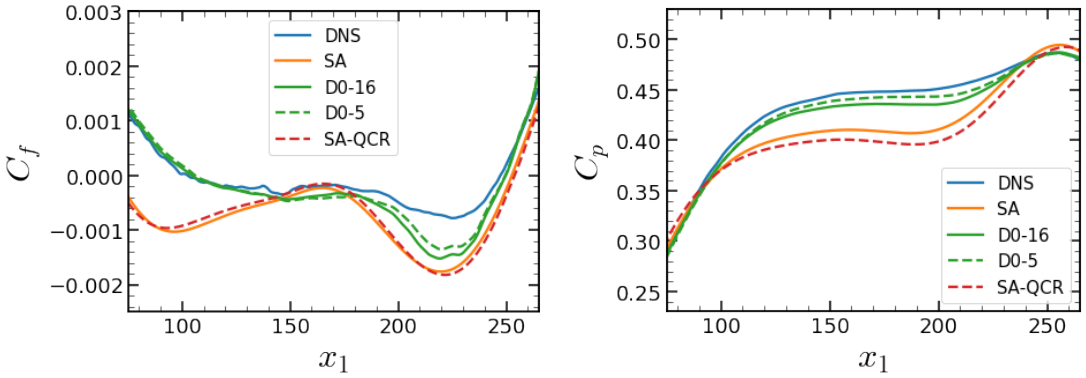

(a) Friction coefficient

(b) Pressure coefficient

Figure 4.18: A subset of components in the measured anisotropic but local-limit eddy viscosity offers significant improvements in RANS predictions. Friction coefficient (a) and pressure coefficient (b) are computed using DNS (blue), RANS using SA (orange), RANS using 16 eddy viscosity tensors components (green solid), RANS using 5 eddy viscosity tensors components D^0_{1111}, D^0_{1121}, D^0_{2111}, D^0_{2121}, and D^0_{2211} (green dashed), and SA with quadratic constitutive relation (QCR) (red dashed).

to predict results much more consistent with the mean of DNS data compared to the SA model prediction. It is important to emphasize that this improvement is obtained using the measured eddy viscosity rather than using a model. Any modeled local eddy viscosity tensor is likely to have errors in matching D^0_{ijkl}, and therefore, the present results offer an upper bound of accuracy for local Reynolds stress models.

Based on these results, it is shown that adding anisotropy to a local RANS model can significantly increase the accuracy of the model. Furthermore, we analyzed these eddy viscosity tensor components to find which of the components contribute significantly to the solution. In the previous work on MFM measurements of channel flow [42], we conducted asymptotic analysis on the spatially developing two-dimensional boundary layer to determine which of the eddy viscosity tensor components are most relevant, and we concluded that D^0_{1111}, D^0_{1121}, D^0_{2121}, and D^0_{2221} are the most important components. However, the present separated boundary layer involves a more complex flow topology not perfectly conforming to the scaling analysis inspired by a gradually developing attached boundary layer. Through additional momentum budget analysis as well as sensivitity analysis of C_f and C_p, we identified the five most important tensorial components of D^0_{ijkl} that provide a reasonable representation of the full tensor even when the rest of the components are set to zero. These five components are D^0_{1111}, D^0_{1121}, D^0_{2111}, D^0_{2121}, and D^0_{2211}.

As with the D0-16 model, we calculate the RANS solution using the reduced five components, D^0_{1111}, D^0_{1121}, D^0_{2111}, D^0_{2121}, and D^0_{2211}, and call this the D0-5 model. Figure 4.18 shows the resulting friction coefficient, C_f, and the pressure coefficient, C_p, near the separation bubble. The result indicates most of the improvement in the RANS solution can be retained with only five components.

We should note however, that the presented rule of reduction of eddy viscosity tensor to a five component tensor is not rotational invariant. In other words, this reduction rule is specific to a coordinate system aligned with the wall. We have attempted to add rotational invariance and further reduce the number of model coefficients. We formulated a rotationally invariant model using the Cayley-Hamilton theorem with inspiration from the work of Pope [46]. This model consisted of two coefficients where these coefficients were tuned using constrained least-square while matching D^0_{2121}, and maintaining a positive semidefinite constraint. However, the model did not lead to substantial improvement when compared against a tuned Boussinesq model, and hence we do not include the results in this work. We further assess other anisotropic RANS models that are rotationally invariant. SA with quadratic constitutive relation (QCR) [60] is chosen as the test case, but as shown in Figure 4.18, we observe that QCR does not offer substantial improvement in prediction of the friction and pressure coefficients compared to SA.

As mentioned, we expect the result computed using the measured D^0_{ijkl} to be the upper bound of accuracy for local Reynolds stress models. However, as shown, the solutions obtained by the full local eddy viscosity tensor (Figure 4.17) are still not identical to the DNS result. Given that we have a precise measurement of the leading-order eddy viscosity in the Kramer Moyal expansion, we conclude that the remaining gap between our solution and DNS is due to nonlocality. Based on these results, the most significant mismatch between DNS and local RANS is near the reattachment zone of the separated bubble. We therefore, conclude that nonlocality plays an important role in governing Reynolds stresses in this zone.

Lastly, as we shall discuss in the next section, modification on the eddy viscosity in the zones downstream the bubble reattachment was done to ensure numerical stability of the RANS simulations. Such modification is minimally affecting the results around the bubble due to the convective nature of the boundary layer.

4.5 Physical Constraints on the Eddy Viscosity and Numerical Robustness

For SBL, the measured D^0_{ijkl} is found to be non-positive semidefinite downstream of the separation bubble, which causes numerical robustness issues. This condition is not an issue as far as we use the measured eddy viscosity as a post-processing tool to elucidate mixing of momentum to the leading-order. However, if one attempts to use any eddy viscosity for prediction of mean flows, i.e. as used in RANS models, positive definite condition is a necessary condition for a well-posed formulation and for robust numerical solutions. To further understand this issue of the numerical robustness, we look at the physical constraints on the eddy viscosity in this section. We first discuss the physically-expected condition for the generalized eddy viscosity operator, to further elucidate implications on its local-limit representation, which has been formulated in this work as a truncated

series expansion. Consider the equation for the mean kinetic energy, $U_i^2/2$, formed by dotting the RANS equation by U_i. The Reynolds stress term dotted by U_i can be rewritten as,

$$-U_i \frac{\partial}{\partial x_j} \overline{u_i' u_j'} = -\frac{\partial}{\partial x_j}(U_i \overline{u_i' u_j'}) + \frac{\partial U_i}{\partial x_j} \overline{u_i' u_j'} \tag{4.3}$$

where the last term is a source term, which appears with opposite sign as the production term in the turbulent kinetic energy equation. In order for the flow to reach a statistically stationary state, the volume integral of the source term must be negative. In other words, when integrated over the entire domain, we expect turbulence to extract energy from the mean flow, and therefore

$$\int_V \frac{\partial U_i}{\partial x_j} \overline{u_i' u_j'} \mathrm{d}V \leq 0. \tag{4.4}$$

This is only required in the volume integral sense. Specifically, $\frac{\partial U_i}{\partial x_j} \overline{u_i' u_j'}$ can be positive locally in some regions of the separation bubble as shown by Abe [3]. Substituting the generalized eddy viscosity from Equation 2.6 results in the condition:

$$\int_V \int_V \frac{\partial U_i}{\partial x_j}(\mathbf{x}) D_{ijkl}(\mathbf{x}, \mathbf{y}) \frac{\partial U_l}{\partial x_k}(\mathbf{y}) \mathrm{d}\mathbf{y} \mathrm{d}\mathbf{x} \geq 0. \tag{4.5}$$

For an eddy viscosity operator to be physically stable, the above equation must hold for any physically admissible input velocity gradient field. This condition does not directly constrain $D_{ijkl}(\mathbf{x}, \mathbf{y})$ to be a positive semidefinite tensor for any specific input coordinate, $\mathbf{x}$ and $\mathbf{y}$. If the eddy viscosity operator is exactly local, then $D_{ijkl}(\mathbf{x}, \mathbf{y}) = D^0_{ijkl}(\mathbf{x})\delta(\mathbf{y} - \mathbf{x})$. Under this condition, Equation 4.5 would exactly reduce to:

$$\int_V \frac{\partial U_i}{\partial x_j} D^0_{ijkl} \frac{\partial U_l}{\partial x_k} dV \geq 0, \tag{4.6}$$

which again must hold for any physically admissible input velocity gradient field, noting that now $\partial U_i/\partial x_j$ and $\partial U_l/\partial x_k$ are at the same location, $\mathbf{x}$. This implies that $D^0_{ijkl}(\mathbf{x})$ must be a positive semidefinite tensor for any given $\mathbf{x}$, i.e., the symmetric part of D^0_{ijkl} must have nonnegative eigenvalues [42, 37]. Equation 4.6 must hold only when the exact eddy viscosity kernel is local. However, this condition does not imply that the leading-order eddy viscosity, D^0_{ijkl}, which is also the local term in a truncated approximation must be positive definite. In other words, the observed violation of positive definite condition in D^0_{ijkl} merely indicate that the full eddy viscosity kernel is nonlocal, and D^0_{ijkl} is not representative of an exact kernel.

Additionally, as we shall see, violation of the positive definite condition for the leading-order eddy viscosity, D^0_{ijkl}, does not necessarily coincide with zones of negative turbulence production. Local negative production can happen only when the eddy viscosity kernel involves non-negligible nonlocality; otherwise, as mentioned above, exact local eddy viscosity is positive definite ensuring positive production. With a nonlocal kernel, local negative production can be sustained when the

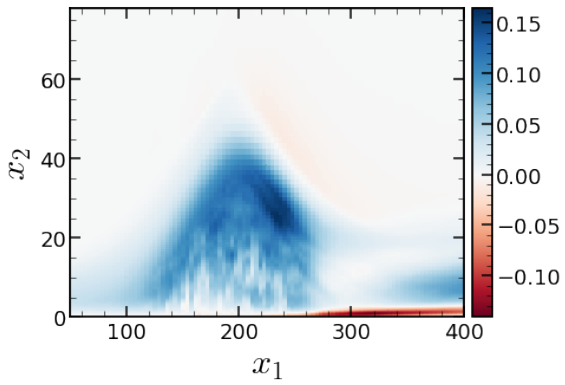

Figure 4.19: Minimum eigenvalue of the symmetric part of the eddy viscosity tensor for SBL.

local Reynolds stress is dominantly controlled by a large mean gradient at a remote location. But in calculation of the production term this Reynolds stress is being multiplied by the local velocity gradient, which itself maybe uncorrelated with the remote gradient that dominantly contributes to the Reynolds stress.

We now return our focus to zones where D^0_{ijkl} is not positive definite, by examining the sign of the minimum eigenvalue associated with the symmetric part of the measured eddy viscosity tensor [42, 37]. Figure 4.19 shows distribution of this eigenvalue in space for SBL. D^0_{ijkl} is found to be non-positive semidefinite in the region downstream of the separation bubble. Previously, we had pointed to nonlocality in the vicinity of the reattachment point, based on assessment of accuracy of the leading-order eddy viscosity using comparisons between DNS and local RANS. This criterion provides another metric that complements the previous metric for identification of nonlocal zones.

Aside from physical interpretation discussed above, a non-positive semidefinite eddy viscosity, D^0_{ijkl}, can lead to numerical instabilities and lack of robustness if used as part of RANS closure. To remedy these issues, the values of D^0_{ijkl} for SBL near wall after the bubble reattachment are modified to make D^0_{ijkl} positive semidefinite. However, this modification region is only downstream of the zones shown in Figure 4.17(a) and Figure 4.17(b). The modification is localized and only D^0_{1121} component is changed. The modification is as follows:

$$D^0_{1121} := D^0_{1121}\left(1 - 0.2\left(\tanh\left(\frac{x_1 - 293}{20}\right) + 1\right)\left(-\tanh\left(\frac{x_2 - 1}{4}\right) + 1\right)\right) \tag{4.7}$$

This modification is centered downstream of reattachment at $x_1 = 293$, while the coordinate of the reattachement point is $x_1 \sim 240$. Additionally, this modification is only used for the purpose of generating Figure 4.17(a) and Figure 4.17(b). Since this modification is primarily conducted after the bubble reattachment, we anticipate its minimal impact on the solution around the bubble due to the convective nature of the flow system. Furthermore, the reduced five-coefficient eddy viscosity tensor for SBL is similarly non-positive semidefinite in the downstream region and similarly treated.

Chapter 5

Eddy Viscosity in a Separated Boundary Layer with Sweep

Materials in this chapter have been published in [43].

In this chapter, we expand on our previous MFM research [41] to examine a more realistic separation scenario of SBLS. Our previous work focused on a unique case where the shear stress at the separation bubble was zero. However, in actual aerodynamics, the majority of the separation line experiences non-zero mean shear due to three-dimensional effects in the mean flow. To address this gap, we follow the approach of [14] and use a canonical flat plate turbulent boundary layer setup with a spanwise sweep imposed on top of the boundary. Separation is induced via suction and blowing boundary conditions, as in our prior work. The goal of this study is to investigate the sensitivity of the eddy viscosity tensor to the imposed sweep and to re-examine the role of eddy viscosity anisotropy in determining the mean momentum budget in this flow. We use MFM to quantify all relevant components of the local-limit eddy viscosity tensor. We compare the anisotropic eddy viscosity tensors between the separation bubble with and without sweep, as in our previous study [41]. Using the eddy viscosity measurement, we quantify and understand the sweep effect.

5.1 Anisotropy Induced from Sweep Effect

In what follows, we first quantitatively demonstrate the anisotropy of the eddy viscosity tensor for the considered swept separation bubble. In this section, we measure a subset of components of the eddy viscosity tensor using MFM simulations, which are D^0_{ij11}, D^0_{ij12}, D^0_{ij13}, D^0_{ij21}, D^0_{ij22}, and D^0_{ij23}, where $i, j \in \{1, 2, 3\}$. We discuss the anisotropic effect from the added sweep.

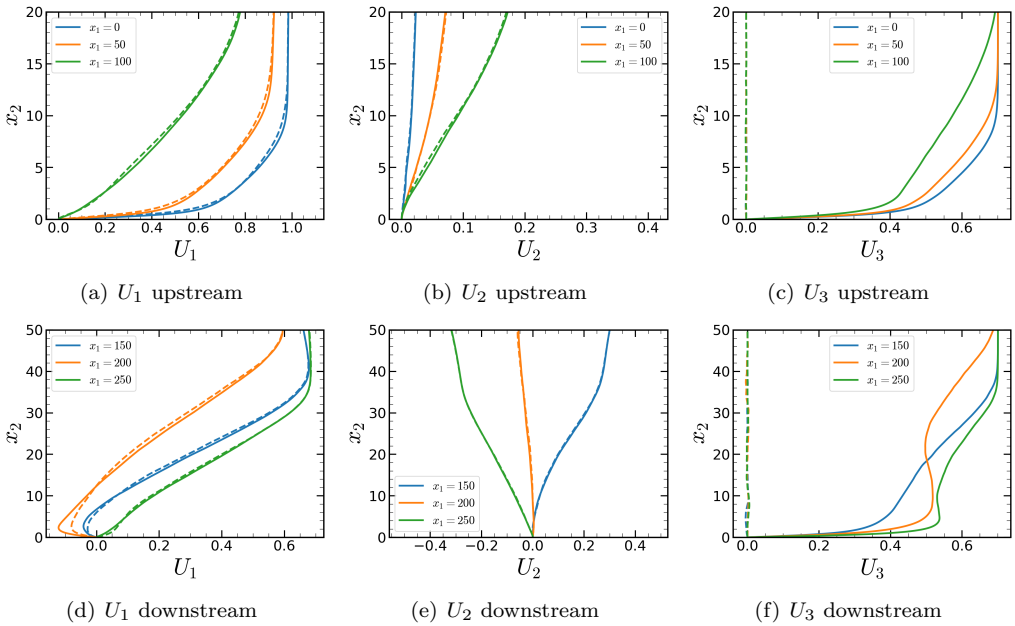

(a) U_1 upstream (b) U_2 upstream (c) U_3 upstream

(d) U_1 downstream (e) U_2 downstream (f) U_3 downstream

Figure 5.1: Velocity profile U_i for SBL (dashed) and SBLS (solid).

5.1.1 Sweep Effect in DNS

Following Coleman et al. [14], we conducted DNS and MFM simulations of the separation bubble at a 35° sweep. Previously, we explained how the SBLS simulations were altered to align the chordwise component with that of the SBL. The x_1 direction represents the chordwise direction, while the flow direction that is tilted 35° is referred to as the streamwise direction. Figure 5.1 depicts the velocity profiles of SBL (dashed) and SBLS (solid) for U_1, U_2, and U_3. Six different x_1 locations were chosen to display the variation in velocity profile as the distance from the wall increases. Figures (a)-(c) illustrate the DNS results upstream of the separation, while (d)-(e) depict the results following the separation, while the separation point is at $x_1 = 108$. We observed that U_1 and U_2 were nearly identical between SBL and SBLS. Although there were some discrepancies in the areas close to the wall after the separation, this is evident since SBL and SBLS are two different flow system. However, as demonstrated by the Reynolds number chordwise variation in Figure 2.13(b), the SBLS flow was generated effectively to match U_1, U_2, and Re_θ. This approach enables us to isolate the effect of sweep while matching as much as possible the chordwise and wall-normal components of the flow.

Coleman et al. [14] compared unswept and swept flow and its projection of the flow onto the chordwise-wall-normal plane in which the gradient act identical. By doing so they examined the independence principle (IP) for treatment of swept wing boundary layers according to which the in-plane motion must be independent of the spanwise momentum in this two dimensional-three component flow. While the IP is valid for laminar and inviscid flows, it is not valid for turbulent

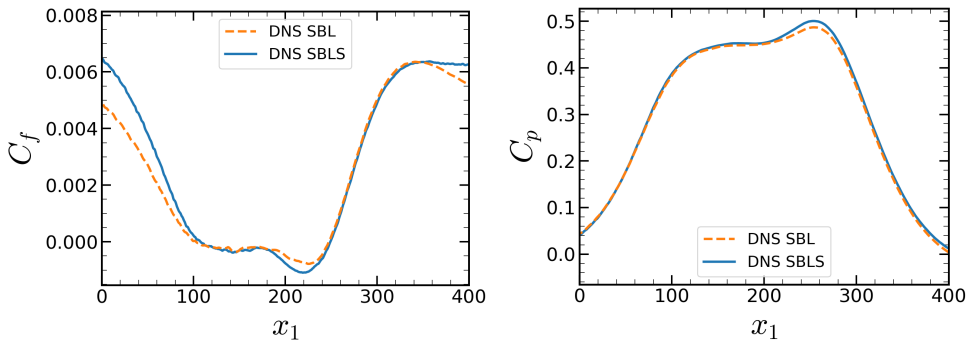

(a) Friction coefficient

(b) Pressure coefficient

Figure 5.2: Friction coefficient and pressure coefficient for SBL (dashed) and SBLS (solid).

boundary layers, as evidenced by changes in near-wall behavior. In the case of turbulent flow, the IP requires that the chordwise and vertical components remain unaffected by the sweep effects [14]. This is clearly not the case since presence of the sweep has resulted in measurable changes in the chordwise and wall-normal motions as shown in Figure 2.11.

In the work of Coleman et al., the main takeaway was that the IP is not valid for the upstream zone where the turbulent boundary layer (TBL) is attached and it is valid for the downstream zone where the flow is near the separation. To verify this, two locations were used: one at $x_1 = 0$ which is well into the attached zone, and the other at $x_1 = 100$ which is near the separation. In Coleman et al. [14], the validity of IP was assessed by comparing the chordwise projected friction coefficient. We have recreated the same analysis using new simulation results shown in Figure 5.2. This figure shows the friction coefficient and the pressure coefficient along the wall. Consistent with Coleman et al.'s [14] conclusions regarding IP, the figure shows that the friction coefficient is significantly affected by the sweep at $x_1 = 0$, while at $x_1 = 100$, near the separation zone, the friction coefficient curves match. This effect is also shown in Figure 2.11 where the log-law change to incorporate the sweep effect. Von Karman constant becomes $k_x = k/\sqrt{\cos\alpha}$, indicating a larger mixing effect due to the sweep leads to an increased Von Karman constant.

Next, we will reevaluate the conclusions by Coleman et al.[14], by examining momentum mixing in the context of MFM. However, before proceeding, we examine the Reynolds stress that is computed from DNS. Figure 5.3 is a contour plot of the Reynolds stress $\overline{u_2' u_1'}$ for SBL and SBLS. Qualitatively, they appear quite similar. On the other hand, Figure 5.4 shows a line plot of the Reynolds stress $\overline{u_2' u_1'}$ at two different locations, one at $x_1 = 0$ and the other at $x_1 = 100$. The dashed line represents the result from SBL, while the solid line represents the Reynolds stress from SBLS, and both datasets are obtained from DNS data. As we can observe at $x_1 = 0$, the swept flow increases the Reynolds stress magnitude. The increase in level is approximately 29% when comparing the two peak values. On the other hand, at $x_1 = 100$, the difference is comparable to the statistical uncertainty, and the

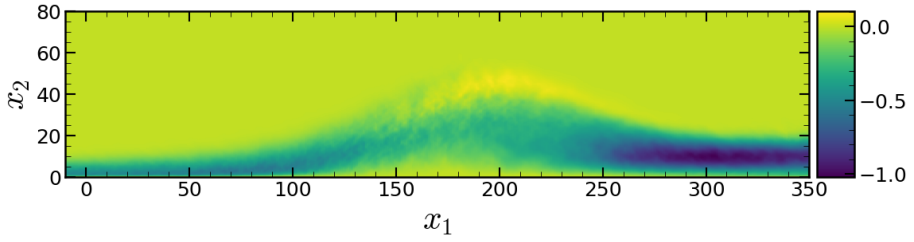

(a) SBL

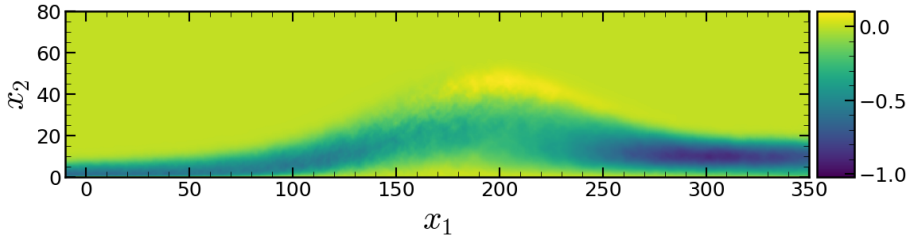

(b) SBLS

Figure 5.3: Reynolds Stress $\overline{u_2' u_1'}$ for SBL and SBLS.

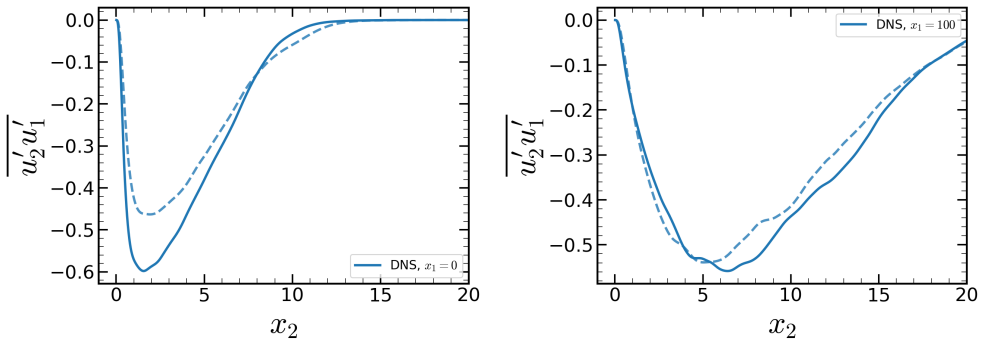

(a) $x_1 = 0$ (b) $x_1 = 100$

Figure 5.4: Reynolds Stress $\overline{u_2' u_1'}$ at given x_1 from DNS for SBL (dashed) and SBLS (solid).

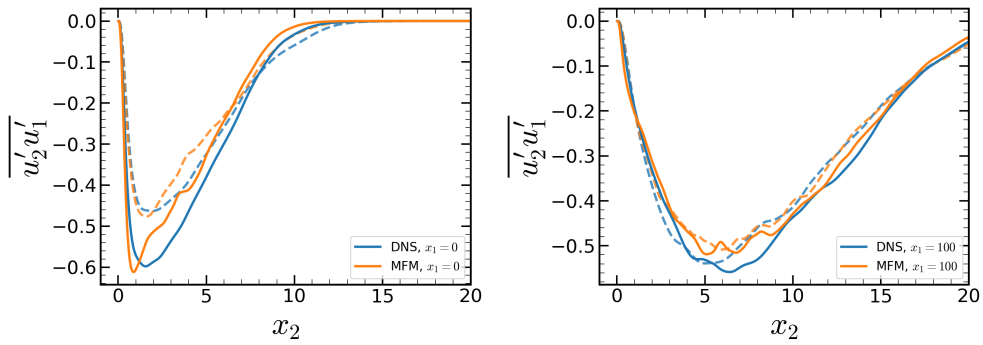

(a) $x_1 = 0$ (b) $x_1 = 100$

Figure 5.5: Reynolds Stress $\overline{u_2'u_1'}$ from DNS and MFM for SBL (dashed) and SBLS (solid).

peak ratio difference is only about 3%. This indicates that the Reynolds stress component $\overline{u_2'u_1'}$ is more affected by sweep in the turbulent boundary layer region and is barely affected by sweep near the separation, which is consistent with the conclusions of Coleman et al. [14].

5.1.2 Reynolds Stress Reconstruction using MFM Measurements

Next, we breakdown the Reynolds stress curves into contributions by different components of the eddy viscosity tensor. However, we cannot do this without first confirming that the measured leading-order eddy viscosity (local limit) can reasonably reproduce the total Reynolds stress obtained from the DNS. Figure 5.5 displays two zones of the Reynolds stress, similar to Figure 5.4, with the addition of an orange line representing the results obtained from the MFM reconstruction of the Reynolds stress: $D^0_{21kl}\,\partial U_l/\partial x_k$. In this reconstruction, we are using the velocity gradient obtained from the DNS data and the eddy viscosity obtained from MFM measurements. As shown in Figure 5.5, the peak values are highly similar between DNS and MFM, which justifies the use of the leading-order eddy viscosity obtained from our MFM for the analysis of the breakdown of Reynolds stress in terms of contributions by various components of the velocity gradient tensor. This is also compatible with our observation from SBL where nonlocality was found to be unimportant until the flow reaches near reattachment zone.

5.1.3 Leading-order Eddy Viscosity Tensor

This section provides the entire nonzero values of the leading-order eddy viscosity tensor D^0_{ijkl}. Figure 5.6 and 5.7 shows a subset of measured eddy viscosity components in contour plot and Figure 5.8 - 5.19 shows all the measured eddy viscosity components in line plot before ($x_1 = 0$) and after the separation ($x_1 = 100$). The separation location is at $x_1 = 108$. This corresponds to the eddy viscosity tensor in Equation 2.17.

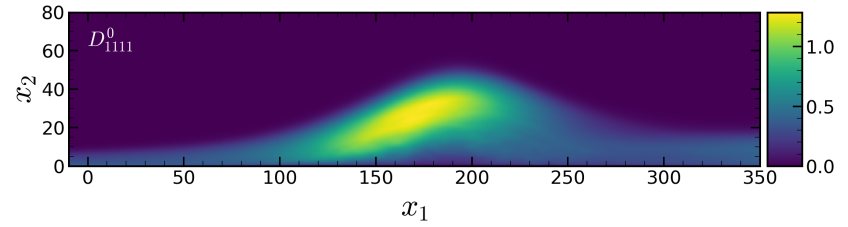

(a) D^0_{1111}

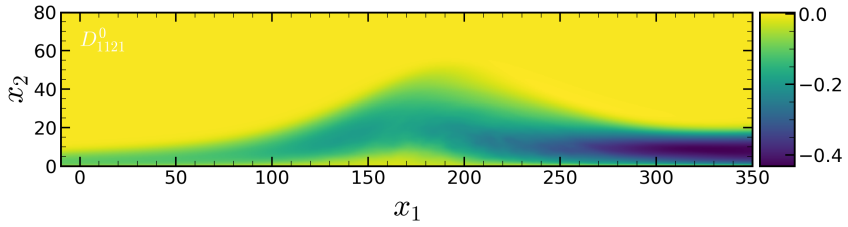

(b) D^0_{1121}

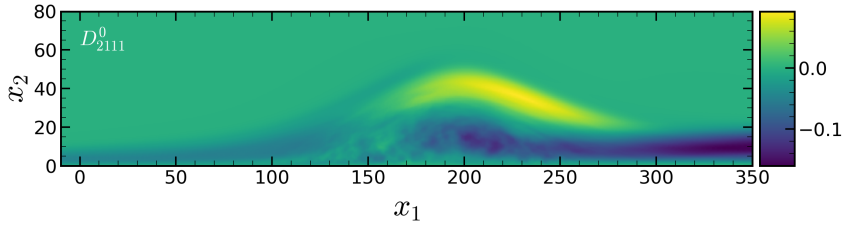

(c) D^0_{2111}

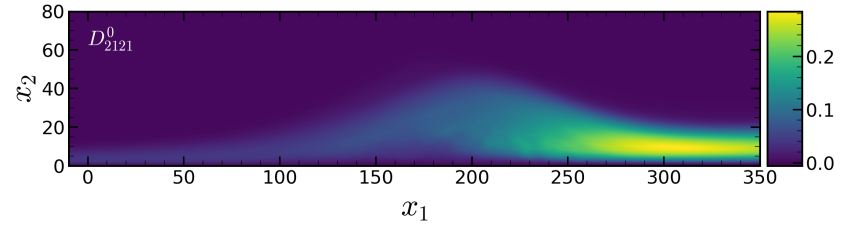

(d) D^0_{2121}

Figure 5.6: Distribution of nonzero D^0_{ijkl} for SBLS: D^0_{1111}, D^0_{1121}, D^0_{2111}, and D^0_{2121} .

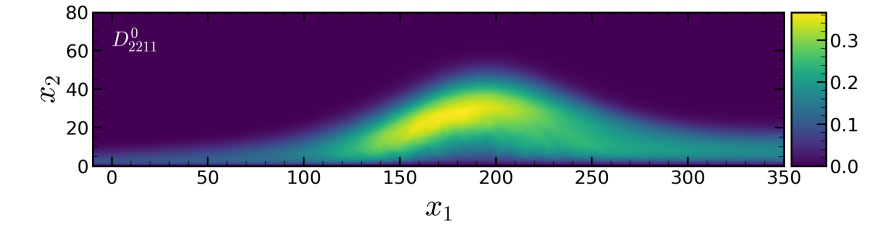

(a) D^0_{2211}

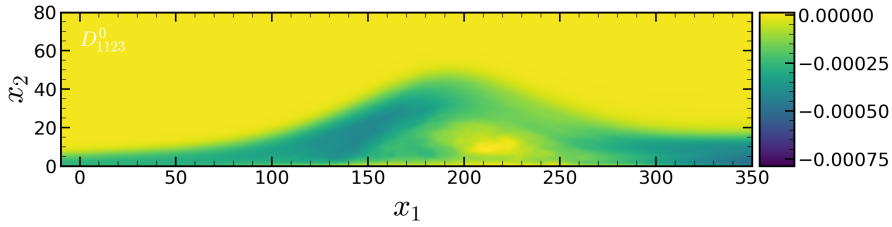

(b) D^0_{1123}

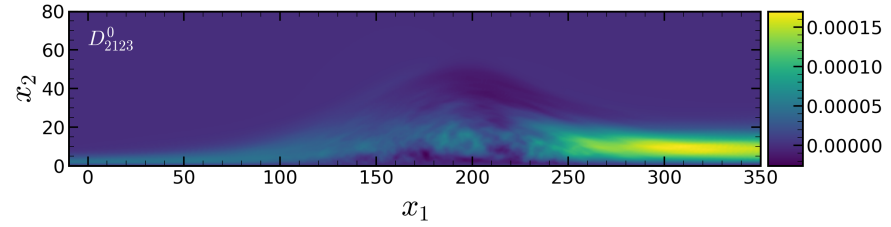

(c) D^0_{2123}

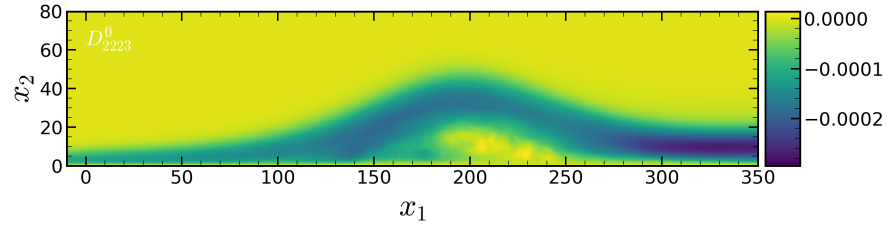

(d) D^0_{2223}

Figure 5.7: Distribution of nonzero D^0_{ijkl} for SBLS: D^0_{2211}, D^0_{1123}, D^0_{2123}, and D^0_{2223}.

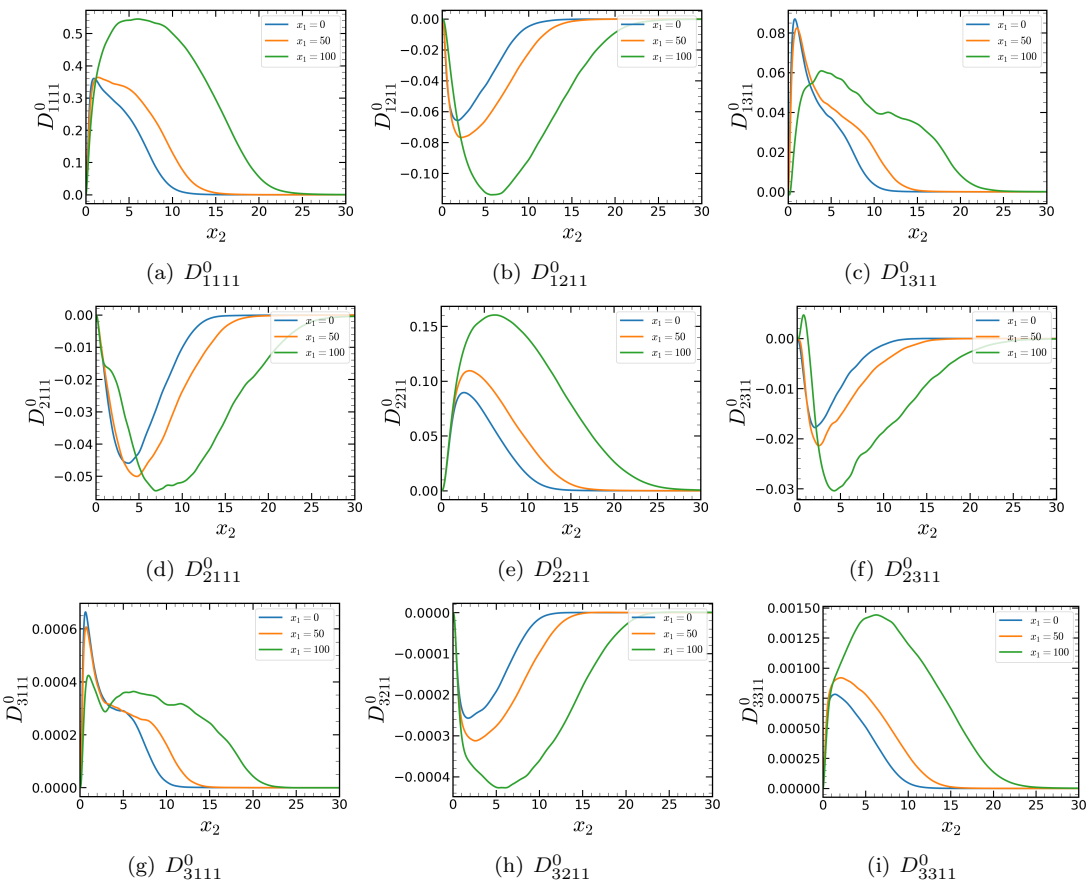

(a) D^0_{1111} (b) D^0_{1211} (c) D^0_{1311}

(d) D^0_{2111} (e) D^0_{2211} (f) D^0_{2311}

(g) D^0_{3111} (h) D^0_{3211} (i) D^0_{3311}

Figure 5.8: Distribution of nonzero D^0_{ij11} for SBLS before separation.

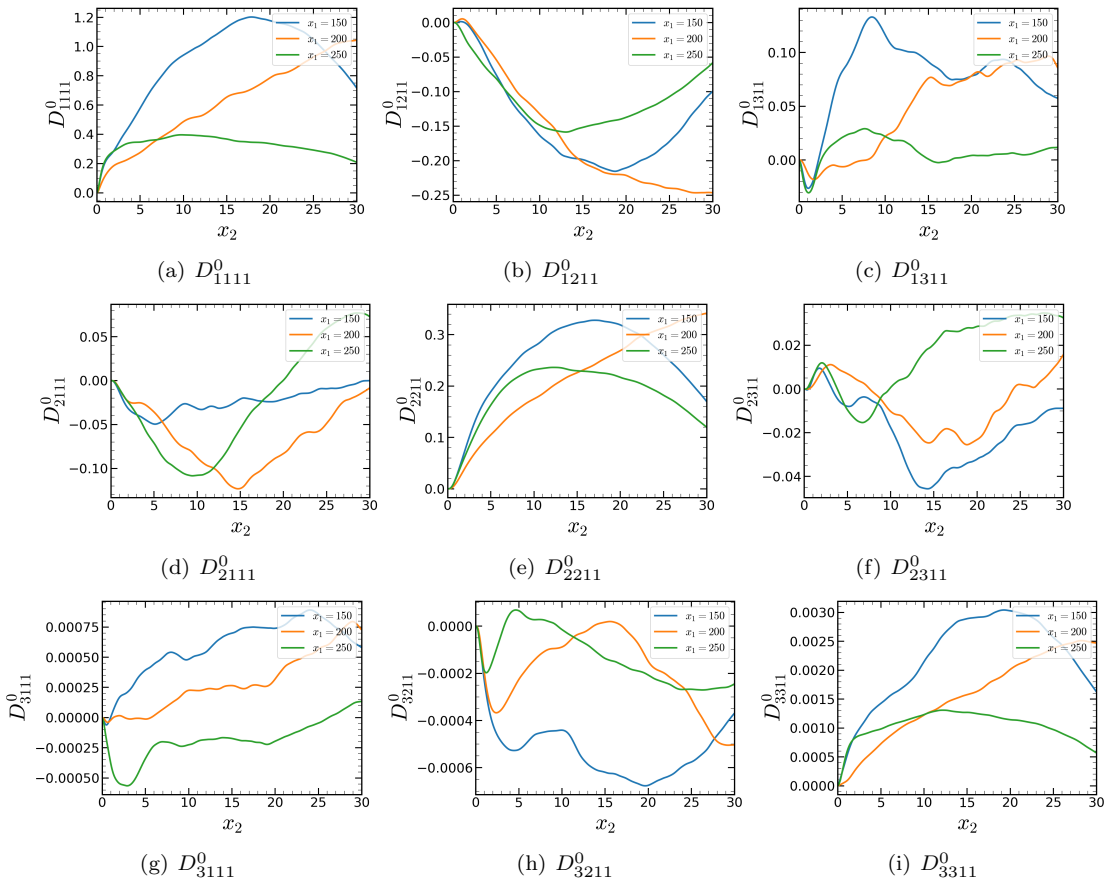

(a) D^0_{1111} (b) D^0_{1211} (c) D^0_{1311}

(d) D^0_{2111} (e) D^0_{2211} (f) D^0_{2311}

(g) D^0_{3111} (h) D^0_{3211} (i) D^0_{3311}

Figure 5.9: Distribution of nonzero D^0_{ij11} for SBLS after separation.

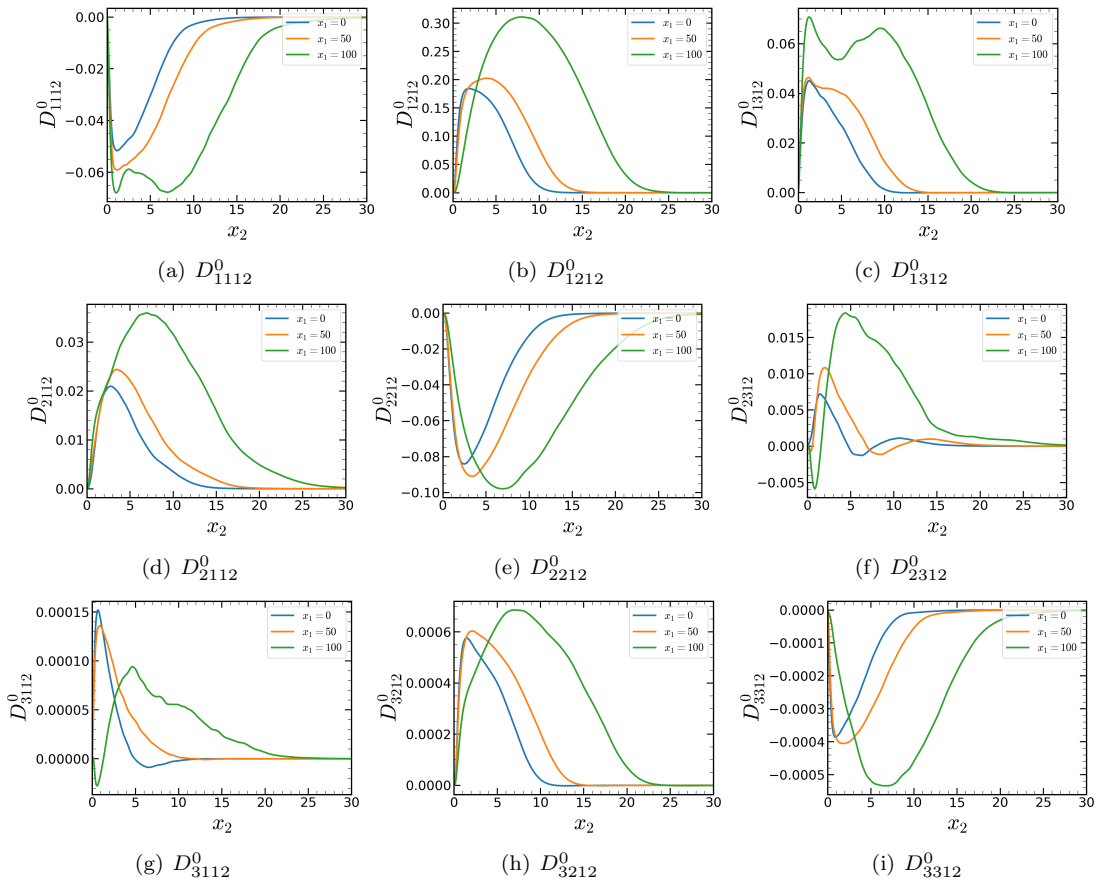

(a) D^0_{1112} (b) D^0_{1212} (c) D^0_{1312}

(d) D^0_{2112} (e) D^0_{2212} (f) D^0_{2312}

(g) D^0_{3112} (h) D^0_{3212} (i) D^0_{3312}

Figure 5.10: Distribution of nonzero D^0_{ij12} for SBLS before separation.

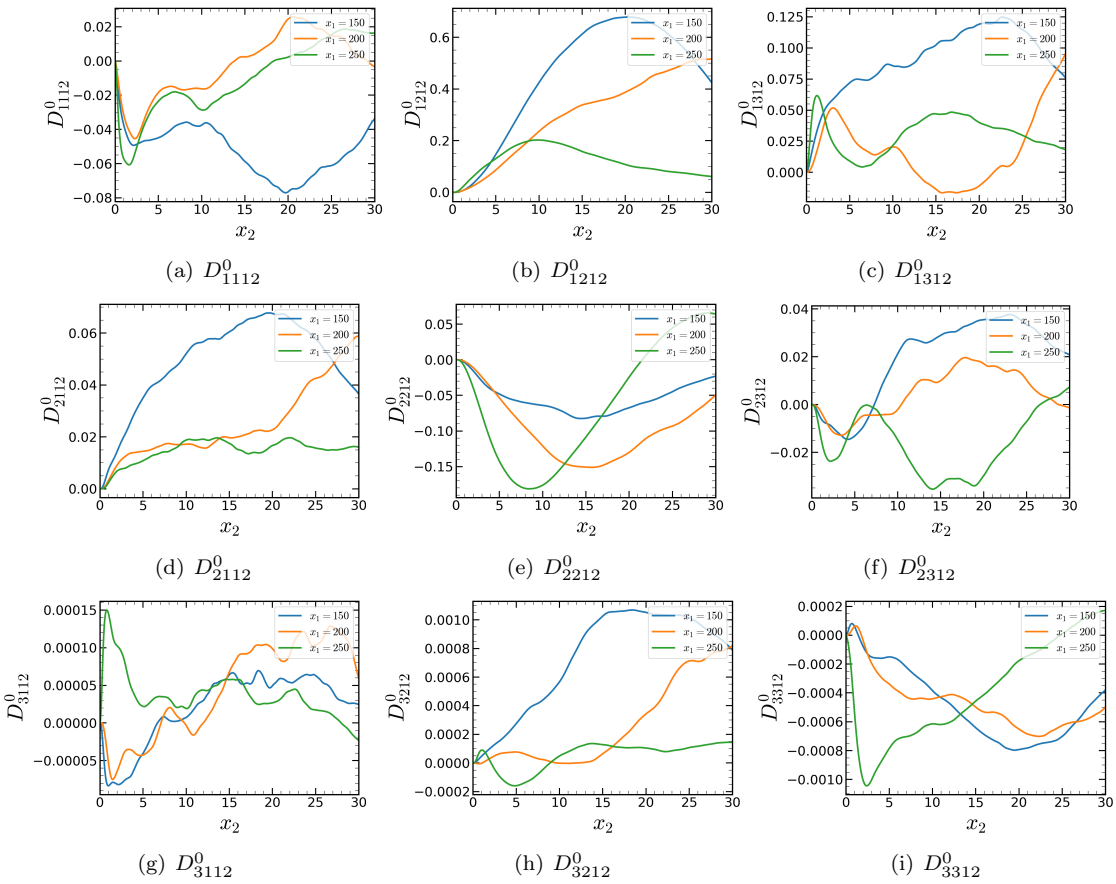

(a) D^0_{1112} (b) D^0_{1212} (c) D^0_{1312}

(d) D^0_{2112} (e) D^0_{2212} (f) D^0_{2312}

(g) D^0_{3112} (h) D^0_{3212} (i) D^0_{3312}

Figure 5.11: Distribution of nonzero D^0_{ij12} for SBLS after separation.

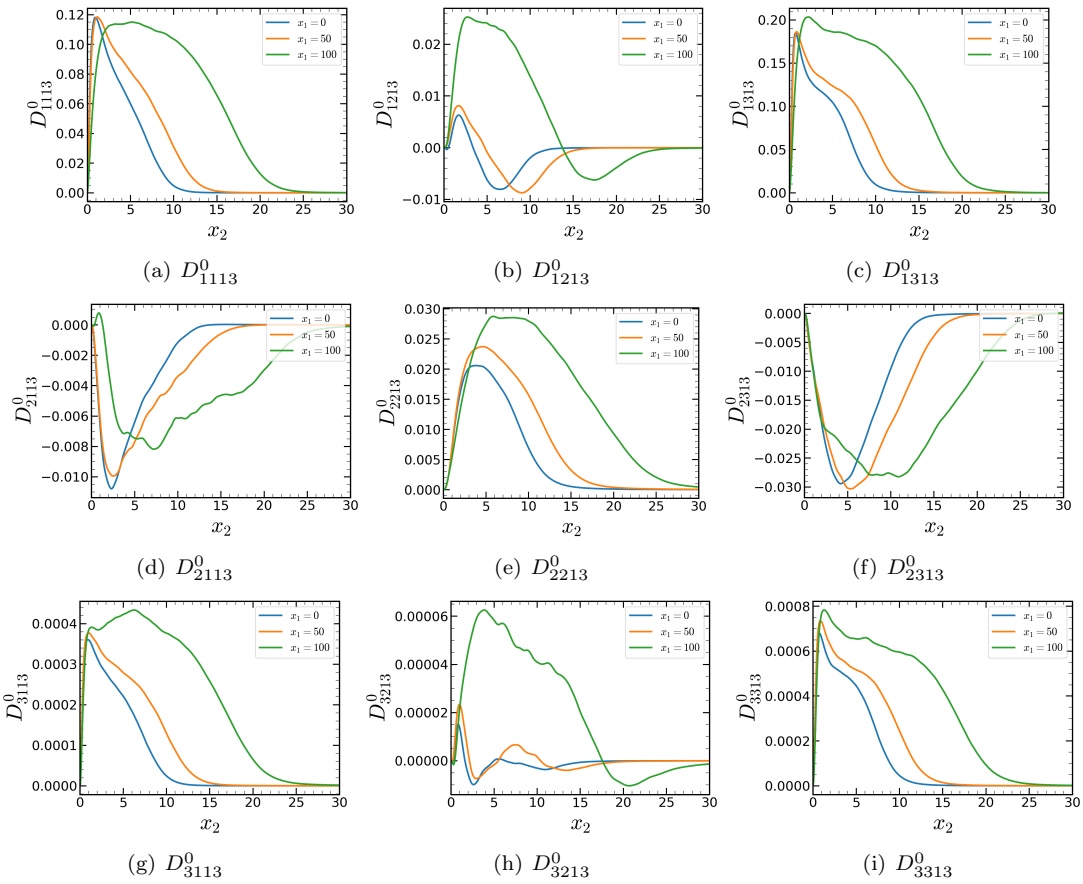

(a) D^0_{1113} (b) D^0_{1213} (c) D^0_{1313}

(d) D^0_{2113} (e) D^0_{2213} (f) D^0_{2313}

(g) D^0_{3113} (h) D^0_{3213} (i) D^0_{3313}

Figure 5.12: Distribution of nonzero D^0_{ij13} for SBLS before separation.

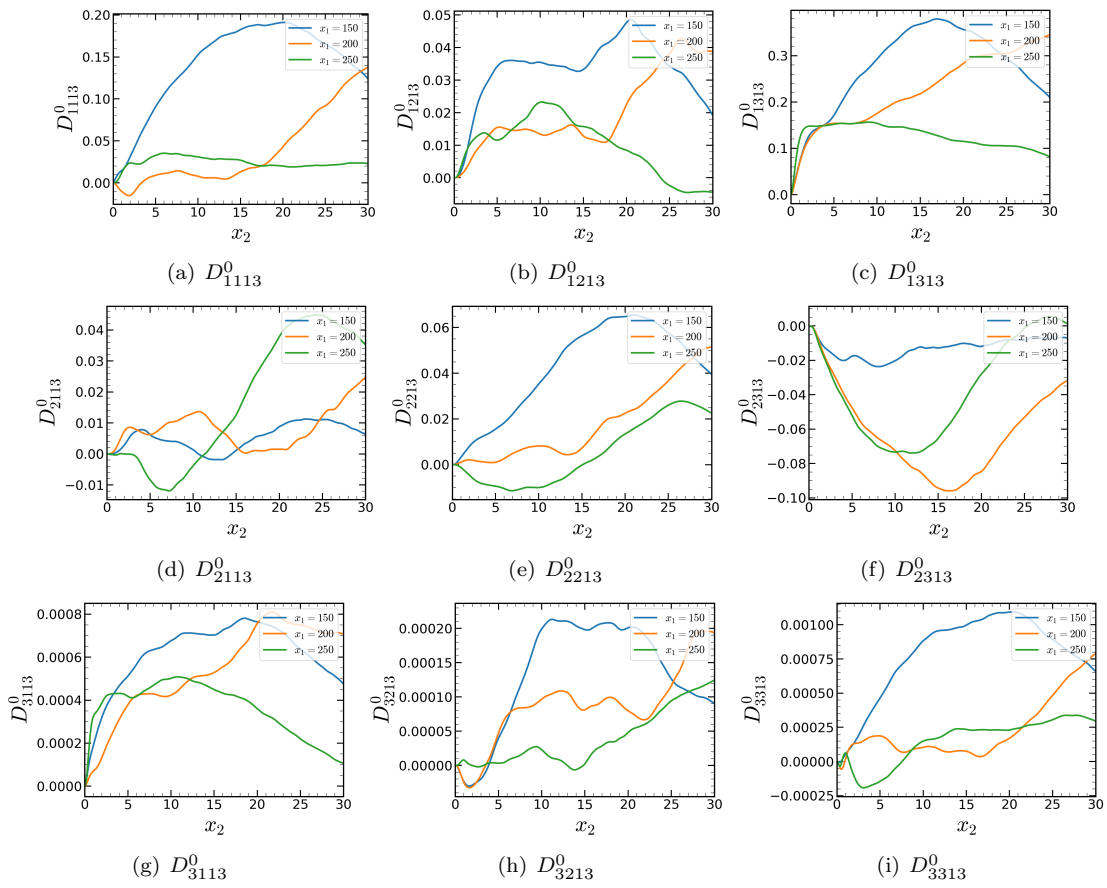

(a) D^0_{1113} (b) D^0_{1213} (c) D^0_{1313}

(d) D^0_{2113} (e) D^0_{2213} (f) D^0_{2313}

(g) D^0_{3113} (h) D^0_{3213} (i) D^0_{3313}

Figure 5.13: Distribution of nonzero D^0_{ij13} for SBLS after separation.

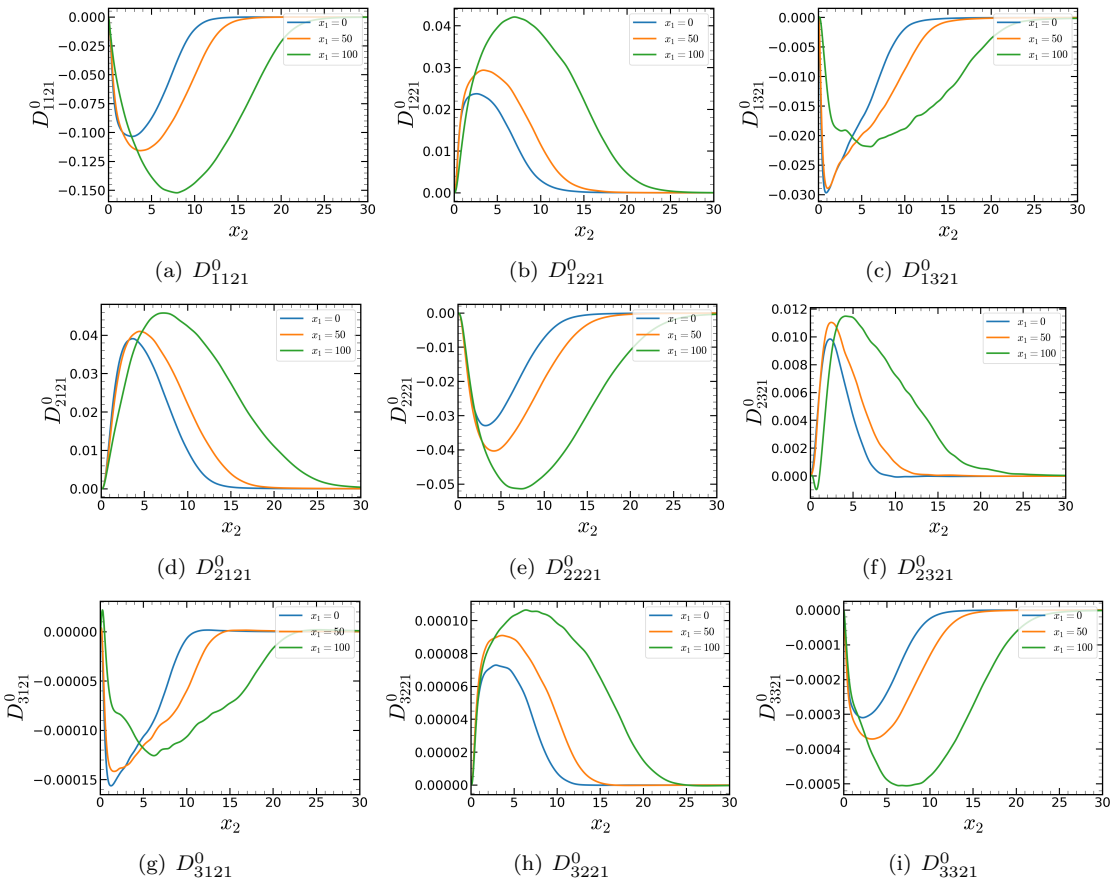

(a) D^0_{1121} (b) D^0_{1221} (c) D^0_{1321}

(d) D^0_{2121} (e) D^0_{2221} (f) D^0_{2321}

(g) D^0_{3121} (h) D^0_{3221} (i) D^0_{3321}

Figure 5.14: Distribution of nonzero D^0_{ij21} for SBLS before separation.

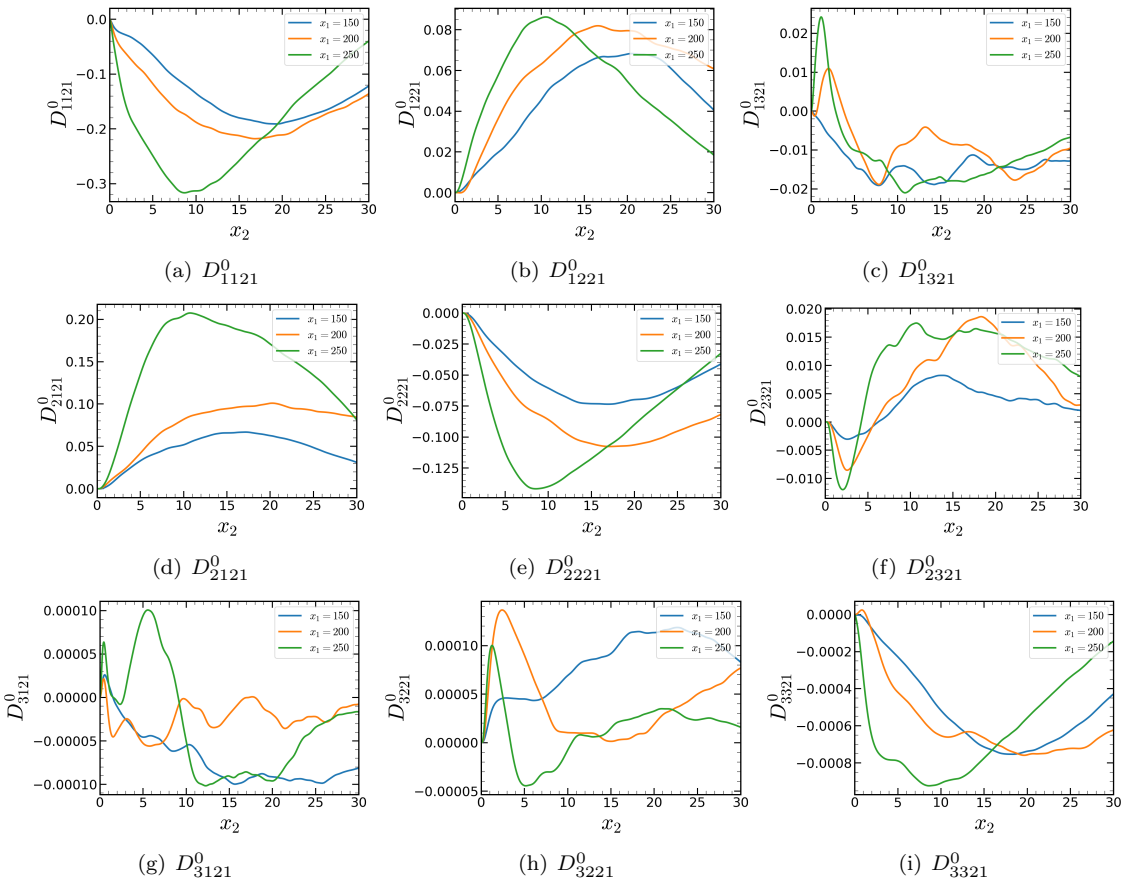

(a) D^0_{1121} (b) D^0_{1221} (c) D^0_{1321}

(d) D^0_{2121} (e) D^0_{2221} (f) D^0_{2321}

(g) D^0_{3121} (h) D^0_{3221} (i) D^0_{3321}

Figure 5.15: Distribution of nonzero D^0_{ij21} for SBLS after separation.

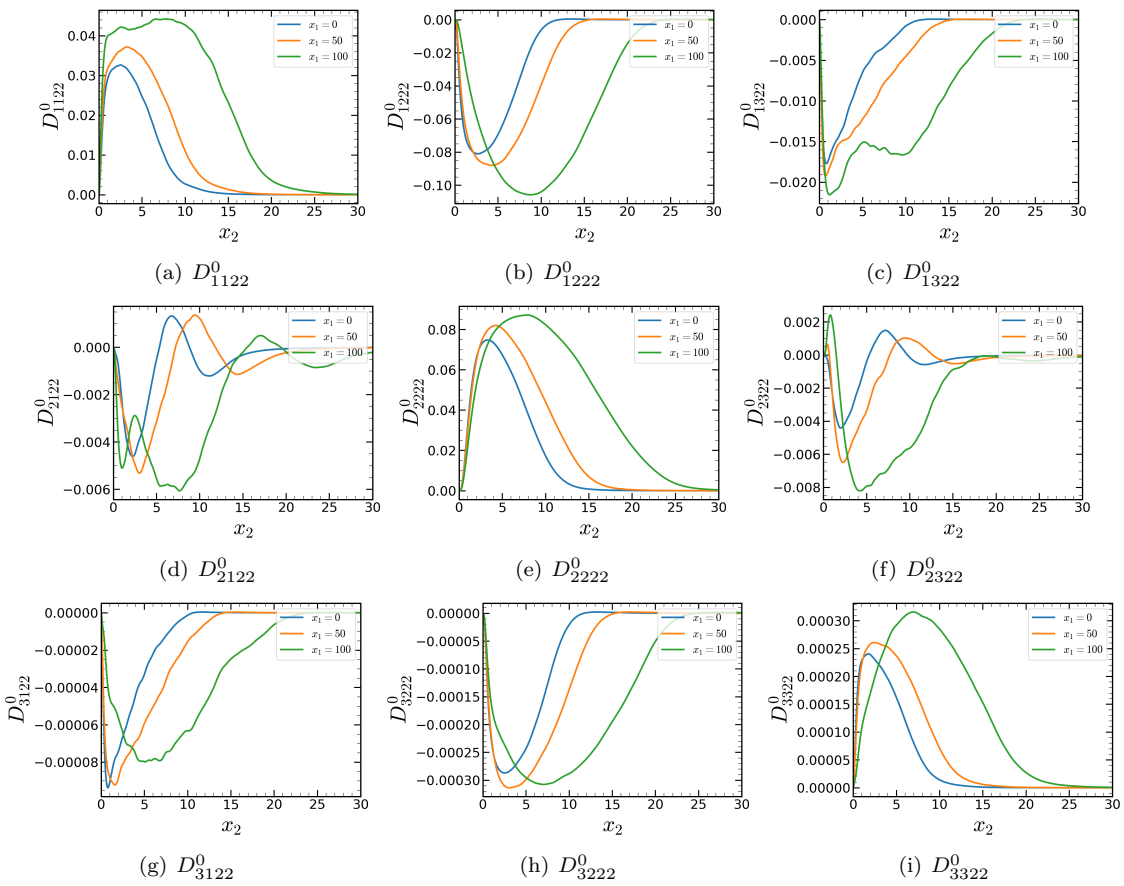

(a) D^0_{1122} (b) D^0_{1222} (c) D^0_{1322}

(d) D^0_{2122} (e) D^0_{2222} (f) D^0_{2322}

(g) D^0_{3122} (h) D^0_{3222} (i) D^0_{3322}

Figure 5.16: Distribution of nonzero D^0_{ij22} for SBLS before separation.

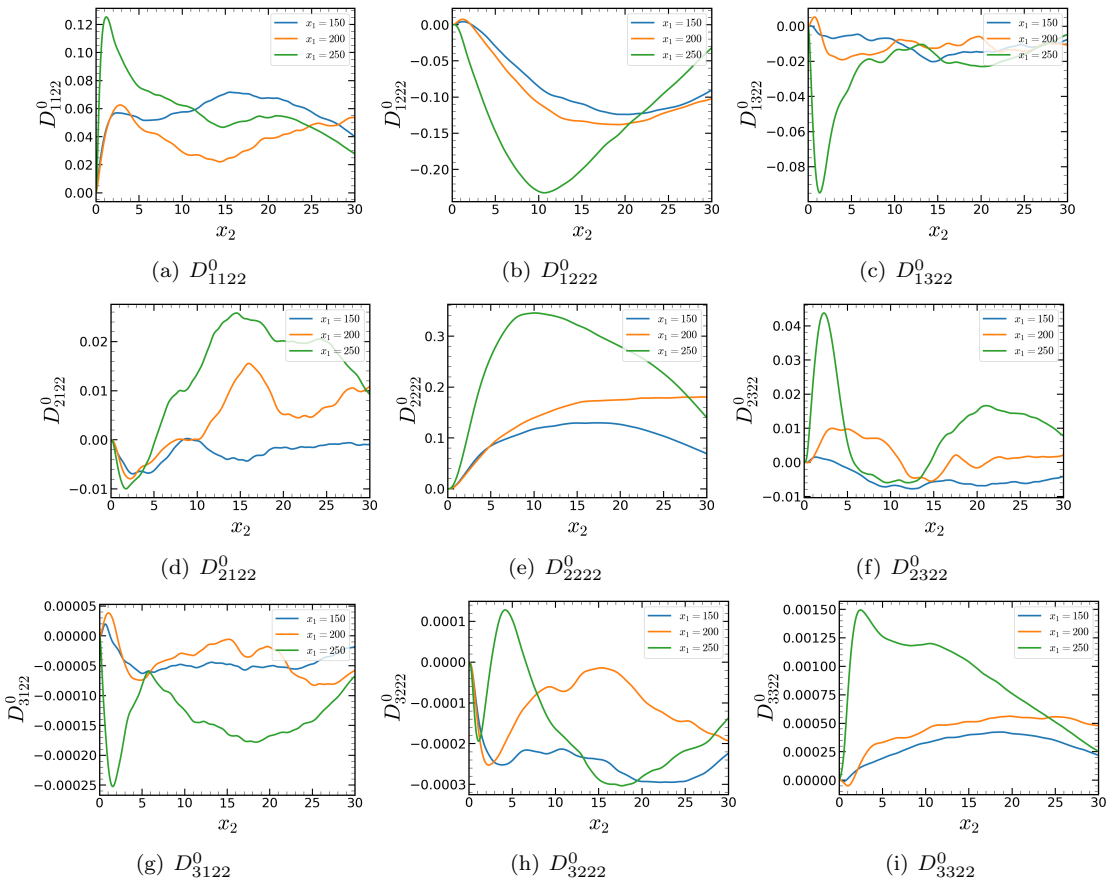

(a) D^0_{1122} (b) D^0_{1222} (c) D^0_{1322}

(d) D^0_{2122} (e) D^0_{2222} (f) D^0_{2322}

(g) D^0_{3122} (h) D^0_{3222} (i) D^0_{3322}

Figure 5.17: Distribution of nonzero D^0_{ij22} for SBLS after separation.

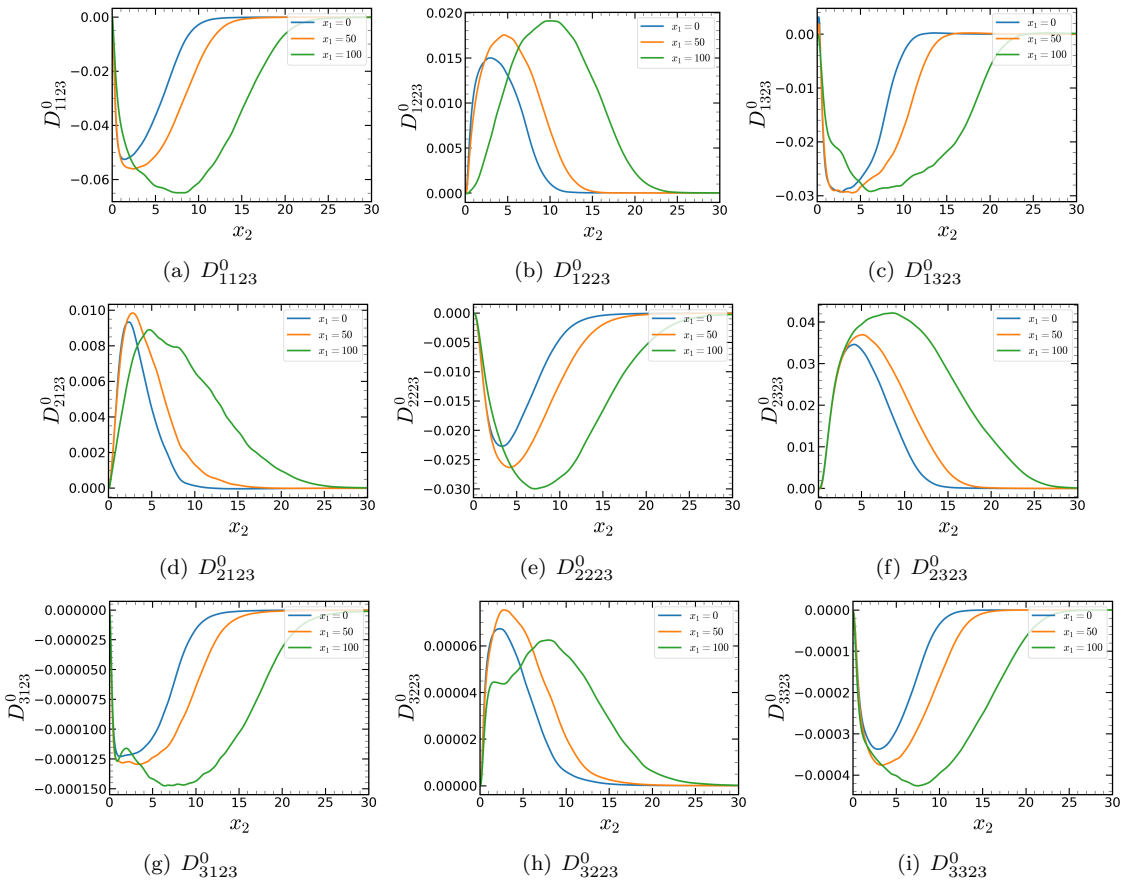

(a) D^0_{1123} (b) D^0_{1223} (c) D^0_{1323}

(d) D^0_{2123} (e) D^0_{2223} (f) D^0_{2323}

(g) D^0_{3123} (h) D^0_{3223} (i) D^0_{3323}

Figure 5.18: Distribution of nonzero D^0_{ij23} for SBLS before separation.

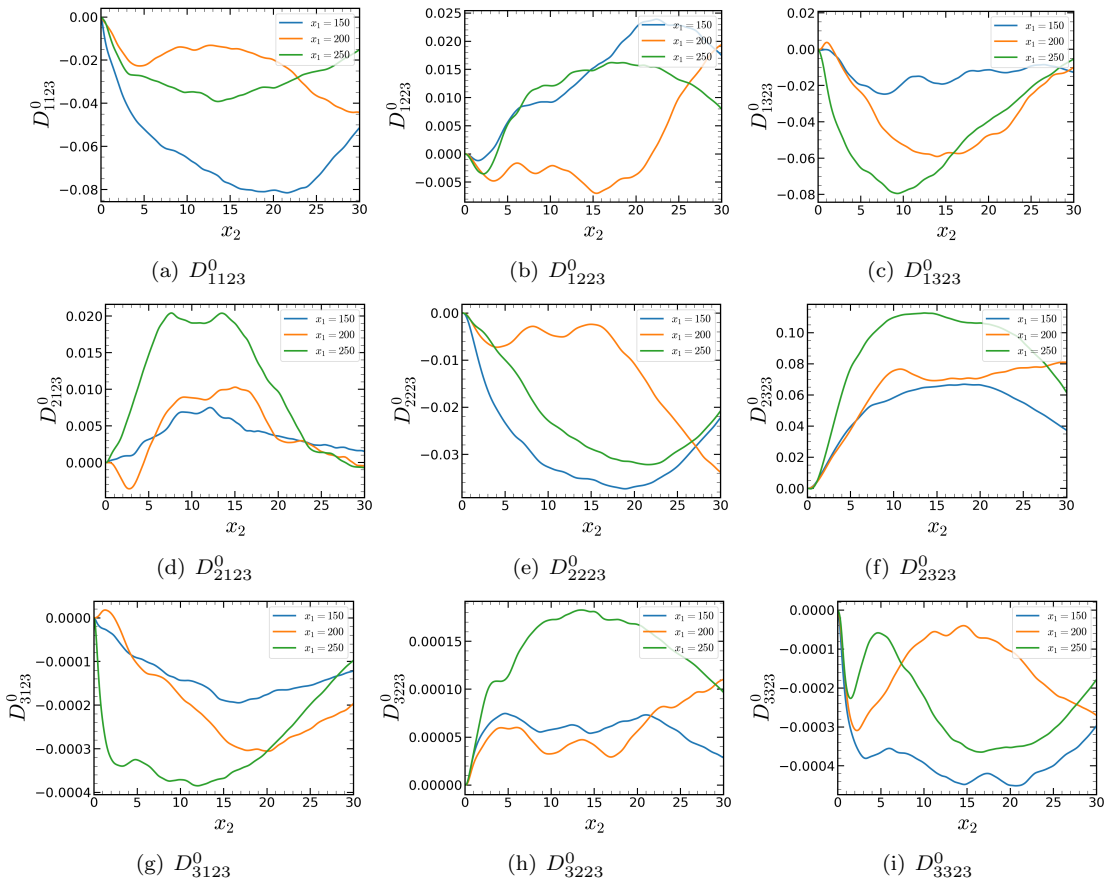

(a) D^0_{1123} (b) D^0_{1223} (c) D^0_{1323}

(d) D^0_{2123} (e) D^0_{2223} (f) D^0_{2323}

(g) D^0_{3123} (h) D^0_{3223} (i) D^0_{3323}

Figure 5.19: Distribution of nonzero D^0_{ij23} for SBLS after separation.

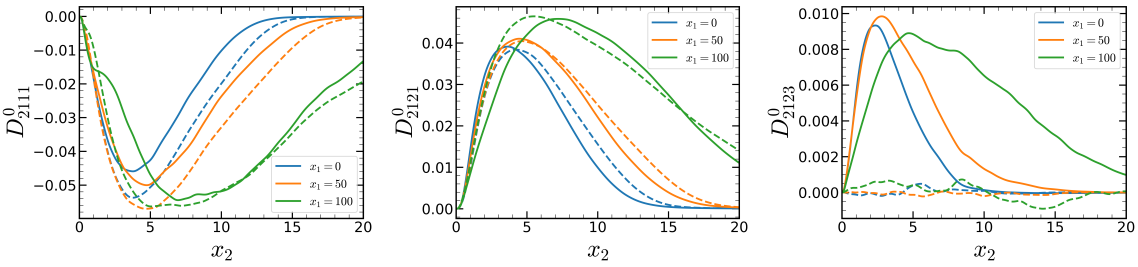

(a) D^0_{2111} (b) D^0_{2121} (c) D^0_{2123}

Figure 5.20: Distribution of D^0_{2111}, D^0_{2121}, and D^0_{2123} for SBL (dashed) and SBLS (solid).

5.1.4 Leading-order Eddy Viscosity Tensor Comparison

Figure 5.20 illustrates the eddy viscosity components, D^0_{2111}, D^0_{2121}, and D^0_{2123}, at three different locations along the x_1 axis: $x_1 = 0$, $x_1 = 50$, and $x_1 = 100$. These components contribute to the Reynolds stress of $\overline{u_2' u_1'}$. The solid and dashed lines represent the eddy viscosity components from SBLS and SBL, respectively. The D^0_{2111} and D^0_{2121} components have similar shapes and magnitudes between the unswept and swept cases, with limited quantitative differences between the two flows. However, the swept case shows a distinct structure for the D^0_{2123} component, while the unswept case has zero D^0_{2123} ignoring the statistical noise. The substantial magnitude of D^0_{2123} is not surprising at $x_1 = 0$, where there is a significant difference between SBL and SBLS in the Reynolds stress comparison. However, it is surprising that even at $x_1 = 100$, a finite level of D^0_{2123} is present, since previous work has perceived IP in this zone. Therefore, further investigation is needed to determine how this difference in eddy viscosity affects the Reynolds stress.

5.1.5 Sweep Effect Analysis using MFM Measurements

Using the eddy viscosity components, the entire Reynolds stress can be reconstructed as shown in Figure 5.24. The solid line represents the SBLS case, while the dashed lines represent the SBL case, with two different zones shown: the upstream TBL zone at $x_1 = 0$ and the zone near the separation at $x_1 = 100$. The green lines represent $D^0_{2111}\, \partial U_1/\partial x_1$, where D^0_{2111} is from the MFM measurement and $\partial U_1/\partial x_1$ is from the DNS. The red, purple, brown, pink, and grey lines are $D^0_{2121}\, \partial U_1/\partial x_2$, $D^0_{2112}\, \partial U_2/\partial x_1$, $D^0_{2122}\, \partial U_2/\partial x_2$, $D^0_{2113}\, \partial U_3/\partial x_1$, and $D^0_{2123}\, \partial U_3/\partial x_2$, respectively. The orange line represents the summation of all the eddy viscosity contributions to the Reynolds stress: $D^0_{21kl}\, \partial U_l/\partial x_k$.

The sweep effect should be quantified through examining the grey and pink lines, which represent the contribution of the spanwise velocity gradient to a dominant component of the Reynolds stress which contributes to the budget of the U_1 momentum. If these two lines were zero, then we would be able to confirm IP since the spanwise velocity gradients would not influence the in-plane momentum.

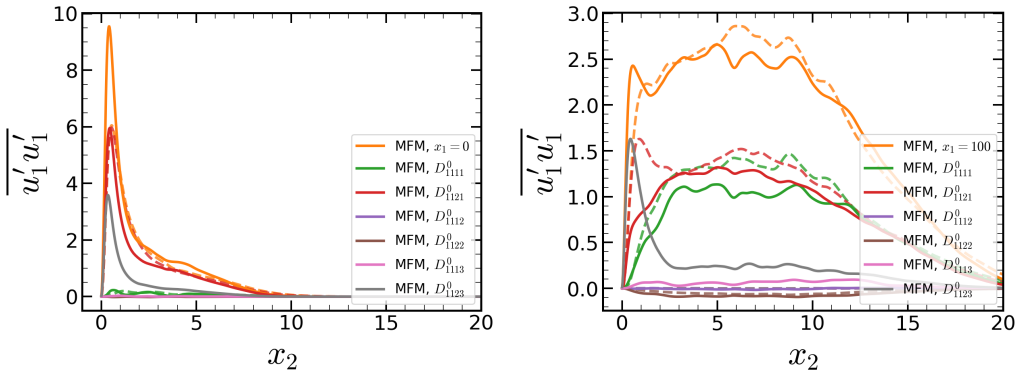

(a) $x_1 = 0$ (b) $x_1 = 100$

Figure 5.21: Reynolds Stress $\overline{u_1'u_1'}$ at given x_1 from DNS, MFM, and MFM eddy viscosity components for SBL (dashed) and SBLS (solid).

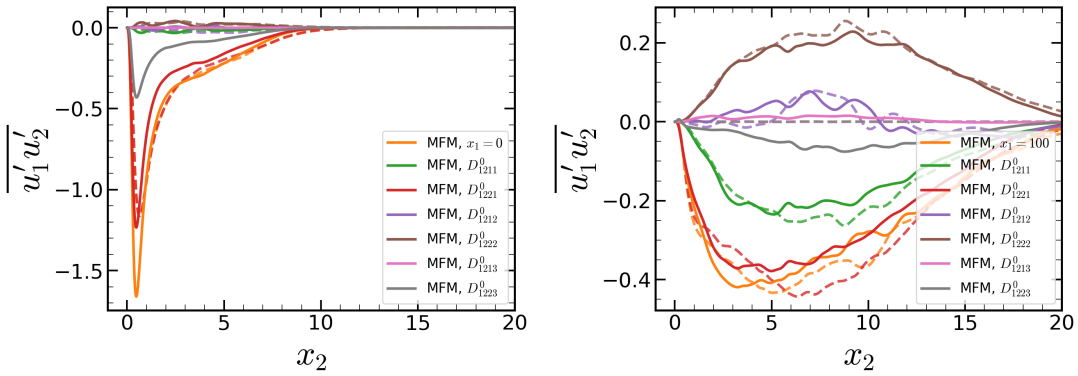

(a) $x_1 = 0$ (b) $x_1 = 100$

Figure 5.22: Reynolds Stress $\overline{u_1'u_2'}$ at given x_1 from DNS, MFM, and MFM eddy viscosity components for SBL (dashed) and SBLS (solid).

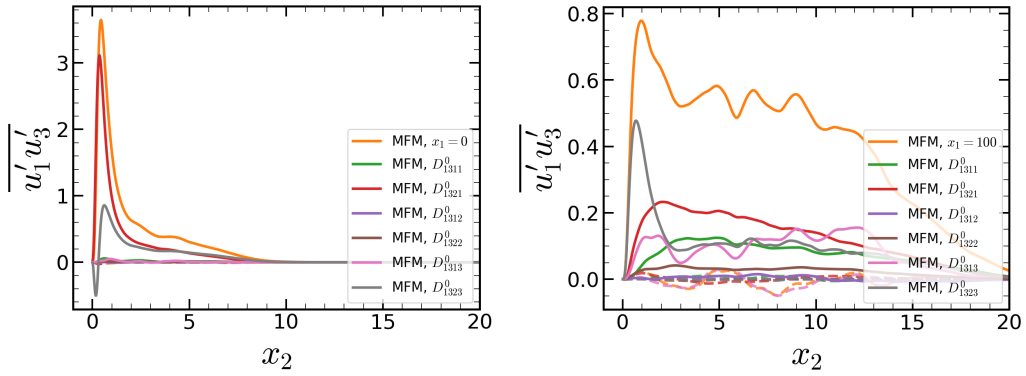

(a) $x_1 = 0$ (b) $x_1 = 100$

Figure 5.23: Reynolds Stress $\overline{u_1'u_3'}$ at given x_1 from DNS, MFM, and MFM eddy viscosity components for SBL (dashed) and SBLS (solid).

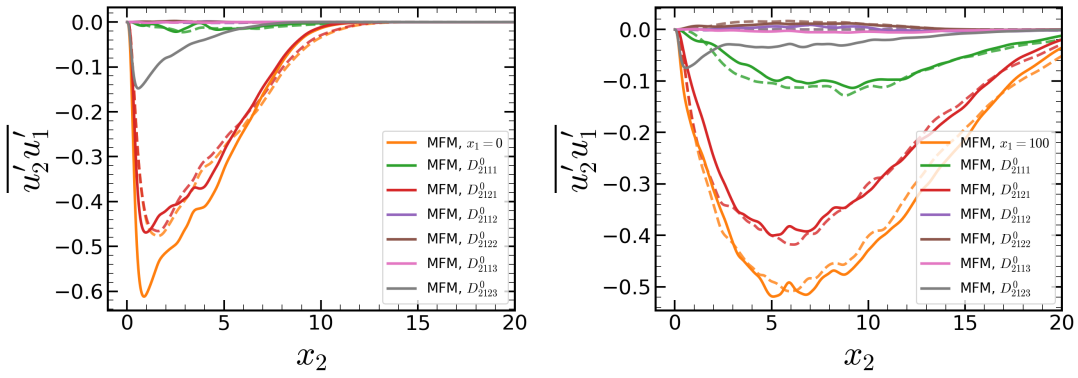

(a) $x_1 = 0$ (b) $x_1 = 100$

Figure 5.24: Reynolds Stress $\overline{u_2'u_1'}$ at given x_1 from DNS, MFM, and MFM eddy viscosity components for SBL (dashed) and SBLS (solid).

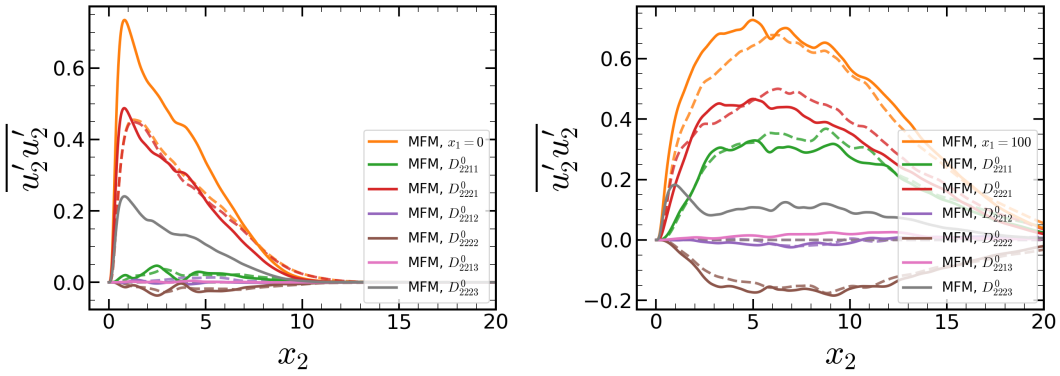

(a) $x_1 = 0$ (b) $x_1 = 100$

Figure 5.25: Reynolds Stress $\overline{u_2'u_2'}$ at given x_1 from DNS, MFM, and MFM eddy viscosity components for SBL (dashed) and SBLS (solid).

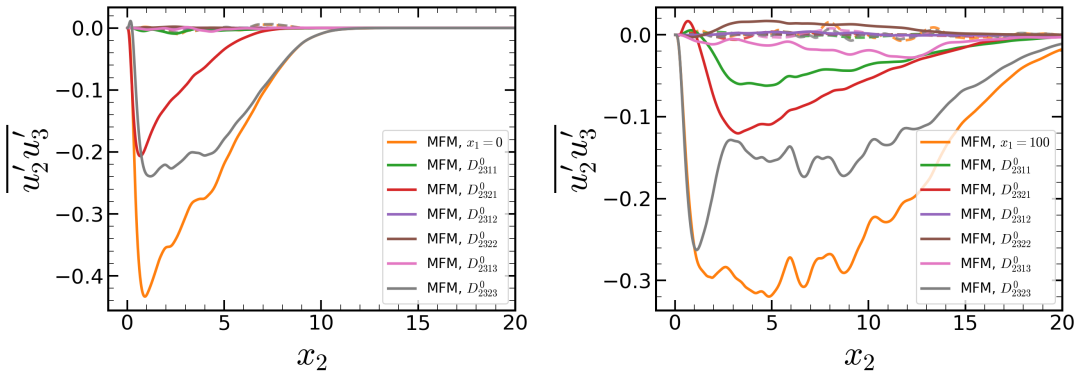

(a) $x_1 = 0$ (b) $x_1 = 100$

Figure 5.26: Reynolds Stress $\overline{u_2'u_3'}$ at given x_1 from DNS, MFM, and MFM eddy viscosity components for SBL (dashed) and SBLS (solid).

Figure 5.24(a) shows that, for the SBL case, most of the Reynolds stress comes from the D^0_{2121} components. However, for the swept case, the D^0_{2121} values between SBL and SBLS are similar, and the newly introduced D^0_{2123} adds to the total value of the Reynolds stress, increasing the magnitude of Reynolds stress for the SBLS case. This is consistent with previous DNS data that indicates the sweep effect is present in the $x_1 = 0$ zone.

Most importantly, we examine in Figure 5.24(b) the sweep effects near the separation zone. In this zone, a non-negligible portion of the Reynolds stress is contributed by D^0_{2123}, particularly in the near wall zone. This observation is in contradiction with Coleman et al.[14] conclusion. In contrast to their assessment of IP validity near the separation zone, we observe and quantify influence of spanwise flow gradients on an in-plane momentum component. Quantification in terms of eddy viscosity components has been critical in reaching this conclusion, since the total Reynolds stress as used in Coleman et al., does not provide a clear picture.

5.2 Coordinate Transformation of Eddy Viscosity

In the previous subsection, we compared the eddy viscosity of SBL and SBLS in the same Cartesian coordinate system, focusing on the measured anisotropic nature of the eddy viscosity, particularly the significant differences in the D^0_{ij3k} components, which represent the sweep effect. Another approach to analyze the eddy viscosity is to use a coordinate system that aligns with the streamwise direction, instead of the chordwise direction. This way, we can identify patterns in the eddy viscosity that are more generalizable to the flow system and are subject to the velocity coordinate.

Using the full components of the anisotropic and local eddy viscosity tensor, we can rotate the eddy viscosity tensor to any set of coordinate systems. The formulation for the rotation is the following:

$$D^0_{i'j'k'l'} = c_{i'i}c_{j'j}c_{k'k}c_{l'l}D^0_{ijkl}, \tag{5.1}$$

where $c_{i'i}$ is the direction cosine for the new coordinate direction x'_i and the original coordinate direction x_i, and $D^0_{i'j'k'l'}$ is the resulting rotated eddy viscosity.

For the coordinate transformation, we utilized a rotated coordinate system, where the coordinates in the x_1 and x_3 plane are rotated by the sweep angle α, in our case 35°. Since all points undergo the same amount of rotation. However, due to our simulation not calculating the D^0_{ij3l} components, we were unable to compute a subset of the rotated eddy viscosity components. Therefore, in this section, we report only the $D^0_{i'j'2'l'}$ components of the eddy viscosity that do not require the D^0_{ij3l} components, based on the coordinate transformation in the x_1-x_3 plane.

Figure 5.27 displays five distinct components of the anisotropic local eddy viscosity in three different coordinate systems at $x_1 = 0$. The components are D^0_{1121}, D^0_{2121}, D^0_{1123}, D^0_{2123}, and D^0_{2223}. First, Figure 5.27(a) presents the eddy viscosity for SBL in the original coordinate system, which is

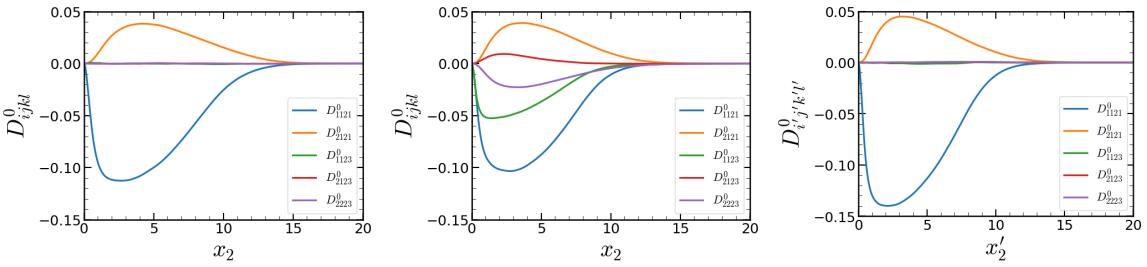

(a) SBL (b) SBLS (c) SBLS in rotated coordinate

Figure 5.27: Eddy viscosity comparison for SBL and SBLS in the original coordinate system and SBLS in rotated coordinate system using globally uniform rotated coordinate at $x_1 = 0$.

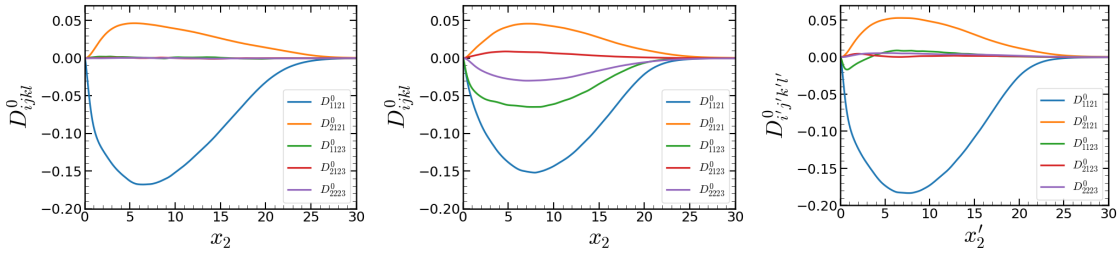

(a) SBL (b) SBLS (c) SBLS in rotated coordinate

Figure 5.28: Eddy viscosity comparison for SBL and SBLS in the original coordinate system and SBLS in rotated coordinate system using globally uniform rotated coordinate at $x_1 = 100$.

aligned with the chordwise direction in the Cartesian coordinate system. In this case, it is observed that the D^0_{1123}, D^0_{2123}, and D^0_{2223} components are all zero, as expected, since they represent the sweep effect. Subsequently, Figure 5.27(b) presents a similar setup, but now with SBLS, where the original coordinate system is used. Upon comparing these two figures, it is evident that the D^0_{1121} and D^0_{2121} components are similar, while the remaining three components now have finite values. This is due to the inclusion of the sweep effect, as explained in the previous section. Finally, Figure 5.27(c) presents the eddy viscosity in the rotated coordinate system. In this case, it is observed that the distribution of eddy viscosity components is qualitatively similar to that of the SBL case. The mixing effects of the sweep D^0_{ijk3} components are now incorporated into the D^0_{1121} and D^0_{2121} components. However, actual quantities differ between Figure 5.27(a) and Figure 5.27(c), as the latter case includes larger kinetic energy and hence exhibits larger mixing effects.

Figure 5.27 is comparing the eddy viscosity components at $x_1 = 0$, which is near the turbulent boundary layer zone. In Figure 5.28, we are comparing the eddy viscosity in the same manner but now at $x_1 = 100$, which is near the separation point. For Figure 5.28(b), we notice that D^0_{1123}, D^0_{2123}, and D^0_{2223} are non-zero for the swept case as in the attached zone. However, unlike the attached zone, we see that D^0_{1123} has a non-negligible value in the rotated coordinate, due to the

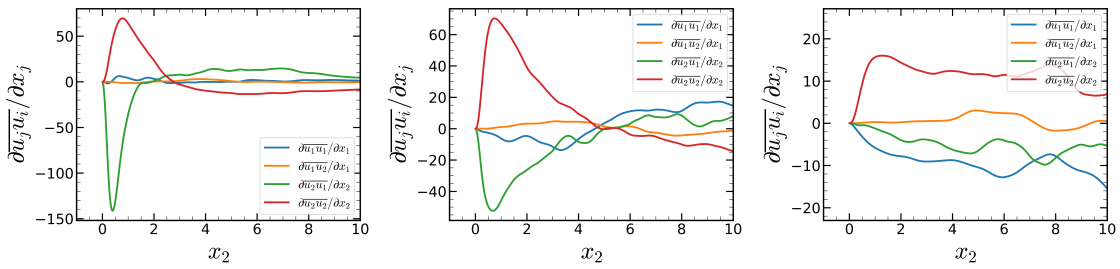

(a) $x_1 = 0$ (b) $x_1 = 100$ (c) $x_1 = 150$

Figure 5.29: Momentum balance of Reynolds stress at three different locations.

more complex flow topology near the separation.

5.3 Key Components of Anisotropic Eddy Viscosity

We used MFM and momentum budget analysis to identify the important eddy viscosity components. Figure 5.29 illustrates the momentum balance of Reynolds stress at three chordwise locations in swept flow: attached zone (a), near separation (b), and middle of the bubble (c). Each subplot has four plots for $\partial\overline{u_j u_i}/\partial x_j$, where $\partial\overline{u_j u_1}/\partial x_j$ affects chordwise momentum and $\partial\overline{u_j u_2}/\partial x_j$ affects wall-normal momentum. We found that $\partial\overline{u_2 u_1}/\partial x_2$ and $\partial\overline{u_2 u_2}/\partial x_2$ are important for near separation and early bubble, while $\partial\overline{u_1 u_1}/\partial x_1$ additionally becomes significant at the middle of the bubble. Based on the eddy viscosity tensorial notation, we identified that D^0_{11kl}, D^0_{21kl}, and D^0_{22kl} are important components, while D^0_{12kl} is less important.

Additionally, we conducted a momentum budget analysis for the Reynolds stress, examining each eddy viscosity component's contribution to the Reynolds stress similar to what was previously shown in Figure 5.24. Through this analysis, we identified eight significant components of the anisotropic eddy viscosity - D^0_{1111}, D^0_{1121}, D^0_{2111}, D^0_{2121}, D^0_{2211}, D^0_{1123}, D^0_{2123}, and D^0_{2223}. The first five components were identified from SBL analysis from Section 4.4, while the last three were added due to the sweep effect considered in this study. It's essential to note that standard RANS models with Boussinesq approximation involve zero D^0_{ij23} when i and j are the in-plane components (i, $j = 1$ or 2). Even anisotropic modifications to the Boussinesq-type model, such as quadratic constitutive relation (QCR) [60], maintain zero sensitivity of some of the in-plane components of Reynolds stresses to spanwise gradients. Specifically these models maintain effectively no representation of D^0_{1123}. The presented results provide detailed quantification of anisotropy in momentum mixing. While indicating the lacking points of some of the existing modeling frameworks.

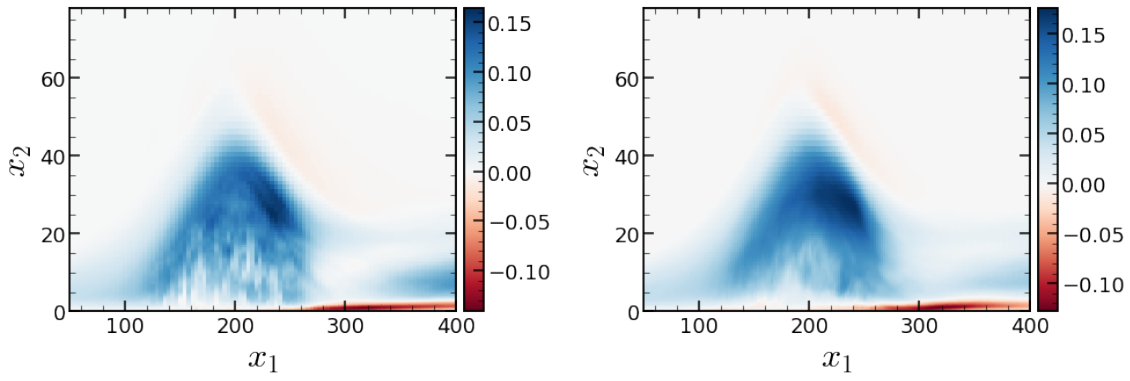

(a) SBL

(b) SBLS

Figure 5.30: Minimum eigenvalue of the symmetric part of the eddy viscosity tensor for (a) SBL and (b) SBLS.

5.4 Physical Constraints on the Eddy Viscosity and Numerical Robustness

Likewise for SBLS, we conducted positive definiteness analysis for the measured D^0_{ijkl} similarly to that of the unswept case. Figure 5.30 shows the minimum eigenvalue associated with the symmetric part of the measured eddy viscosity tensor of the swept boundary layer (b), along with the unswept case that was previously shown in Figure 4.19. The negative zone shown in this figure refers to the zone where positive semidefiniteness is violated. In both SBL and SBLS, a similar pattern is observed, with two prominent regions containing negative eigenvalues. The first region, situated at the top of the bubble, is a region where non-positive definite D^0_{ijkl} is coinciding with a region of negative production signifying importance of nonlocality, aligning with findings previously reported in works by Abe and Coleman [3, 13]. The second region, occurring after the bubble reattachment, shows a highly nonlocal area, in alignment with our prior analysis of RANS results in Section 4.4.

Furthermore, we attempted to modify the leading-order eddy viscosity tensor for SBLS to make the tensor positive semidefinite, similar to what we did in Section 5.4. However, for SBLS, the complex nature of the flow prevented us from identifying a suitable modification and therefore for this flow we limit our study to a priori analyses that use the DNS mean flow as an input to the RANS closure. We conclude that for this flow, proper mitigation of lack of positive definiteness of the local eddy viscosity likely requires RANS closures that formally include the nonlocal effects rather than artificially modifying the measured local eddy viscosity to become positive definite.

Chapter 6

Conclusion

In this research, we presented a quantification of RANS closure as an operator for wall-bounded turbulent flows using DNS and MFM techniques, with a focus on understanding the anisotropy and nonlocality of momentum mixing caused by turbulent eddies. To achieve this, we examined three different flow systems that mimic flow phenomena around an airplane wing, selected based on an analysis of surface streamlines and skin friction contours. We specifically provided eddy viscosity data and explored non-Boussinesq effects in different flow systems, aiming to offer valuable insights into the dynamics of turbulent mixing in various flow configurations involving wall-bounded turbulent flows.

In the first study, we provided a quantification of non-Boussinesq effects in eddy viscosity in a turbulent channel flow. The analyses presented were systematically focused on two aspects: anisotropy and nonlocality of momentum mixing. Combining DNS with MFM, we measured the leading-order eddy viscosity tensor for the analysis of anisotropy and extended the research to measure eddy viscosity tensorial kernel for the analysis of nonlocality.

Our investigations of the parallel channel flow indicated the following: (1) the eddy viscosity is highly anisotropic with some elements an order of magnitude larger than the nominal eddy viscosity; (2) the Reynolds stresses reconstructed from this eddy viscosity depends not only on the mean rate of strain but also on mean rate of rotation; (3) the leading-order eddy viscosity, which is obtained by neglecting higher spatial moments of the closure kernel, generates a non-symmetric Reynolds stress tensor; and (4) aside from the shear component of the Reynolds stress, $\overline{u_2' u_1'}$, the dependence of other components of the Reynolds stress on the mean velocity gradient is highly nonlocal at the level where some components of the Reynolds stress are influenced by the velocity gradient on the other half of the channel.

The exact measurement of the eddy viscosity of the channel flow has different implications for RANS modeling of the parallel flow and that of the spatially developing boundary layers. For the parallel flow, only one Reynolds stress component and one velocity gradient are important;

hence anisotropy does not influence the predictions of the solution as long as D_{2121} is properly modeled. At the same time, not only the anisotropy but also nonlocality can be omitted for the channel flow since the spatial distribution of $D_{2121}(x_2, y_2)$ exhibits a relatively local distribution, as shown in our MFM measurement of the eddy viscosity kernel. These two findings explain why the Boussinesq approximation works well for parallel flows. However, our quantification suggest that this conclusion does not hold for spatially developing wall-bounded flows where the non-parallel effects become important. For instance, even a small gradient in the streamwise direction can have a non-neglible effect since D^0_{1111} is very large compared to most of other eddy viscosity components. Our measurements reveal that the eddy viscosity is highly anisotropic and highly nonlocal, when it comes to components other than D_{2121}, indicating a clear need to include non-Boussinesq effects in RANS models.

While we focused on full nonlocal analysis in the x_2 direction, we did not consider nonlocal spatial effects in other directions and nonlocal temporal effects. Equation 2.10 is a reduced version of Equation 2.6 using leading-order moments in x_1, x_3, and t. These leading-order reductions are justified for channel flow since it is statistically homogeneous in these directions, and are expected to be qualitatively valid for systems with slow variation of turbulence in these directions. While it is possible to quantitatively assess such effects with MFM, we defer analysis of streamwise and spanwise nonlocality in eddy viscosity to a future study.

In the second study, we investigated the anisotropy of the eddy viscosity in two canonical separated boundary layers. Again, using MFM, we obtained a direct measurement of the leading-order eddy viscosity for the considered separated boundary layer flows at $\mathrm{Re}_{\theta_0} = 350$ with and without sweep. The Reynolds stress closure is expanded to extract a leading operator characterizing a purely local but anisotropic eddy viscosity by using a Kramers-Moyal expansion with its coefficients representing the spatial moments of the eddy viscosity kernel. For these three-component two-dimensional flows, we provided the full characterization of the leading-order eddy viscosity tensor and identified its key anisotropy directions.

For the unswept flow, we studied the anisotropy of the local eddy viscosity and assessed its implication for local RANS models. Our results demonstrated significant anisotropy in local momentum mixing. Specifically, eddy viscosity components with significant contribution to momentum mixing were shown to be distributed differently in space. By examining selected locations we demonstrated that local ratio between these components can be large and vary substantially from location to location. To examine the impact of anisotropy on RANS predictions and on quantities of interest, we conducted a RANS simulation using the measured tensorial eddy viscosity and compared its results against predictions of the Spalart-Allmaras (SA) model [59]. Our results indicates that incorporation of anisotrpy, even at the local level, substantially improves RANS prediction, specifically quantities of interest such as friction and pressure coefficients. While the anisotropic local eddy viscosity generated results with remarkable agreement with the mean of DNS, remaining gaps in its accuracy were

noticed particularly in regions close to flow reattachment. We attributed this gap to nonlocal effects expressed by the higher-order terms in the expansion of the eddy viscosity kernel, which are not accounted for in our study. Refocusing our attention on the local level anisotropy, we identified the five key components of the eddy viscosity tensor that contribute dominantly to momentum mixing in this flow. We showed that traditional anisotropic extensions of the Boussinesq eddy viscosity, such as the QCR extension [60] are not effective in capturing quantitative impact of anisotropy when its performance was compared against the measured eddy viscosity tensor.

In the final study, we extended our analysis of momentum mixing in separated turbulent boundary layers to a more realistic scenario of a separated boundary layer with sweep. For unswept flow, the shear stress at the separation line is zero, resulting in a two-dimensional and two-component mean flow. However, in practice, most separation lines experiences non-zero mean shear along the line of separation due to the three-dimensional effects in the mean flow. To fill this gap, we utilized the approach in [14] and simulated their canonical flat plate turbulent boundary layer configuration with a spanwise sweep imposed over the boundary. The spanwise sweep is designed to result in a 35° angle between the chordwise direction and the streamwise flow outside of the boundary layer.

Our MFM analysis indicated that while the in-plane components of the eddy viscosity does not change substantially due to the imposed sweep, new out of plan components of the eddy viscosity, such as D^0_{2123} emerge, which have significant impact even on the in-plane components of the Reynolds stress. Using the measured eddy viscosity tensor, we reconstructed Reynolds stress and evaluated the contributions of each eddy viscosity component. It is found that the D^0_{2123} component adds to the total Reynolds stress, increasing its magnitude for the SBLS case. This result is in contradiction of the independence principle [14] indicating non-negligible influence of spanwise velocity gradient on the mean momentum mixing even near the separation line.

Furthermore, in both the SBL and SBLS cases, we have identified regions where the measured leading-order eddy viscosity is locally non-positive semidefinite. In these areas, momentum mixing must involve significant nonlocal effects. Furthermore, regions of local negative production were found to be correlated with regions of non-positive semidefinite leading-order eddy viscosity. However, the reverse correlation was not the case. We do not have a proof on whether either correlation should hold universally, and expect more diverse data would shed light on this matter.

Lastly, using MFM and momentum budget analysis, eight significant components of eddy viscosity were identified that capture Reynolds stress accurately, with the first five identified from SBL analysis and the last three added due to the sweep effect. These findings open unique ways to understand momentum mixing by turbulence in the context of wall-bounded flows, revisit prior work on turbulence modeling, and enable insights on how to improve the existing RANS models.

Appendix A

Estimation of the Convergence Error for a Channel Flow

Figure A.1 shows the convergence analysis of MFM results with respect to the spatio-temporal domain size. Figure A.1(a) shows the estimated temporal error due to the finite time horizon of the MFM simulations. In our MFM studies we used a temporal sampling window of $T = 850$ in eddy turnover time unit, which is substantially longer than simulation times typically used in the literature. We estimate the temporal convergence error by comparing D^0_{2121} obtained from a shorter window, $T = 400$, with that obtained from the full simulation. Based on the magnitude of the difference, shown in Figure A.1(a), we estimate that the temporal convergence error, is about 1%.

In addition to the sampling time convergence study, we discuss the use of time dependent forcing. MFM restricts the forcing to be in the macroscopic space, the Reynolds-averaged space. For the channel flow, the forcing needs to be only a function of wall-normal direction, i.e. $s_i(x_2)$, and hence, time independent. Therefore, the precise way of conducting the MFM analysis is to estimate the stationary forcing prior to the computation. This is problematic since it is difficult to know the forcing terms before the simulation. The remedy to this issue is to perform averages over ensembles, instead of using time averages. For a statistically stationary flow, the ensemble-averaged fields tend to time-constant fields as one increases the number of ensembles. Ensemble averages can then be accessed at each time step, in order to estimate $s_i(x_2)$ according to the procedure described in Section 2.1.3. Since channel flow is statistically homogeneous in x_1 and x_3 directions, instead of creating new simulations, we used these directions for ensemble averaging. We then increased the number of independent ensembles by increasing the domain size in these directions. Figure A.1(b) shows the computed D^0_{2121} in two different domain sizes: one is the original domain size shown in Table 2.1 and the other is a larger domain which is twice bigger in both x_1 and x_3. The difference between these two plots are approximately 2%. This difference quantitatively represents the error

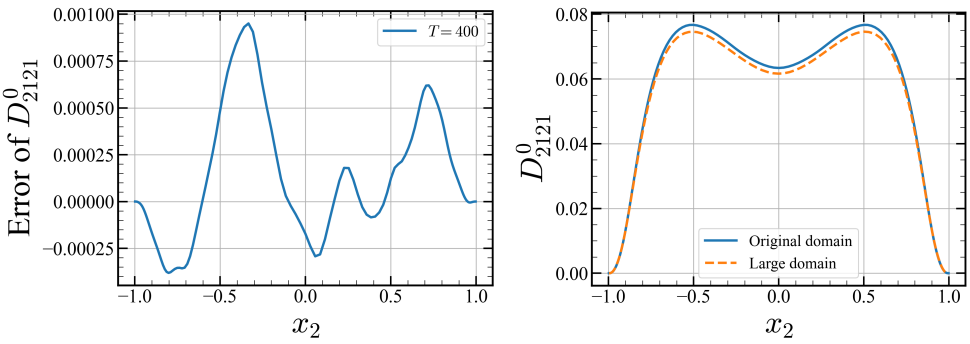

(a) Temporal convergence

(b) Domain convergence

Figure A.1: Convergence studies on D^0_{2121}; (a) $D^0_{2121}(T = 400) - D^0_{2121}(T = 850)$ where T is normalized sampling time period; (b) D^0_{2121} where the blue solid line is from the original domain (Table 2.1) and the orange dashed line is from the larger domain where domain length is twice larger in both x_1 and x_3 directions.

committed by using a weakly time dependent forcings and finite domain size.

Appendix B

Implementation for Determining D^0_{ijkl} in a Periodic Domain

MFM allows computation of every component in the leading-order eddy viscosity tensor D^0_{ijkl} in Equation 2.17. In Section 2.2.2., we briefly explained how D^0_{ij21} is determined via MFM with a forcing taht would maintain $V_1 = x_2$ and $V_2 = V_3 = 0$. For this case, boundary conditions and the initial condition are easily chosen to be compatible with the MFM instructions; for instance, periodic conditions in x_1 and x_3 direction and a Dirichlet condition in x_2 such as $v_1(x_1, x_2 = \pm 1, x_3) = \pm 1$. The simple generalization of the forcing to other directions is $V_n = x_m$ and $V_{i \neq n} = 0$ where m and n is not indices in the index notation, rather a choice of the forcing direction. However, such directional forcing is problematic in certain directions. For example, MFM of $V_2 = x_1$ and $V_1 = V_3 = 0$ forcing to compute D_{ij12} has incompatible boundary conditions with the DNS solver since $V_2 = x_1$ is not a periodic field in the streamwise direction . Therefore, to compute all the components of the eddy viscosity tensor, we modify the GMT to solve for the fluctuating part of the GMT variable v'_i. We start from the GMT equations with forcing of $V_n = x_m$ and $V_{i \neq n} = 0$ which gives a tensor D^0_{ijmn} as shown in Equation B.2. When we subtract the mean of the GMT equation from the GMT equation, the equation becomes the following:

$$\frac{\partial v'_i}{\partial t} + \frac{\partial}{\partial x_j}\left(u_j v'_i\right) = -\frac{\partial p}{\partial x_i} + \nu \frac{\partial^2 v'_i}{\partial x_j \partial x_j} + s_i - u_m \delta_{in} \tag{B.1}$$

At given m and n, once we solve for the equation above, we can determine the nine of the eddy viscosity tensor by post-processing the results as Equation B.2. Using various m and n, we reveal all the element in the leading-order eddy viscosity tensor.

$$-\overline{u'_i v'_j}(x_2) = \int_{y_2} D_{ijkl}(x_2, y_2) \left.\frac{\partial V_l}{\partial x_k}\right|_{y_2} \mathrm{d}y_2 \sim \int_{y_2} D_{ijmn}(x_2, y_2) \mathrm{d}y_2 = D^0_{ijmn}(x_2) \tag{B.2}$$

There are multiple advantages of solving for GMT fluctuation equations. The first advantage is that the boundary condition is now compatible with the periodic conditions. Second, all the boundary conditions are easily set with a periodic condition or a Dirichet condition of $v'_i = 0$ at the boundary. With these two advantages, the solver become more systematic and simple.

Appendix C

Scaling Analysis for 2D Spatially Developing Boundary Layer

To determine which components of the eddy viscosity tensor are critical to the RANS of the two-dimensional spatially developing boundary layer, we conduct the following scaling analysis. The flow system with the streamwise length scale l and the wall-normal length scale d is considered where $l \gg d$. Based on the correlation by [70], a typical ratio for $\mathrm{Re}_x \sim O(10^6)$ is $d/l \sim 0.02$. Using the leading-order eddy viscosity tensor model, Equation 2.17, the Reynolds stress term includes a summation of the eddy viscosity tensor terms. For instance, $\overline{u_2' u_1'}$ is represented as follows:

$$-\overline{u_2' u_1'} = D_{2111}\frac{\partial U_1}{\partial x_1} + D_{2112}\frac{\partial U_2}{\partial x_1} + D_{2121}\frac{\partial U_1}{\partial x_2} + D_{2122}\frac{\partial U_2}{\partial x_2} \tag{C.1}$$

One needs to consider not only the magnitude of the eddy viscosity tensor element but also the estimated scales of each term in this equation. To evaluate the length scales for the velocity, we set $U_1 \sim 1$, and the continuity enforces $U_2 \sim d/l$. Ignoring D_{21kl} coefficients, the length scales of the four terms on the right-hand side are $1/l$, d/l^2, $1/d$, and $1/l$. Since $l \gg d$, D_{2121} plays the major role for this Reynolds stress. The next two are the terms that multiply D_{2111} and D_{2122}. However, MFM reveals that D_{2111} is one order of magnitude larger than D_{2122}. Hence, D_{2111} is the next important eddy viscosity tensor for this Reynolds stress. Likewise, we conducted scaling analysis for all other Reynolds stresses. The analysis informs that D_{1111}, D_{1121}, D_{2121}, and D_{2221} are among the most significant eddy viscosity tensor elements for the case of slowly developing semi-parallel wall-bounded flows.

Appendix D

MFM for D_{ij21} Measurement

To compute the eddy viscosity kernel $D_{ij21}(x_2, y_2)$, we use brute force MFM method using delta function forcing of the velocity gradient at each location. We start from the full kernel eddy viscosity representation in Equation 2.10. We macroscopically force the mean velocity gradient by $\partial V_l/\partial x_k = \delta(y_2 - y_2^*)\,\delta_{k2}\delta_{l1}$, where $\delta(x)$ represents Dirac delta function, δ_{ij} represents Kronecker delta in index notation, and y_2^* is the probing location of the eddy viscosity. With such forcing, Equation 2.10 becomes the following:

$$\begin{aligned} -\overline{u_i' v_j'}(x_2) &= \int D_{ijkl}(x_2, y_2) \left.\frac{\partial V_l}{\partial x_k}\right|_{y_2} \mathrm{d}y_2 \\ &= \int D_{ijkl}(x_2, y_2)\,\delta(y_2 - y_2^*)\,\delta_{k2}\delta_{l1}\mathrm{d}y_2 \\ &= D_{ij21}(x_2, y_2 = y_2^*) \end{aligned}$$

Forcing that would maintain the mean streamwise velocity as a Dirac delta function at $y_2 = y_2^*$ reveals the eddy viscosity kernel $D_{ij21}(x_2, y_2 = y_2^*)$. By setting y_2^* for all possible locations, we can obtain the eddy viscosity kernel D_{ij21}. In numerical implementation of this strategy, instead of dealing with Dirac delta functions, we selected V_1 to be a step function with respect to the y_2 direction. In discrete space, the MFM is conducted at each discrete point of y_2^* in wall-normal direction with a corresponding heaviside function where the discontinuous point lies at that point. In order to compute the entire kernel D_{ij21}, one need to conduct many MFM simulations. More specifically, the number of simulations has to be the number of degree of freedom of the Reynolds-averaged space, i.e. the number of mesh points in the wall-normal direction. For instance, since our RANS space has 144 cell centers, we need 146 MFM simulations, including two for the boundary values.

Bibliography

[1] Hiroyuki Abe. Reynolds-number dependence of wall-pressure fluctuations in a pressure-induced turbulent separation bubble. *Journal of Fluid Mechanics*, 833:563–598, 2017.

[2] Hiroyuki Abe. Direct numerical simulation of a turbulent boundary layer with separation and reattachment over a range of Reynolds numbers. *Fluid Dynamics Research*, 51(1):011409, 2019.

[3] Hiroyuki Abe, Yasuhiro Mizobuchi, Yuichi Matsuo, and Philippe R Spalart. DNS and modeling of a turbulent boundary layer with separation and reattachment over a range of Reynolds numbers. *Annual Research Briefs*, 143, 2012.

[4] Rafik Absi. Eddy viscosity and velocity profiles in fully-developed turbulent channel flows. *Fluid Dynamics*, 54(1):137–147, 2019.

[5] Nasser Ashgriz and Javad Mostaghimi. An introduction to computational fluid dynamics. *Fluid Flow Handbook*, 1:1–49, 2002.

[6] George K Batchelor. Diffusion in a field of homogeneous turbulence. I. Eulerian analysis. *Australian Journal of Chemistry*, 2(4):437–450, 1949.

[7] Sanjeeb T Bose, Parviz Moin, and Donghyun You. Grid-independent large-eddy simulation using explicit filtering. *Physics of Fluids*, 22(10), 2010.

[8] Joseph Boussinesq. *Essai sur la théorie des eaux courantes*. Impr. nationale, 1877.

[9] René-Daniel Cécora, Rolf Radespiel, Bernhard Eisfeld, and Axel Probst. Differential Reynolds-stress modeling for aeronautics. *AIAA Journal*, 53(3):739–755, 2015.

[10] Kuei-Yuan Chien. Predictions of channel and boundary-layer flows with a low-Reynolds-number turbulence model. *AIAA Journal*, 20(1):33–38, 1982.

[11] Andrea Cimarelli, Adriano Leonforte, Elisabetta De Angelis, Andrea Crivellini, and Diego Angeli. On negative turbulence production phenomena in the shear layer of separating and reattaching flows. *Physics Letters A*, 383(10):1019–1026, 2019.

[12] Gary N Coleman, John Kim, and Anh-Tuan Le. A numerical study of three-dimensional wall-bounded flows. *International Journal of Heat and Fluid Flow*, 17(3):333–342, 1996.

[13] Gary N Coleman, Christopher L Rumsey, and Philippe R Spalart. Numerical study of turbulent separation bubbles with varying pressure gradient and Reynolds number. *Journal of Fluid Mechanics*, 847:28–70, 2018.

[14] Gary N Coleman, Christopher L Rumsey, and Philippe R Spalart. Numerical study of a turbulent separation bubble with sweep. *Journal of Fluid Mechanics*, 880:684–706, 2019.

[15] Régis Du Vachat. Realizability inequalities in turbulent flows. *Physics of Fluids*, 20(4):551–556, 1977.

[16] Paul A Durbin. A Reynolds stress model for near-wall turbulence. *Journal of Fluid Mechanics*, 249:465–498, 1993.

[17] Georg Eitel-Amor, Ramis Örlü, Philipp Schlatter, and O Flores. Hairpin vortices in turbulent boundary layers. *Physics of Fluids*, 27(2), 2015.

[18] Gordon A Gerolymos, Celine Lo, Isabelle Vallet, and Bassam A Younis. Term-by-term analysis of near-wall second-moment closures. *AIAA Journal*, 50(12):2848–2864, 2012.

[19] Fujihiro Hamba. Nonlocal expression for scalar flux in turbulent shear flow. *Physics of Fluids*, 16(5):1493–1508, 2004.

[20] Fujihiro Hamba. Nonlocal analysis of the Reynolds stress in turbulent shear flow. *Physics of Fluids*, 17(11), 2005.

[21] Fujihiro Hamba. Exact transport equation for local eddy viscosity in turbulent shear flow. *Physics of Fluids*, 25(8), 2013.

[22] Kemal Hanjalić and Brian E Launder. A Reynolds stress model of turbulence and its application to thin shear flows. *Journal of Fluid Mechanics*, 52(4):609–638, 1972.

[23] Julius Hinze. Turbulence: An introduction to its mechanism and theory. *McGraw-Hill Book Company, Inc*, page 22, 1959.

[24] AKMF Hussain and WC Reynolds. Measurements in fully developed turbulent channel flow. *American Society of Mechanical Engineers*, (75-FE-5), 1975.

[25] Javier Jiménez. Near-wall turbulence. *Physics of Fluids*, 25(10):101302, 2013.

[26] John Kim and Parviz Moin. Application of a fractional-step method to incompressible Navier-Stokes equations. *Journal of Computational Physics*, 59(2):308–323, 1985.

[27] Robert H Kraichnan. Eddy viscosity and diffusivity: exact formulas and approximations. *Complex Systems*, 1(4-6):805–820, 1987.

[28] Doug S Lacy and Anthony J Sclafani. Development of the high lift common research model (hlcrm): A representative high lift configuration for transonic transports. In *54th AIAA Aerospace Sciences Meeting*, page 0308, 2016.

[29] Brian E Launder, G Jr Reece, and Wolfgang Rodi. Progress in the development of a Reynolds-stress turbulence closure. *Journal of Fluid Mechanics*, 68(3):537–566, 1975.

[30] Myoungkyu Lee and Robert D Moser. Direct numerical simulation of turbulent channel flow up to. *Journal of Fluid Mechanics*, 774:395–415, 2015.

[31] Jessie Liu, Hannah Williams, and Ali Mani. A systematic approach for obtaining and modeling a nonlocal eddy diffusivity. *arXiv preprint arXiv:2111.03914*, 2021.

[32] Adrián Lozano-Durán, MJ Philipp Hack, and Parviz Moin. Modeling boundary-layer transition in direct and large-eddy simulations using parabolized stability equations. *Physical Review Fluids*, 3(2):023901, 2018.

[33] Thomas S Lund, Xiaohua Wu, and Kyle D Squires. Generation of turbulent inflow data for spatially-developing boundary layer simulations. *Journal of Computational Physics*, 140(2):233–258, 1998.

[34] Ali Mani and Danah Park. Macroscopic forcing method: A tool for turbulence modeling and analysis of closures. *Physical Review Fluids*, 6(5):054607, 2021.

[35] Mortaza Mani, Deric Babcock, Chad Winkler, and Philippe Spalart. Predictions of a supersonic turbulent flow in a square duct. In *51st AIAA Aerospace Sciences Meeting Including the New Horizons Forum and Aerospace Exposition*, page 860, 2013.

[36] Florian R Menter. Two-equation eddy-viscosity turbulence models for engineering applications. *AIAA Journal*, 32(8):1598–1605, 1994.

[37] Pedro M Milani. *Machine learning approaches to model turbulent mixing in film cooling flows*. PhD thesis, 2020.

[38] Parviz Moin and John Kim. Numerical investigation of turbulent channel flow. *Journal of Fluid Mechanics*, 118:341–377, 1982.

[39] Yohei Morinishi, Thomas S Lund, Oleg V Vasilyev, and Parviz Moin. Fully conservative higher order finite difference schemes for incompressible flow. *Journal of Computational Physics*, 143(1):90–124, 1998.

[40] Y Na and Parviz Moin. Direct numerical simulation of a separated turbulent boundary layer. *Journal of Fluid Mechanics*, 374:379–405, 1998.

[41] Danah Park, Jessie Liu, and Ali Mani. Direct measurement of the eddy viscosity tensor in a canonical separated flow: What is the upper bound of accuracy for local Reynolds stress models? In *AIAA SCITECH 2022 Forum*, page 0940, 2022.

[42] Danah Park and Ali Mani. Direct calculation of the eddy viscosity operator in turbulent channel flow at $Re_\tau = 180$. *arXiv preprint arXiv:2108.10898*, 2021.

[43] Danah Park and Ali Mani. Direct measurement of the eddy viscosity tensor in a turbulent separation bubble with sweep. In *AIAA AVIATION 2023 Forum*, page 3268, 2023.

[44] Ugo Piomelli and Elias Balaras. Wall-layer models for large-eddy simulations. *Annual Review of Fluid Mechanics*, 34(1):349–374, 2002.

[45] Sergio Pirozzoli. Revisiting the mixing-length hypothesis in the outer part of turbulent wall layers: mean flow and wall friction. *Journal of Fluid Mechanics*, 745:378–397, 2014.

[46] Stephen B Pope. A more general effective-viscosity hypothesis. *Journal of Fluid Mechanics*, 72(2):331–340, 1975.

[47] Stephen B Pope. Turbulent flows. *Measurement Science and Technology*, 12(11):2020–2021, 2001.

[48] Robert S Rogallo. Numerical experiments in homogeneous turbulence. 81315, 1981.

[49] Michael M Rogers, Nagi N Mansour, and William C Reynolds. An algebraic model for the turbulent flux of a passive scalar. *Journal of Fluid Mechanics*, 203:77–101, 1989.

[50] Michael M Rogers and Parviz Moin. The structure of the vorticity field in homogeneous turbulent flows. *Journal of Fluid Mechanics*, 176:33–66, 1987.

[51] Nicolae Romanof. Application of the orthonormal expansion of random functions to turbulent diffusion. In *Proceedings of the Seventh Conference on Probability Theory: August 29–September 4, 1982, Brasov, Romania*, pages 493–496. De Gruyter, 1985.

[52] Christopher L Rumsey, Jan-Renee Carlson, Thomas H Pulliam, and Philippe R Spalart. Improvements to the quadratic constitutive relation based on nasa juncture flow data. *AIAA Journal*, 58(10):4374–4384, 2020.

[53] Christopher L Rumsey, Jeffrey P Slotnick, and Anthony J Sclafani. Overview and summary of the third AIAA high lift prediction workshop. *Journal of Aircraft*, 56(2):621–644, 2019.

[54] Ulrich Schumann. Realizability of Reynolds-stress turbulence models. *Physics of Fluids*, 20(5):721–725, 1977.

[55] Jongmin Seo, Ricardo García-Mayoral, and Ali Mani. Pressure fluctuations and interfacial robustness in turbulent flows over superhydrophobic surfaces. *Journal of Fluid Mechanics*, 783:448–473, 2015.

[56] Yasaman Shirian and Ali Mani. Eddy diffusivity operator in homogeneous isotropic turbulence. *Physical Review Fluids*, 7(5):L052601, 2022.

[57] Jeffrey P Slotnick. Integrated CFD validation experiments for prediction of turbulent separated flows for subsonic transport aircraft. In *NATO Science and Technology Organization, Meeting Proceedings RDP*, 2019.

[58] Alexander J Smits and Ivan Marusic. Wall-bounded turbulence. *Physics Today*, 66(9):25–30, 2013.

[59] Philippe R Spalart. Direct simulation of a turbulent boundary layer up to $Re_\theta = 1410$. *Journal of Fluid Mechanics*, 187:61–98, 1988.

[60] Philippe R Spalart. Strategies for turbulence modelling and simulations. *International Journal of Heat and Fluid Flow*, 21(3):252–263, 2000.

[61] Philippe R Spalart and Steven R Allmaras. A one-equation turbulence model for aerodynamic flows. *La Recherche Aérospatiale*, (1):5–21, 1994.

[62] Philippe R Spalart and Gary N Coleman. Numerical study of a separation bubble with heat transfer. *European Journal of Mechanics*, 16(2):169–189, 1997.

[63] Philippe R Spalart, Michael Strelets, and Andrey Travin. Direct numerical simulation of large-eddy-break-up devices in a boundary layer. *International Journal of Heat and Fluid Flow*, 27(5):902–910, 2006.

[64] Charles G Speziale, Ridha Abid, and Paul A Durbin. On the realizability of Reynolds stress turbulence closures. *Journal of Scientific Computing*, 9:369–403, 1994.

[65] Charles G Speziale, Sutanu Sarkar, and Thomas B Gatski. Modelling the pressure–strain correlation of turbulence: an invariant dynamical systems approach. *Journal of Fluid Mechanics*, 227:245–272, 1991.

[66] Milomir M Stanišić and Richard N Groves. On the eddy viscosity of incompressible turbulent flow. *Zeitschrift für angewandte Mathematik und Physik ZAMP*, 16(5):709–712, 1965.

[67] Nicolaas Godfried Van Kampen. *Stochastic processes in physics and chemistry*, volume 1. Elsevier, 1992.

[68] Zellman Warhaft. An experimental study of the effect of uniform strain on thermal fluctuations in grid-generated turbulence. *Journal of Fluid Mechanics*, 99(3):545–573, 1980.

[69] Jonathan H Watmuff. An experimental investigation of a low Reynolds number turbulent boundary layer subject to an adverse pressure gradient. *Annual Research Briefs*, 1:37–49, 1989.

[70] Frank M White and Joseph Majdalani. *Viscous fluid flow*, volume 3. McGraw-Hill New York, 2006.

[71] David C Wilcox. *Turbulence modeling for CFD*, volume 2. DCW industries La Canada, CA, 1998.

[72] David C Wilcox. Formulation of the kw turbulence model revisited. *AIAA Journal*, 46(11):2823–2838, 2008.

[73] Wen Wu, Charles Meneveau, and Rajat Mittal. Spatio-temporal dynamics of turbulent separation bubbles. *Journal of Fluid Mechanics*, 883, 2020.

[74] Victor Yakhot and Katepalli R Sreenivasan. Anomalous scaling of structure functions and dynamic constraints on turbulence simulations. *Journal of Statistical Physics*, 121:823–841, 2005.

[75] A Cengel Yunus. *Fluid mechanics: fundamentals and applications*. McGraw Hill, 2010.